A Multi-Scale Molecular Dynamic Approach to the Study of the Outer Membrane of the Bacteria *Psudomonas Aeruginosa* PA01 and the Biocide Chlorhexidine

by

Brad Van Oosten

B.Sc. (Honours) Department of Physics, Brock University, 2011

A THESIS SUBMITTED IN PARTIAL FULFILMENT OF
THE REQUIREMENTS FOR THE DEGREE OF

DOCTOR OF PHILOSOPHY

in

The Faculty of Mathematics and Sciences

Department of Physics

BROCK UNIVERSITY

September 15, 2016

In presenting this thesis in partial fulfilment of the requirements for an advanced degree at the Brock University, I agree that the Library shall make it freely available for reference and study. I further agree that permission for extensive copying of this thesis for scholarly purposes may be granted by the head of my department or by his or her representatives. It is understood that copying or publication of this thesis for financial gain shall not be allowed without my written permission.

(Signature) _____

Department of Physics

Brock University
St.Catharines, Canada

Date _____

Abstract

The introductory chapters of this thesis contains an explanation to the methods and basic theory of the molecular dynamics approach. Together with the appendix section, in which a step by step tutorial how to set up and run basic simulations using the gromacs software is presented, this thesis can serve as an introductory aid in performing molecular dynamics simulations. In the research portion of this thesis, I provide several uses for the molecular dynamics approach applied to the biocide chlorhexidine as well as the study of membranes, including a mimic of the bacteria membrane of Pseudomonas Aeruginosa PA01.

The motivation for this research was previous work done in our lab which determined that chlorhexidine has a high affinity for DMPC and found the depth at which it resides in a model DMPC membrane. From this information, an all-atom representation of chlorhexidine was made, which was proven to reproduce the experimental results. While we learned much about chlorhexidine in a model DMPC membrane, this study lacked the destruction of the membrane as well as the study of chlorhexidine in a biologically relevant membrane. For these reasons coarse grained versions of the all-atom chlorhexidine models as well as a new lipopolysaccharide molecule was created. With the coarse grained model of chlorhexidine and the ability to create a bacterial membrane mimic, the study

of chlorhexidine and other antibacterial agents can be further studied.

Contents

List of Tables

List of Figures

Nomenclature

AA All-atom

BGU Biguanide

CG Coarse grain

CHX Chlorhexidine

CPL Chlorophenol ring

CPU Central processing unit

DFT Density functional theory

DLPC 1,2-dilauroyl-sn-glycero-3-phosphocholine

DMPC 1,2-dimyristoyl-sn-glycero-3-phosphocholine

DPPC 1,2-dipalmitoyl-sn-glycero-3-phosphocholine

EM Energy minimization

GPU Graphics processing unit

HEX Hexane

HWHM Half width at half max

LJ Lennard-Jones

LPS Lipopolysaccharide

MD Molecular dynamics

PC phosphatidylcholine

PE phosphatidylethanolamine

PG Phosphatidylglycerol

PMF Potential of mean force

POPE 1-palmitoyl-2-oleoyl-sn-glycero-3-phosphoethanolamine

PS phosphatidylserine

QM Quantum mechanics

WHAM Weighted histogram analysis method

Preface

List of publications:

B. Van Oosten, D. Marquardt, I. Komljenovic, J. P. Bradshaw, E. Sternin, T. A. Harroun, Small molecule interaction with lipid bilayers: A molecular dynamics study of chlorhexidine, Journal of Molecular Graphics and Modelling 48 (2014) 96-104.

N. Kucerka, B. van Oosten, J. Pan, F. A. Heberle, T. A. Harroun, J. Katsaras, Molecular Structures of Fluid Phosphatidylethanolamine Bilayers Obtained from Simulation-to-Experiment Comparisons and Experimental Scattering Density Profiles, Journal of Physical Chemistry B 119 (5) (2014) 1947-1956.

B. Van Oosten, T. A. Harroun, A MARTINI extension for *Pseudomonas aeruginosa* PAO1 lipopolysaccharide, Journal of Molecular Graphics and Modelling 63 (2016) 125-133.

Acknowledgements

I would like to express my gratitude and appreciation to my supervisor, Dr. Thad Harroun for his guidance, support and opportunities he's granted me during my education. Without his open mindedness towards changes in my thesis direction I would not have thoroughly enjoyed my time reaserching at Brock University half as much.

I also owe a great deal of thanks to my supervisory committee, including Dr. Edward Sternin, and Dr. David Crandles, for their support and guidance, which in turn have helped immensely to improve both the clarity and completeness of this thesis.

I would also like to thank all of the lab members of the Brock's biophysics lab. Although some of you were here for a long portion of my degree, many others came and left for a quick summer position or 4F90 project. However, every single one of you have been helpful in inspiring new ideas and the ability to take a break by spend time thinking about projects other than my own. A special thanks to Ivana, who helped me at the beginning of my thesis, and whose project I carried forward when she finished her MSc. A special thanks as well to Drew, who was present for a major portion of my thesis, helping with ideas when I got stumped, and chiefly, in aiding to fill in the gaps in my knowledge about chemistry and

what can and cannot be done experimentally.

I would also like to acknowledge the support of my friends aforementioned above as well as Egor, Michelle, and the rest of the sushi gang, for their help, support and most importantly, a means for a coffee or food break to escape from work or to just take a break in order to keep my sanity.

Chapter 1

Introduction

1.1 Molecular Dynamic (MD) Simulations

Molecular dynamic (MD) simulations are a set of computational methods used in the study of the motion of atoms and molecules based on the laws of physics. MD is founded on classical newtonian mechanics, allowing the atoms to interact for a set period of time, leading to the evolution of the system.

The method of MD was first published in 1959 [1], in which MD simulations were used to observe elastic collisions of 500 hard sphere particles. The method was created as an alternative to Monte Carlo simulations. The Monte Carlo method uses an algorithm which chooses movements which lower the energy taking steps which are chosen randomly rather than using equations of motion. This constricts its area of research to study equilibrium states only. The MD study by Alder and Wainwright [1] was different in that it was capable of studying relaxation phenomena and transport properties. They reported great success in their ability to produce reasonable results however, they noted some fundamental limitations to the method. Firstly, the memory of their best computers could only handle up to 500 particles at a time. Secondly they note a more

fundamental flaw that even without any memory limitations, the MD method is limited in the amount of time necessary to run the simulations. To analytically solve the equations of motion a time step must be small enough to capture the fastest motion being simulated. In the cast of most molecular structures, the vibration of the hydrogen atomic bonds have the fastest motion requiring a step of approximately 1 fs. This leads to a large number of calculations that must be carried out in a simulation. For their system of 500 particles they require "a half hour to achieve an average of one collision per particle".

Since the first appearance of MD in 1959, there have been huge advances in computational power, thus increasing the ability of MD simulations. However, even though computers can now perform calculations much faster, there is still no resolution to the necessity of a large number of small time step iterations. Current atomistic simulations take time steps on the order of 1 fs [2–4], meaning an order of 10^{15} steps must be taken in order to simulate even one second, which is currently not computationally feasible.

Currently two strategies are being implemented to reduce the severity of this problem. Firstly, research to develop faster computational devices capable of performing the number of calculations for 10^{15} time steps in a reasonable amount of time. This can be achieved by hardware designed specifically for MD type simulations. Anton, the world's fastest MD supercomputer at the time of writing this thesis has been built by D. E Shaw with the sole function being to perform MD calculations, at extremely high speeds [5]. To a lesser scale, dedicated graphics cards contain a graphics processing unit, which has been optimized for vector

algebra and can be purchased to greatly increase the ability of any desktop computer to perform MD calculations [6].

With the current computational capacity we are beginning to see simulations that can reach either the microsecond time scale [7–9] or into the 100s of nanometers in size [10–12]. Figure 1.1 is a pictorial representation of the current computational capabilities for MD simulations on an average high-end supercomputer (Spending millions of dollars on a supercomputing cluster will increase the size of the boxes representing the current computational capabilities).

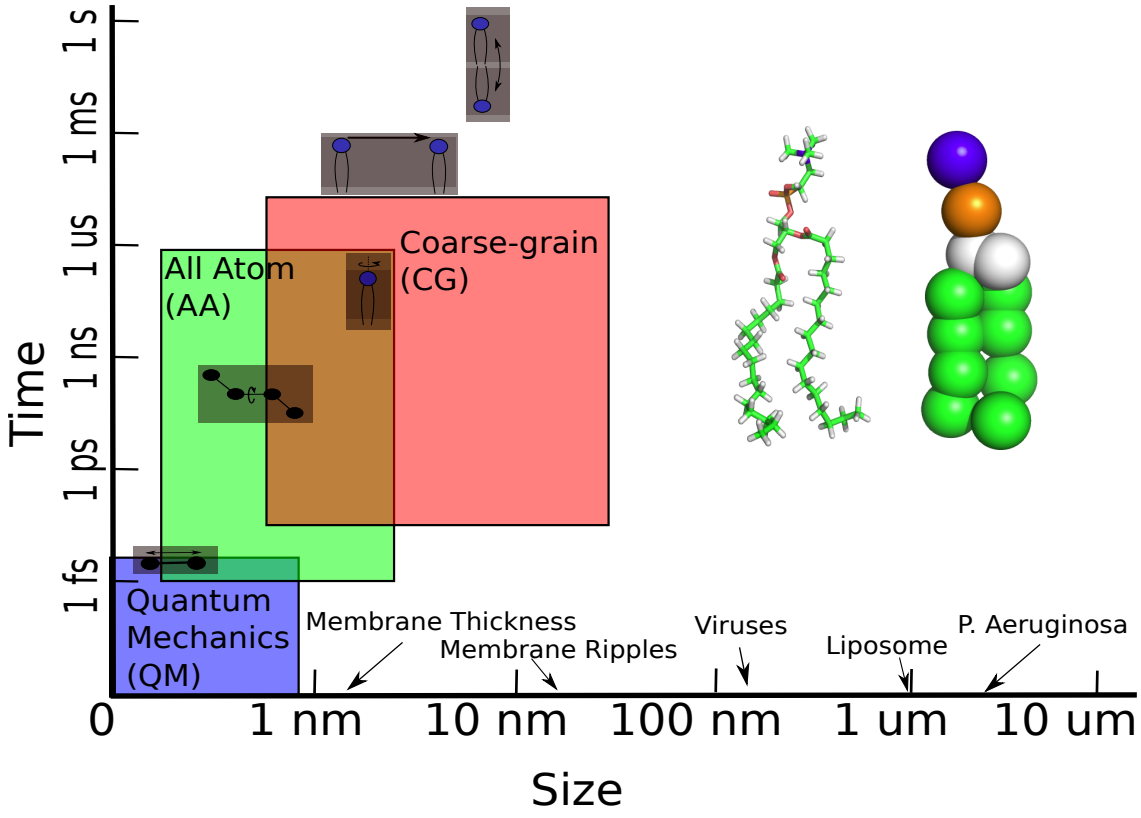

Figure 1.1: Time and size scales currently achievable for each of the three levels of resolution (quantum mechanics, all-atom and coarse grained). Pictorial lipid motions of bond stretching, trans-gauche isomerization, rotation, dispersion and flip-flop are located at their approximate time and length scales. Several labels along the size axis label the approximate size of several biologically relevant objects to enhance a sense of scale.

Despite the advances in computational devices continuing to increase, a major unresolved problem is that there is still a gap that exists between the time and length scales of that can be simulated compared to those measured experimentally. Also shown pictorially in Figure 1.1 are the rough estimated for the time/length scales of lipid motions with the smallest of lipid motion of atom vibrations happening on the order of $\sim 10^{-15}$s, and the slowest motion of lipid flip-flop happening on $\sim 10^{0}$s. This is a span of about 15 orders of magnitude. This is ignoring the fact that we would want to measure several times larger than the timescale of the longest motion to observe multiple instances of this motion in order to get the proper statistics to describe it. It is therefore a viable idea not to look at every type of motion in one simulation but rather create different techniques for different scales. This results in the ability to observe one property of interest at a time. Analogously there are a multitude of experimental techniques that can only observe properties on a certain timescale, yet in combination they can complement each other to give information over a wide range of scales. For proper membrane equilibration concerning membranes of a single component, simulations should be at least 1×10^{-6}s in order to allow several rotations of the lipids and rotation of the acyl chains to properly relax into its lowest energy position. This type of simulation can be done on the AA scale. Membranes with multiple components may need lipids to translate across the membrane to equilibrate and thus take upwards of $\sim 1 \times 10^{-3}$s, which is more fitting for a CG simulation.

MD has different resolution scales to observe different membrane properties.

Quantum mechanics can be used to describe the motion of electrons and charge through a system, however can not tackle a large system or a large time scale. An all-atom approach assumes electrons as stationary in order to allow for slightly larger and longer simulations. However, this approach limits the ability to study the motion of charges, as well as extremely large systems. Coarse grained simulations freeze whole sections of a molecule together in order to further reduce the degrees of freedom necessary to compute. This lengthens the length/time scales with the disadvantage of limiting the lower bound resolution. Each of these three methods are explained in greater detail in the following sections.

1.1.1 Quantum Mechanics (QM)

Quantum mechanical (QM) methods contribute a large role in the calculation of atomistic parameters. Density functional theory and Hartree Fock [13, 14] provide the methodology to determine the ground state energy of a molecular structure, as well as provide the molecular charge density.

Calculating the ground state energy of an ensemble of molecules with a single atomic bond at different values of its length will give a parabolic energy function close to the equilibrium bond length. An atomistic force field can utilize this information to approximate its bonded term which is generally represented as a harmonic spring term with its length and strength determined through a mixture of experimental information as well as these QM calculations. Similarly, any other interaction potential can be calculated in a similar fashion such as the angle or dihedral terms.

QM calculations can also determine the molecular charge density. Mulliken population analysis method can then utilize this charge density to determine the correct partial charges. The partial charges located at the center of the atoms of the atomic structure will give rise to the same calculated molecular charge density [15].

1.1.2 All-Atom (AA)

All-atom (AA) simulations negate the electron motions of QM calculations and instead estimate them as a partial charge frozen into spheres representing each atom of the molecule. Without the computationally intensive calculation of the electron behaviour, the AA simulation can be made larger, with atomic resolution. Because their charges are static, AA simulations can not reproduce charge exchange or different excitation levels. In exchange for this simplification, they can represent reasonably large systems in comparison to the QM counterpart.

AA simulations have each atom represented by a sphere governed by newtonian mechanics to define its motion. Thermal motion drives the system to explore conformational space, but is limited by bonded and steric interactions to limit the motion to meaningful conformations. The resultant simulation creates snapshots across time in which the system has one of an infinite number of conformations. Boltzmann's statistical mechanics can then be used on this classical system to extract meaningful statistical properties of the system.

There also exists a variation to AA simulations called united atom simulations in which all atoms are represented by a single sphere except for hydrogen

atoms, which are implicit. These hydrogen atoms have their attributes absorbed into the atom to which they are connected. This was done since most experimental techniques do not have the resolution necessary to distinguish the location of single hydrogen atoms. Therefore since there is uncertainty in their actual position, removing them for more computational efficiency can be done without any substantial consequences [16].

1.1.3 Coarse Grained (CG)

Coarse grained (CG) simulations have been constructed to further increase the computational efficiency needed to simulate even larger systems than the AA counterpart. Coarse graining does to an AA simulation what the AA did to the QM simulations, it freezes internal degrees of freedom in order to decrease the computational cost to increase the simulation scale. Coarse graining removes internal degrees of freedom in a molecule by grouping several atoms into a single virtual particle which mimics the represented atom constituents as best as possible. These CG simulations are therefore best adapted to situations where large ensembles are necessary and atomic detail is of low priority. A popular example of the use of the CG method is to study domains created by mixtures of several different lipid types [17, 18]. In this example, the low level determination of each atom position is irrelevant, while the larger macroscopic level domains created by said lipids is of high importance.

1.1.4 Hybrid

The boundary between the resolution levels is blurred by hybrid solutions which combine the use of multiple resolution scales. QM/MM (quantum mechanics/-molecular mechanics) simulations utilize QM in combination with MM. This can be accomplished by limiting the QM calculations by either a subset of timesteps or sections of the simulation. Switching between the two scales performing a few steps utilizing QM followed by a few AA steps interchangeably allows for the motion of charge from the QM steps and large motional progression from the AA steps. It can also be advantageous to use QM calculations on a small subset of a system in which the motion of charge is of high importance and AA for the rest of the simulation, in order to still be able to simulate a reasonably large system. This results in a simulation with the accuracy of QM while still performing with an efficiency increase from the AA portion. This method has a wide span of uses from observing the charge transfer path within a protein [19] to the breaking of bonds in silicon crystals creating fractures [20].

Similar hybrid techniques have been created to combine AA with CG resolution scales in order to take advantage of both types of simulations through adaptive resolution. Adaptive resolution switches the whole system from CG to AA and visa-versa when necessary. An example of such is constructing and equilibrating a large system (which takes a significant amount of computational time) with the lower resolution CG simulation followed by converting all CG molecules into AA molecules and continuing the last of equilibration with atomic scale resolution [21]. This method enables the study of equilibrium properties of large

systems, while drastically reducing the computational time required to obtain the final equilibrium state.

1.2 Force Fields

The MD software uses a set of algorithms (further explained in Chapter 2) to enforce the laws of physics to a system of particles in order to create physically accurate motions. Force fields are the parameter sets which are used to calculate the potential energy of the system. This usually contains bonded interactions such as a bond length and strength, as well as nonbonded parameters such as the particle's charge, size and mass. These parameters are constructed so that they can accurately recreate the mechanics of physical system.

It is non-trivial to classify one force field as inherently better than another. Rather, each has been created to accurately recreate a certain observable property, and as a result may inadequately reproduce another. Force field parameters are obtained through a combination of experimental and theoretical calculations, weighted by importance as chosen by its creator. For example, consider the situation where two separate experimental techniques give a result of 0.24 nm and 0.28 nm for the distance between two atoms A and B. It would be up to the person creating the force field to then determine which value between 0.24 nm and 0.28 nm to choose as the actual distance between A and B based on the accuracy and reliability of each technique. This discretion leads to small variations in the force fields, leading to the wide variety of various available force fields.

Quantum mechanics are often used to determine the partial charges for a particle, for determining such experimentally is not currently feasible. Bonded parameters such as a bond length and strength can be measured by different techniques. Bond lengths are often determined through NMR spectroscopy or scattering experiments. As such, different force fields will rely more heavily on one type of experiment than another. The parameters are tweaked until the force field can best reproduce each of the experimental techniques within their selected tolerance. Because of these minute differences, there exist a plethora of different force fields, each built to be suited for a certain subset of results. It is therefore important to choose which force field is best based on the problem being studied.

1.2.1 MARTINI

The Martini force field was first released with a publication in 2003 as a simplified model for semiquantitative lipid simulations [22]. The goal of the Martini force field was to simulate lipid systems on the microscale, which is currently unreachable by traditional AA simulations. It has since grown in complexity and has expanded to proteins and small molecules, vastly increasing its catalogue of applications. In the first iteration of the Martini force field, a 4-1 atom mapping was used, where a single virtual particle represented approximately 4 heavy atoms of the atomistic molecule. These virtual particles were categorized into one of four main atom types: charged, apolar, polar and nonpolar. The charged and polar types were split into 4 subtypes to allow for further fine tuning. This created 10 particle types with different levels of attraction/repulsion to each other

ranging from 1-5 (1 being very attractive and 5 being repulsive).

The first molecules included in the Martini force field were a water molecule, a charged site representing an ion with its first hydration shell, a few alkanes as well a small subset of common lipid types with phosphatidylcholine (PC) and phosphatidylethanolamine (PE) headgroups [22]. The water and alkane models were each constructed to reproduce their bulk liquid properties such as density, compressibility and diffusion rates. A simulation box made of half water and half hexadecane was then constructed with these models. Their parameters were further tweaked to reproduce the AA water/hexadecane interface. The hexadecane model was then used to create a model 1,2-dipalmitoyl-sn-glycero-3-phosphocholine (DPPC) lipid, which consisted of 2 hexadecane chains as tails, as well as two particles as a backbone and two for the headgroup.

When randomly distributed in a water box, the DPPC molecules aggregated into a bilayer, which was able to reproduce the electron density profiles of atomistic simulations. This bilayer also demonstrated a phase transition from a fluid to crystalline state with general agreement with experimental data for the values of area per lipid in both states. The DPPC model was then altered to create various other PC lipids by switching the tails to different fatty-acyl chains of shorter and longer lengths. Similarly several PE lipids were made by changing one of the headgroup particle type to better mimic the PE headgroup.

The second iteration of the Martini force field came in 2007, with a vast increase in the number of particle types and particle-particle interactions. This allowed for a further fine tuning of the particles to better mimic a larger number

of atomic groupings [23]. The four main particle types remained, however, both the apolar and polar types were split into 5 subcategories each, increasing the number of particles from 10 to 18. Each of the 18 new particle types were also given a smaller 3-1 mapping counterpart with a 75% reduced interaction size utilized in ring structures, doubling the amount of atom types to 36 particle types. The number of non bonded particle-particle interaction levels increased as well from 1-5 to 0-9. The greater number of atom types and interaction levels lead to a greater distinction between lipid types, leading to increased accuracy. The ability to reproduce ring structures with the smaller particle types expanded the ability to create sterols such as cholesterol. With a large number of particle types, Martini has been able to expand beyond the ability to simulate lipids. It has been extended to include proteins in 2008 [24], carbohydrates in 2009 [25] and DNA in 2015 [26].

The Martini force field is not without its limitations. Its fundamental flaw is that in the coarse graining process, there is a loss in information due to the decreased resolution. This limitation created by the chosen 4-1 mapping for lipids can be described for lipids with the example of dimyristoylphosphatidylcholine (DMPC), a common lipid which has tails consisting of a chain of 14 carbon atoms. Since 14 is not equally divisible by 4, the consequence is to model it using 3 virtual particles (representing 12 carbons) or 4 virtual particles (representing 16 carbons). Neither option is an ideal choice because they represent a completely different lipid type. The addition of 2 carbons (16 total) is dipalmitoylphosphatidylcholine (DPPC) while removing 2 carbons (12 total) would be

dilauroylphosphatidylcholine (DLPC). The 4-1 mapping also oversimplifies the molecules electrostatics. While the total charge of a molecule is able to be conserved, the charge location and polarization effects are lost. The Martini force field is therefore inherently bad at reproducing important electrostatic interactions such as cation-pi interactions in proteins. The current best workaround to these limitations is to use a hybrid solution, backmapping the simulation to an atomistic simulation [27].

Polarizability is an important property of water, having a large effect on the intermolecular interactions between both itself and other molecules. Acting as small dipoles, the orientation of water molecules are affected by other surrounding water molecules as well as any surrounding molecular charges. Zwitterionic headgroups of lipids, are highly charged regions that create a large electrostatic dipole at the lipid/water interface. This region is one example of where the polarizability of water would make a large difference in the ordering of the water molecules in the localized area. To improve upon the behaviour of the Martini water model, a polarized water molecule was created where 4 water molecules were represented by a set of 3 virtual particles. These 3 virtual particles contained two partial charges to recreate an effective dipole term to recreate the electrostatic environment of the 4 water molecules that it represented. The resultant model lead to better reproducibility of water properties as well as the electrostatics of water and the interactions of charged particles. [28].

Thermodynamic properties of CG models are of particular interest. Martini has been constructed to best reproduce free energies of atomistic simulations.

While this is a preferred property for some calculations such as the potential of mean force, because of the decrease in the molecule's internal degrees of freedom, it alters the shift between enthalpic and entropic energy factors. Therefore, a CG model is not suitable for the decomposition of the free energy into its entropic and enthropic terms without the use of extreme caution. Another resulting effect is that the temperature of the CG simulation is by definition not physically correct. [27].

As well as the absolute temperature, the time scales of a CG simulation is not straightforward. Because coarse graining involved a smoothing of the energy landscape, motions are less restricted and therefore the kinetics of the system are sped up. An effective time scale can be calculated by comparing the motion of molecules such as the lateral diffusion of lipids to determine the proper multiplicative term to transfer the CG time scales into those comparable to experiments or atomistic simulations. Martini estimated this as a factor of 4, however studies show that it is highly dependant on the system, and can range from 1.2 to 22 times larger [27, 29].

The Current State of the Martini Research

Since its creation in 2003, the Martini force field has escalated its popularity, being used in an increasing amount of publications as shown in Figure 1.2. A large increase in the amount of publications using Martini was seen after its expansion beyond the original usage for semiquantitative lipid simulations [22], to include other molecules. Most notably, the inclusion of proteins in 2008 [24] can be spec-

ulated to be the cause of the large increase in publications the following year in 2009. After this publication, the Martini force field became a strong tool for the study of membrane bound protein. With the increase capabilities for larger system sizes as well as longer time scales offered by the Martini force field, studies were able to be conducted on large membrane bound protein complexes [30], interactions of peptides on the surface of membranes [31, 32], and the motion of the proteins in membranes [33, 34].

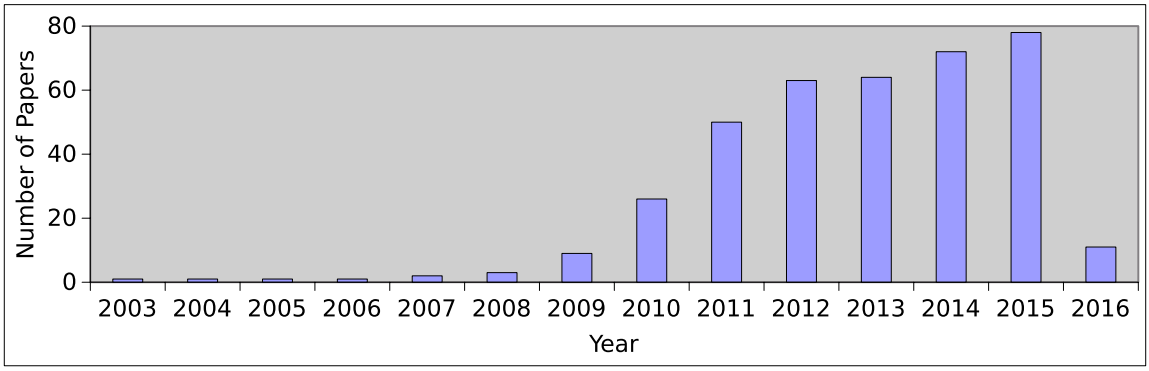

Figure 1.2: The number of papers published with the keywords "Martini simulations" determined via Web of Science [35].

Although the study of proteins seems to be the most prominent area of research surrounding the Martini force field, the main Martini research groups of Dr. Peter Tieleman and Dr. Siewert-Jan Marrink focus their research on expanding the library of molecules and tools in order to increase the span of reach of its usefulness. Within the last year in late 2015, two such publications were released from these research groups to expand the force field to include more sterols [36] as well as DNA [26]. These studies utilized a bottom up approach using AA sim-

ulations to create the bonded parameters, as well as use the potential of mean force pulling each component into a membrane to test the non-bonded interactions.

Additionally, as well as expanding the Martini force field, the groups of Tieleman and Marrink also use their force field to study membranes. Mainly, with the capability to create large systems they have created large vesicles [37] as well as utilized their lipid library with a vast number of lipid types available to create complex membrane systems. They have so far mimicked actual lipid compositions of a plasma [12] and thylakoid [10] membranes.

Simulating the interactions between small molecules and membranes is less prevalent in literature. This is likely due to the fact there is currently no library of Martini parameters for small molecules. This creates a large entrance barrier of time and effort to create these parameters for each new molecule. There still exists a few such studies [38–40], however their numbers are small in comparison to the number of studies on proteins. Proteins do not have the same entrance barrier as the small molecules since the Martini library already contains the parameters for amino acids. All that is needed is for the researcher to string together the amino acid sequence of whichever protein they want to simulate. The limited number of studies on small molecule interactions may soon be rectified with a recent tutorial on the Martini website describing how to create such parameters and a recent publication introducing a small molecule builder for Martini [41].

1.2.2 Slipids

The Slipids (Stockholm lipids) force field was derived at Stockholm University by the research group of Dr. Alexander Lyubartsev. The mandate of Slipids force field was to increase the accuracy of lipid simulations to reproduce a greater number of experimentally tested parameters [4]. The Slipids force field was first released with a publication in 2012, which focused on the parameters of three lipid types: 1,2-diauroyl-sn-glycero-3-phospocholine (DLPC), 1,2-dimyristoyl-sn-glycero-3-phosphocholine (DMPC), and 1,2-dipalmitoyl-sn-glycero-3-phospocholine (DPPC). The initial force field parameters were borrowed from the CHARMM36 (C36) force field and modified with emphasis the parameters of the lipid tails [3, 42].

Slipids focused mainly on modifications to the alkane tails. Partial charges of the alkane tails were recalculated using the restricted electrostatic potential approach with the DFT method. This approach was performed on an ensemble of alkanes to determine the partitioning of charges on a distribution of conformations. This is in contrast to the conventional method of using the single most prominent confirmation to calculate the charge distribution as in the creation of the CHARMM force field [3, 42]. The parameters of the Lennard-Jones potential were then systematically altered in order to best reproduce the latent heat of vapourization as well as densities measured from experimental results. This was done since both latent heat of vapourization as well as densities are directly correlated to the well depth of attraction in the Lennard-Jones potential. Alternating between Lennard-Jones and torsion angle parameters, modifications were

made to maximize agreement between the force field and experiments. The force field parameters were validated by comparing their ability to reproduce: lateral diffusion coefficients, ^{13}C longitudinal relaxation times, isothermal area compression modulus, thermal area expansion, thermal contractivities, volume per lipid, head-head distance, Luzzati distance, hydrophobic core thickness, electron density, scattering form factors, and deuterium order parameters at temperature of 303, 323 and 333K to encompass both the liquid and gel phases [4].

The Slipids force field was later extended to a greater number of lipid types, with further publications [43, 44]. Using the same methods as their first publication, parameters were made for unsaturated lipid tails and phosphatidylethanolamine(PE) headgroups [43]. Next, charged lipid headgroups were parameterized to extend Slipids to include sphingomyelin as well as phosphatidylglycerol(PG), and phosphatidylserine(PS) headgroups [44].

The Current State of the Slipids Force Field

Unlike the Martini force field which is a new construct to create a novel coarse grained resolution scale, the Slipids force field is a modification for increased accuracy to a force field which already exists. Because of this, many compatible molecular parameters already exist in libraries and do not have to be recreated from scratch. Instead of spending a large amount of time increasing the accuracy of each and every lipid type, the Slipids force field focus on only the most commonly studied: saturated and unsaturated phosphatidylcholine (PC), phosphatidylethanolamine (PE), phosphatidylglycerol (PG), phosphatidylserine (PS)

and sphingomyelin (SM) [4, 43, 44]. With these improved lipid parameters now created, no more work is being done to further this force field, as it has accomplished its goal and further work on less common lipids would be a lot of work for diminishing returns. Although the force field itself is not growing, Figure 1.3 shows an increase in its usage.

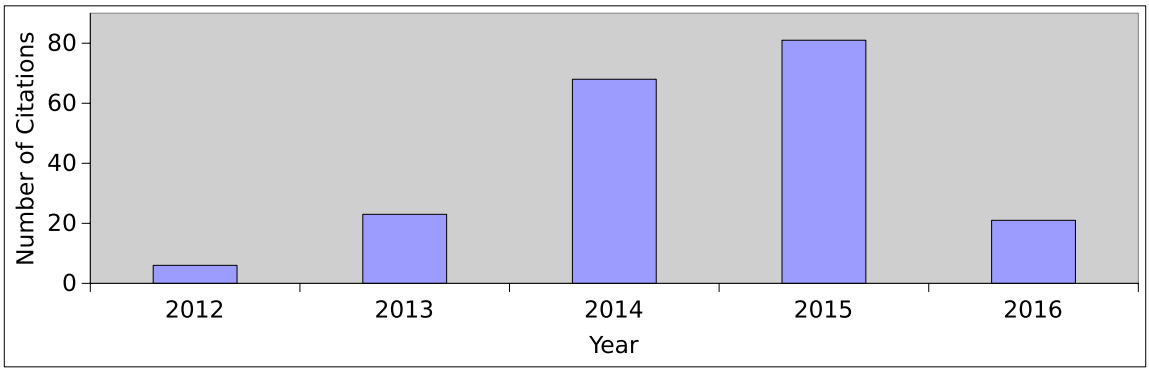

Figure 1.3: The number of papers citing the original three papers published with the release of the Slipids force field [4, 43, 44] as determined via Web of Science [35]

Now that the Slipids has created the means for lipid simulations able to reproduce many experimental properties, researchers have been using it to study many different systems. Since an all-atom force field requires a higher computational cost for increased accuracy, studies using Slipids has been focusing around simulations which desire atomic level precision. Kučerka, et al. used the Slipids force field to aid in determining the molecular structure of phosphatidylethanolamine bilayers using a comparison technique between simulations and experiment [45]. Here, the simulations were used as the model to fit the scattering form factors obtained from neutron and x-ray scattering. Uusitalo et al. utilized the Slipids

force field to aid in the creation of their coarse grained model of DNA [26]. Their model was made to best reproduce the Slipids energetics of partitioning nucleobases into a membrane. Slipids was chosen due to its attention in parameterizing the force field to recreate proper partitioning.

In a recent comparison study of five commonly used AA force fields (Berger, Slipids, CHARMM36, GAFFlipids and GROMOS 43A1-S3) Otyepka et al. contrasted the ability for each to reproduce experimental physical properties of DMPC [46]. Although all force fields did an adequate job in reproducing most of the lipid's physical properties, CHARMM36 and Slipids were closest to the experimentally obtained values. The study was furthered by studying the molecule-lipid interaction of 11 different molecules. The Slipids force field was best in recreating the partitioning coefficient for the 11 molecules as well as the prediction of free energy barriers. This result is most likely attributed to the extensive parameterization of the partial charges and Lennard-Jones potential terms of the Slipids force field.

Since the Slipids force field has enhanced parameters for the acyl chains it is best able to reproduce small molecule interactions in the center of a lipid membrane. For this reason, there are also simulations using the Slipids force field to study the insertion and interactions of small molecules inside of a membrane [47, 48].

1.2.3 Water Models

Many water models were originally developed concurrently with a specific force field but have since been adapted to be generalized and compatible with all force fields. As a result each force field usually comes with its recommended water model to use. However other water models may be used with caution depending on the specific usage. Simple point charge (SPC) was generated for the use with the GROMOS force field [49], while TIP3P was created with the AMBER force field [50], and modified into TIPS3P for usage with the CHARMM force field [3]. Higher complexity, 4 and 5 site TIP4P and TIP5P water models, were generated for the OPLS force field [51].

Of the various available water models there is a large amount of diversity in their complexity as well as the experimentally observed physical properties in which they can reproduce. Figure 1.4 shows how a single water model can be made using 3 atomic sites and up to 3 virtual sites used to shift the location of the atomic charges. A 3-site model is the most computationally efficient and contains the partial charges located on the centers of each of the atoms. A 4 site model also contains 3 charges, however the charge of the oxygen atom is no longer placed at the center of the atom, but rather it is located on the virtual site M [50]. The 5-site model places a negative charge on the 2 virtual L sites to represent the lone pairs of electrons [51]. The 6-site model is a combination of the 4-site and the 5-site, containing both L sites and an M site, to relocalize the charge of the oxygen atom[52].

Other than representing a water molecule with an increasing number of elec-

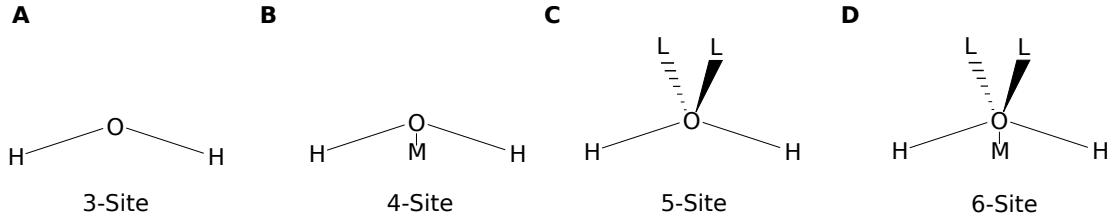

Figure 1.4: A) 3-site model, B) 4-site model containing offsite oxygen charge position M, C) 5-site model containing two offsite lone pair charge positions L, D) 6-site model containing offsite position M and lone pairs L

trostatic sites, other models have altered their performance by adding additional van der Waals terms, molecule flexibility, and polarizability (See Figure 1.5 for visual representation). The SPC model, again, is the simplest model to accurately describe a water molecule. It utilizes a single van der Waals sphere centered on the oxygen atom, with 3 charges located on each of the atom sites. A second, more complex alternative to the SPC model is the TIP3P model, which contains van der Waals terms for each of the hydrogen atoms as well as the oxygen atom. This enhances the shape of the molecule, however no additional changes are made to the molecule's electrostatics. A flexible model adds harmonic spring terms to the bond lengths and angles of the water's atoms. This creates a dynamic motion of the atoms, and therefore alters the dynamics of the location of the charges of the molecule. A Polarized model, adds an additional electrostatic term:

$$\vec{E}_{pol} = \sum_i \frac{(\vec{\mu} - \vec{\mu}_o)^2}{2\alpha_i}$$

to better reproduce the effects of water polarization, where $\vec{\mu}$ is the effective dipole moment of the model, $\vec{\mu}_o$ is the dipole moment of isolated water and α_i is the isotropic polarizability constant.

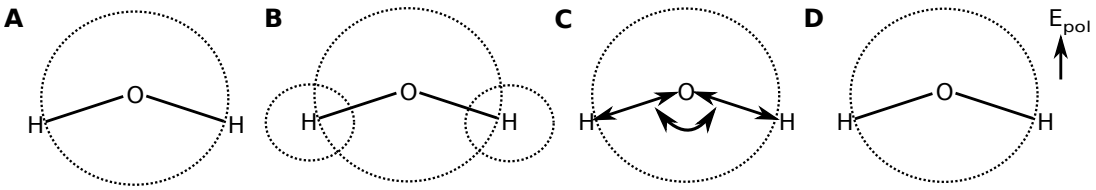

Figure 1.5: A) Simple point charge (SPC) model, B) three site model (TIP3P), B) Flexible model with variable bond lengths and bond angle (Flexible SPC), D) Polarizable model (SPC/E).

With the combination of 3, 4, 5 or 6 site water models as well as additional vdw terms on the hydrogen atoms, flexibility in the bonds/angle and polarization electrostatic terms, a plethora of different water models have been constructed, each with its own set of advantages and disadvantages. SPC is the most computationally efficient model, having the least amount of parameters. It is effective in closely reproducing experimental diffusion rates, average configurational energy, and specific heat C_p. However, this model fares much worse in its ability to reproduce the molecules dipole moment, dielectric constant, shear viscosity as well as several of the different ice phase regions [53–55]. TIP3P water is better able to reproduce all of the aforementioned water properties than the SPC model with exception to the diffusion rate. TIP3P however, can not reproduce all of the different ice phases, which currently can only be done by TIP4P [50].

CG water models were created to reproduce water using a mapping of virtual particles so that a single virtual particle represents multiple water molecules. The Martini force field, for example, uses their regular 4-1 construct to map four water molecules into one virtual water model. The first iteration of the Martini force field was released with a single water model type created to reproduce the isothermal compressibility coefficient and self-diffusion constant at 300 K [22]. This model however, did not fare well in reproducing the correct electrostatics (with a low dielectric constant), or the correct freezing temperature (being too high, around 290 K). The low dielectric constant was rectified by adding a screening dielectric constant throughout the whole system, whereas the high freezing point was mended by adding a larger "antifreeze particle", which prevented freezing at high temperatures. These problems were later rectified with the creation of a new polarizable water model for the force field [28]. This new model consists of three particles; a central particle for the central mass and vdw sphere, as well as two other particles to hold a positive and negative charge to create an internal dipole. The resulting effect was an increase in the reproduction of experimental physical properties and electrostatic interactions. The screening dielectric constant and the antifreeze particles were no longer necessary to mend the lack of electrostatic interactions. Without the artificial screening dielectric constant applied to a membrane, the transport of charge into or through a membrane is able to be better reproduced [28].

Implicit water is the extreme in the case of efficiency, in which all water molecules are removed and replaced with one continuous medium. Implicit wa-

ter is extremely valuable for simulations where water accuracy can be traded off for computational efficiency. This is useful for simulations in which the overlying structure of the water or the interactions of the water-molecule interface are of little importance. Implicit water has also been applied to the Martini force field in an altered version named "Dry Martini", which is able to reproduce the effects of explicit water molecules [11].

References

1. Alders, B & Wainwright, T. Studies in Molecular Dynamics. I. General Method. *The Journal of Chemical Physics* **31,** 459–466 (1959).

2. Brooks, B & et. al. CHARMM: the biomolecular simulation program. *Journal of Computational Chemistry* **30,** 1545–1614 (2009).

3. Klauda, J. *et al.* Update of the CHARMM All-Atom Additive Force Field for Lipids: Validation on Six Lipid Types. *The Journal of Physical Chemistry B* **114,** 7830–7843 (2010).

4. Jambeck, J. & Lyubartsev, A. Derivation and Systematic Validation of a Refined All-Atom Force Field for Phosphatidylcholine Lipids. *The Journal of Physical Chemistry B* **116,** 3164–3179 (10 2012).

5. Shaw, D. *et al.* Anton, A Special-Purpose Machine for Molecular Dynamics Simulation. *Communications of the ACM* **51,** 91–97 (2008).

6. Hardy, D. *et al. Fast molecular electrostatics algorithms on GPUs* (Morgan Kaufmann Publishers, 2011., 2011).

7. Bowman, G. Accurately Modeling Nanosecond Protein Dynamics Requires at least Microseconds of Simulation. *Journal of Computational Chemistry* **37,** 558–566 (2016).

8. Havrila, M. *et al.* Microsecond-Scale MD Simulations of HIV-1 DIS Kissing-Loop Complexes Predict Bulged-In Conformation of the Bulged Bases and

Reveal Interesting Differences between Available Variants of the AMBER RNA Force Fields. *Journal of Physical Chemistry B* **119,** 15176–15190 (2015).

9. Espinoza-Fonseca, L. M. & Ramirez-Salinas, G. L. Microsecond Molecular Simulations Reveal a Transient Proton Pathway in the Calcium Pump. *Journal of the Americal Chemical Society* **137,** 7055–7058 (2015).

10. Van Eerden, F. J., de Jong, D. H., de Vries, A. H., Wassenaar, T. A. & Marrink, S. J. Characterization of thylakoid lipid membranes from cyanobacteria and higher plants by molecular dynamics simulations. *Biochimica et Biophysica Acta-Biomembranes* **1848,** 1319–1330 (2015).

11. Arnarez, C. *et al.* Dry Martini, a Coarse-Grained Force Field for Lipid Membrane Simulations with Implicit Solvent. *Journal of Chemical Theory and Computation* **11,** 260–275 (2015).

12. Ingolfsson, H. I. *et al.* Lipid Organization of the Plasma Membrane. *Journal of the Americal Chemical Society* **136,** 14554–14559 (2014).

13. Becke, A. A New Mixing of Hartree-Fock and Local Density Functional Theories. *Journal of Chemical Physics* **98,** 1372–1377 (1993).

14. Slater, J. A Simplification of the Hartree-Fock Method. *Physical Review* **81,** 385–390 (1951).

15. Mulliken, R. Electronic Population Analysis on LCAO-MO Molecular Wave Functions. I. *The Journal of Chemical Physics* **23,** 1833–1840 (1955).

16. Berger, O., Edholm, O. & Jahnig, F. Molecular Dynamics Simulations of a Fluid Bilayer of Dipalmitoylphosphatidylcholine at Full Hydration, Constant Pressure, and Constant Temperature. *Biophysical Journal* **72,** 2002–2013 (1997).

17. Risselada, J. & Marrink, S. The molecular face of lipid rafts in model membranes. *PNAS* **105,** 17367–17372 (2008).

18. Apajalahti, T. *et al.* Concerted diffusion of lipids in raft-like membranes. *Faraday Discussions* **144,** 411–430 (2010).

19. Krapf, S., Weber, S. & Koslowski, T. The road not taken: a theoretical view of an unexpected cryptochrome charge transfer path. *Physical Chemistry Chemical Physics* **14,** 11518–11524 (2012).

20. Ogata, S., Shimojo, F., Kalia, R., Nakano, A. & Vashishta, P. Environmental effects of H2O on fracture initiation in silicon: A hybrid electronic-density-functional/molecular-dynamics study. *Journal of Applied Physics* **95,** 5316–5323 (2004).

21. Zavadlav, J., Melo, M., Marrink, S. & Praprotnik, M. Adaptive resolution simulation of polarizable supramolecular coarse-grained water models. *The Journal of Chemical Physics* **142,** 244118 (2015).

22. Marrink, S., de Vries, A. & Mark, A. Coarse Grained Model for Semiquantitative Lipid Simulations. *The Journal of Physical Chemistry B* **108,** 750–760 (2004).

23. Marrink, S., Risselada, J., Yefimov, S., Tieleman, P. & de Vries, A. The MARTINI Force Field: Coarse Grained Model for Biomolecular Simulations. *The Journal of Physical Chemistry B* **111,** 7812–7824 (27 2007).

24. Monticelli, L. *et al.* The MARTINI Coarse-Grained Force Field: Extension to Proteins. *Journal of Chemical Theory and Computation* **4,** 819–834 (5 2008).

25. Lopez, C. *et al.* Martini Coarse-Grained Force Field: Extension to Carbohydrate. *Journal of Chemical Theory and Computation* **5,** 3195–3210 (12 2009).

26. Uusitalo, J. J., Ingolfsson, H. I., Akhshi, P., Tieleman, D. P. & Marrink, S. J. Martini Coarse-Grained Force Field: Extension to DNA. *Journal of Chemical Theory and Computation* **11,** 3932–3945 (2015).

27. Marrink, S. & Tieleman, P. Perspective on the Martini model. *Chemical Society Reviews* **42,** 6801–6822 (2013).

28. Yesylevskyy, S., Schafer, L., Sengupta, D. & Marrink, S. Polarizable Water Model for the Coarse-Grained MARTINI Force Field. *PLOS Computational Biology* **6,** 1–17 (2010).

29. De Jong, D. A Molecular View on the Organizational Complexity of Proteins in Membranes. *Retrieved from University of Groningen research database.* (2013).

30. Ingolfsson, H., Arnarez, C., Periole, X. & Marrink, S. Computational 'microscopy' of cellular membranes. *Journal of Cell Sciences* **0,** 1–12 (2016).

31. Shihu, W. & Ronald, L. Coarse-Grained Molecular Dynamics Simulation of Self-Assembly and Surface Adsorption of Ionic Surfactants Using an Implicit Water Model. *Langmuir* **31,** 1262–1271 (2015).

32. Gomez-Llobregat, J. & Linden, M. Anisotropic Membrane Curvature Sensing by Antibacterial Peptides. *Biophysical Journal* **108,** 550A (2015).

33. Lu, Y. & Salsbury, F. Recapturing the Correlated Motions of Protein Using Coarse-Grained Models. *Protein and Peptide Letters* **22,** 654–659 (2015).

34. Mustafa, G., Nandekar, P. P., Yu, X. & Wade, R. C. On the application of the MARTINI coarse-grained model to immersion of a protein in a phospholipid bilayer. *Journal of Chemical Physics* **143,** 243139 (2015).

35. Thomson Reuters, Web of Science. Retrieved 1 April 2016, from `https://www.webofknowledge.com/`.

36. Melo, M. N., Ingolfsson, H. I. & Marrink, S. J. Parameters for Martini sterols and hopanoids based on a virtual-site description. *Journal of Chemical Physics* **143,** 243152 (2015).

37. Risselada, H. J., Marrink, S. J. & Mueller, M. Curvature-Dependent Elastic Properties of Liquid-Ordered Domains Result in Inverted Domain Sorting on Uniaxially Compressed Vesicles. *Physical Review Letters* **106,** 148102 (2011).

38. Gautieri, A., Russo, A., Vesentini, S., Redaelli, A. & Buehler, M. J. Coarse-Grained Model of Collagen Molecules Using an Extended MARTINI Force Field. *Journal of Chemical Theory and Computation* **6,** 1210–1218 (2010).

39. Gobbo, C. *et al.* MARTINI Model for Physisorption of Organic Molecules on Graphite. *Journal of Physical Chemistry C* **117,** 15623–15631 (2013).

40. Van Oosten, B. & Harroun, T. A MARTINI extension for Pseudomonas aeruginosa PAO1 lipopolysaccharide. *Journal of Molecular Graphics and Modeling* **63,** 125–133 (2016).

41. Bereau, T. & Kremer, K. Automated Parametrization of the Coarse-Grained Martini Force Field for Small Organic Molecules. *Journal of Chemical Theory and Computation* **11,** 2783–2791 (2015).

42. Feller, S. An Improved Empirical Potential Energy Function for Molecular Simulations of Phospholipids. *The Journal of Physical Chemistry B* **104,** 7510–7515 (2000).

43. Jambeck, J. & Lyubartsev, A. An Extension and Further Validation of an All-Atomistic Force Field for Biological Membranes. *Journal of Chemical Theory and Computation* **8,** 2938–2948 (2012).

44. Jambeck, J. & Lyubartsev, A. Another Piece of the Membrane Puzzle: Extending Slipids Further. *Journal of Chemical Theory and Computation* **9,** 774–784 (2013).

45. Kucerka, N. *et al.* Molecular Structures of Fluid Phosphatidylethanolamine Bilayers Obtained from Simulation-to-Experiment Comparisons and Experimental Scattering Density Profiles. *Journal of Physical Chemistry B* **119,** 1947–1956 (2014).

46. Paloncyova, M. *et al.* Benchmarking of Force Fields for Molecule-Membrane Interactions. *Journal of Chemical Theory and Computation* **10,** 4143–4151 (2014).

47. Van Oosten, B. *et al.* Small molecule interaction with lipid bilayers: A molecular dynamics study of chlorhexidine. *Journal of Molecular Graphics and Modelling* **48,** 96–104 (2014).

48. Liu, W., Zhang, S., Meng, F. & Tang, L. Molecular simulation of ibuprofen passing across POPC membrane. *Journal of Theoretical & Computaional Chemistry* **13,** 1450033 (2014).

49. Berendsen, H, Grigera, J & Straatsma, T. The missing term in effective pair potentials. *Journal of Physical Chemistry* **91,** 6269–6271 (1987).

50. Jorgensen, W. & Madura, J. Solvation and Conformation of Methanol in Water. *Journal of the American Chemical Society* **105,** 1407–1413 (1983).

51. Mahoney, M. & Jorgensen, W. A five-site model for liquid water and the reproduction of the density anomaly by rigid, nonpolarizable potential functions. *The Journal of Chemical Physics* **112,** 8910–8922 (2000).

52. Rick, S. A reoptimization of the five-site water potential (TIP5P) for use with Ewald sums. *The Journal of Chemical Physics* **120,** 6085–6093 (2004).

53. Abascal, J & Vega, C. A general purpose model for the condensed phases of water: TIP4P. *The Journal of Chemical Physics* **123,** 234505 (2005).

54. van der Spoel, D., van Maaren, P. & Berendsen, H. A systematic study of water models for molecular simulation: Derivation of water models optimized for use with a reaction field. *The Journal of Chemical Physics* **108,** 10220–10230 (1998).

55. Kiyohara, K., Gubbins, K. & Panagiotopoulos, A. Phase coexistence properties of polarizable water models. *Molecular Physics* **94,** 803–808 (1998).

Chapter 2

Molecular Dynamics

2.1 GROMACS

There are several different molecular dynamics (MD) packages used for simulating biological systems, such as NAMD [1], CHARMM [2] and GROMACS [3, 4], to name a few. Although each has slight variations to the algorithms that they use, they all perform the same general operations to perform a MD simulation. GROMACS (GROningen MAchine for Chemical Simulations) is a versatile package to both perform and analyse MD simulations. Created at the University of Groningen, GROMACS first appeared in publication in 1995 [3]. It was built to be an efficient parallel implementation of a MD program for the use of biomolecules. It has remained a popular MD software, renown to be fast and utilizing the newest technologies to remain among the fastest of MD softwares available to date. Recent advancements in graphical processing units (GPU) have boosted the performance of MD simulations with its abundance of available threads for computations. Creating algorithms to take full advantage of the GPU's, GROMACS has benefited from an approximate 100 fold improvement in efficiency [5]. GPU acceleration is just one of many examples of acceleration

techniques GROMACS has implemented to boost its performance. Others include CPU acceleration (SSE, AVX, etc) as well as using software acceleration packages (BLAS, LAPACK, fftw, MPI, OpenMP, etc).

2.2 Energy Minimization (EM)

Often when the initial coordinates of a simulation are made, they contain a number of unfavourable conformations/interaction. These can lead to unrealistic forces and thus large movements in the atom positions, giving rise to unstable simulation environments. EM techniques are employed to initially relax the system such as using the steepest descent [6], conjugate gradient [1] or limited-memory Broyden-Fletcher-Goldfarb-Shanno quasi-Newtonian minimizer (L-BFGS) algorithms [7]. Although, all 3 options are available in the GROMACS software, the steepest descent algorithm is used most frequently due to its robustness and ease to implement [8].

The steepest descent algorithm calculates the new positions of the atoms using the gradient of the potential and a maximum step size utilizing the following:

$$\vec{r}_{n+1} = \vec{r}_n + \frac{-\vec{\nabla} V}{\max(|\vec{F}|)} h_n$$

where $\vec{r}$ is the position coordinate, h is the step size, V is the potential and $\max(|\vec{F}|)$ is the largest value of the force components. With the new configuration, the potential of the new positions is recalculated and compared with the previous configuration. If the new potential is lower than that of the previous step then

the new configuration is accepted or rejected otherwise. The algorithm then halts after either a predefined number of iterations or the maximum force gradient is reduced to a smaller value than a predefined value ϵ [8].

2.3 Molecular Dynamics (MD) Simulation

The process of a molecular dynamic (MD) simulation can be immensely complicated, however they can all be summarized into the following 4 general steps:

1 - Input (initial conditions)

$\Downarrow$

2 - Compute forces

$\Downarrow$

3 - Update configuration

$\Downarrow$

4 - Output

Each step may differ depending on the type of simulation, program used and preferred algorithms. Described below are the general components of each step with details focusing on the algorithms later utilized in the work provided in this thesis.

2.3.1 Input (Initial Conditions)

Before performing a simulation, a list of the coordinates (often called a topology) and velocities of each particle is required, as well as information about the box

size and boundaries. The initial topology of a system can be obtained in many different ways. Physically accurate structures can be found experimentally, or found in online libraries such as the protein database [9]. Structures are commonly constructed using a combination of techniques including NMR, scattering experiments and computational chemistry techniques such as density functional theory. Physically inaccurate structures can also be utilized as a first approximation, if and only if it is close enough to a reasonable structure that a MD simulation will pull it into a physically accurate conformation. This method is useful in building a membrane, where pre-equilibrated lipids of any type can be placed on lattice points to build a membrane with any combination of lipid types and in any concentration required. The membrane will not be in a physically accurate or equilibrated state however, it is close enough that it will relax into equilibrium through simulation. Two such programs are the CHARMM-GUI [10] for creating AA bilayers, and INSANE [11] for building CG membranes.

The initial velocities for the simulation can either be provided if continuing from a previous simulation or generated if the initial velocities are unknown. The component of each velocity of a particle v_i (for i=1..3N) are generated with a Maxwell-Boltzmann distribution for a given temperature (T) with the probability (P):

$$P(v_i) = \sqrt{\frac{m_i}{2\pi kT}} \exp(-\frac{m_i v_i^2}{2kT})$$

where m_i is the mass of the particle and k is Boltzmann's constant.

Information on the simulation box (size and boundaries) must be defined as well. The boundaries of the simulation can be solid, but in many cases are created

as periodic boundaries to minimize the edge effects of a finite system. Periodic boundaries create a simulation in a box, which is surrounded by translated images of itself to create a seemingly infinitely sized system. This however is not truly accurate, because any periodic effects such as membrane fluctuations must be contained within one unit cell, to satisfy the continuity boundary condition. Thus only an integer number of periodic wavelengths may take place inside the simulation box. There are multiple different box shaped for the use of periodic boundaries such as cubic or truncated octahedron. Each shape has its own distinct advantage depending on the simulation. For example a cubic boundary is preferable for a membrane with x, y, z dimensional symmetry, however the truncated octahedron is preferable for proteins which do not benefit from the x, y, z symmetry but do benefit from the reduced volume of the box, which requires less solvent and thus faster simulation times.

2.3.2 Computing Forces

With the set of initial conditions, a MD simulation can take place, which moves the system forward through time using Newtonian mechanics. When GROMACS computes the forces, it uses the potential energy of the system, which is split up into contributions from six terms:

$$V(\vec{r_1}, \vec{r_2}, ..., \vec{r_n}) = \sum_{\text{Bonds}} V_{\text{Bonds}} + \sum_{\text{Angles}} V_{\text{Angles}} + \sum_{\text{Dihedrals}} V_{\text{Dihedrals}} + \sum_{\text{Impropers}} V_{\text{Impropers}} + \sum_{\text{Coulomb}} V_{\text{Coulomb}} + \sum_{\text{LJ}} V_{\text{LJ}}$$

which are summed over the whole system. These potentials are split into two main categories: bonded(bonds, angles, dihedrals, and improper dihedrals) and

nonbonded interactions(Coulomb and Lennard-Jones). If two atoms are within the same molecule, connected by three bonds or less, the interactions are determined purely on the bases of the bonded interactions. For atoms not connected through a distance of at most three bonds, interactions are based off of the nonbonded interactions. There are multiple variations to the potential function used for each of the six terms. The function chosen for each potential, as well as the parameters for each is stored in the chosen force field.

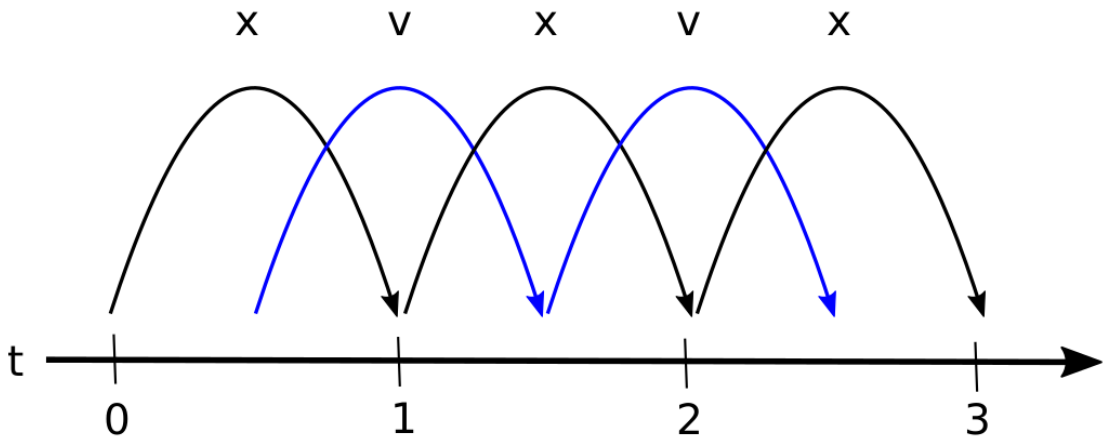

Figure 2.1: Visual representation for the leapfrog algorithm calculation of position (x) and velocity (v) "leapfrogging" over one another, with the position determined at every integer value and every velocity calculated at half inter values.

The force on each particle is calculated as:

$$\vec{F}_i = -\vec{\nabla} V \Big|_{\vec{r}_i}$$

The equations of motion are then computed using a chosen integrator. The default integrator in GROMACS is the leapfrog algorithm (See Figure 2.1) [8, 12], which uses the forces at time t to calculate the velocity at half time step intervals ($t + \frac{1}{2}\Delta t$) and positions at full step intervals ($t + \Delta t$), using the equations:

$$\vec{v}(t + \frac{1}{2}\Delta t) = \vec{v}(t - \frac{1}{2}\Delta t) + \frac{\Delta t}{m}\vec{F}(t)$$

$$\vec{r}(t + \Delta t) = \vec{r}(t) + \vec{v}(t + \frac{1}{2}\Delta t)\Delta t$$

These equations are then further modified for the correct temperature and pressure coupling controlled through the use of the selected thermostat or barostat, depending on the chosen ensemble of the system (see Ensambles section 2.3.5).

2.3.3 Bonded Potentials

Interactions between atoms connected within a distance of three bonds from another are calculated purely based on bonded potentials. There are three types of bonded interactions(see Figure 2.2): bonds (2-body interactions), angles (3-body interactions), and dihedral interactions (4-body interactions). Dihedral interactions are separated into two types, proper (named as simply "dihedral") and improper dihedrals, which keeps the planarity of groups such as aromatic rings, to prevent them from flipping to their mirror images. In Figure 2.2 d) the improper dihedral interaction acts between planes made by atoms ijk and jkl.

The most common bonded potential is represented as a harmonic function such as V_{Bond} for the length of a chemical bond:

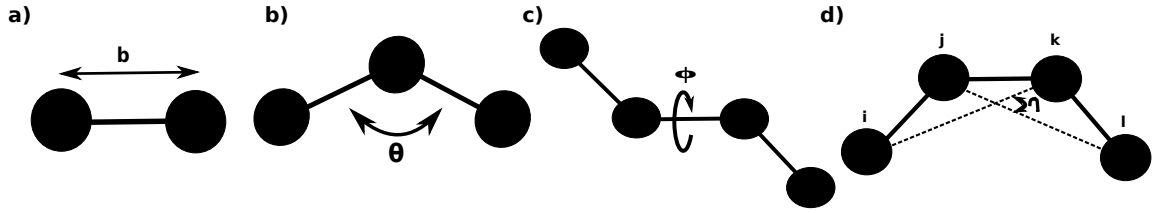

Figure 2.2: Bonded interactions - a) bonds (2-body bond interaction), b) angles (3-body angle interaction), c) dihedrals (4-body interaction) d) improper dihedral (4-body interaction).

$$V_{\text{Bond}} = \frac{1}{2}k_b(b - b_0)^2$$

where k_b is the strength of the spring, b is the distance between the two particles and b_0 is the equilibrium distance between them(Figure 2.2 a)). Similarly, the V_{Angle} and V_{Improper} function use harmonic functions:

$$V_{\text{Angle}} = \frac{1}{2}k_\theta(\theta - \theta_0)^2$$

$$V_{\text{Improper}} = \frac{1}{2}k_\eta(\eta - \eta_0)^2$$

with spring strengths (k_θ, k_η) keeping the angles (θ, η) about their equilibrium angles (θ_0, η_0) as in Figure 2.2 b) and d). Dihedral potential functions can not be fit to a simple harmonic function since they are periodic around a rotation of 360°. Thus, the V_{Dihedral} is fit to a sum of n sinusoidal functions:

$$V_{\text{Dihedral}} = \sum_{n=1}^{n} k_\phi(1 + cos(n\phi - \phi_o))$$

where k_ϕ is the amplitude of each sinusoidal function, ϕ is the current angle made by the dihedral, and ϕ_0 is a phase shift(Figure 2.2 c)), determining the location of the sinusoidal minimum.

2.3.4 Nonbonded Potentials

Nonbonded interactions are more complicated than the bonded potentials due to the fact that they depend on atom types as well as their proximity to each other. If two atoms are connected within 3 bonds of each other in a molecule, then the non bonded interactions are ignored and their interactions are based solely on their bonded interactions. Similarly, if the particles are too far apart, beyond a set cutoff, the interactions are negligibly small and not calculated. For pairs of particles within a defined cut off distance, and not connected within 3 bonds, electrostatic ($V_{Coulomb}$) and Lennard-Jones (V_{LJ}) potentials are calculated. The electric potential between particles i and j is calculated using Coulomb's law:

$$V_{Coulomb} = \frac{q_i q_j}{4\pi\epsilon r_{ij}}$$

where q_i and q_j are the charges of the two particles, ϵ is the dielectric constant and r_{ij} is the distance between them. The potential energy due to Lennard-Jones interactions (synonymous with van der Waals interactions) is calculated based on a 12-6 potential:

$$V_{LJ} = \frac{C_{ij}^{(12)}}{r_{ij}^{12}} - \frac{C_{ij}^{(6)}}{r_{ij}^{6}}$$

The parameters $C_{ij}^{(12)}$ and $C_{ij}^{(6)}$ are constants, depending on the atom types, the size of the two particles as well as the strength of attraction between them.

Nonbonded pair interactions are a computationally expensive to calculate. For a system of N particles, there are $N(N-1)/2$ pair interaction. As the system size grows, the amount of pair calculations increases proportional to N^2. The amount of pair interactions is increased with the use of periodic boundary conditions, where the amount of particles is increased to an infinite amount. It is therefore both illogical and impossible to calculate these forces explicitly as such. To avoid this problem, a select cutoff distance for the nonbonded interactions is used, where all interactions outside of this rage are considered negligibly small. A list of atoms within this cutoff range are kept, and updated so that the algorithm can run much more effectively in this short cutoff region of each atom. At the edge of this cutoff range, either the forces or the potential can be shifted to zero. This is done either as a sudden hard cutoff, a downward shift in the whole function, or a softer switched cutoff which slowly brings the function to zero over an extended distance of a few angstroms from the desired cutoff distance.

The long range interactions, while much weaker than the short range interactions, still contribute to the forces and free energy calculations. A correction term to the long range contribution to the dispersion interaction can be derived analytically and added to both the energy and pressure of the simulation to account for this correction. Long range electrostatics are calculated through the use of Ewald summation. Particle Mesh Ewald summation interpolates charges onto a grid, which is then Fourier transformed to determine the energy term. The potential

at the grid points can then be calculated through the inverse transformation [13, 14].

2.3.5 Ensembles

There are many different types of ensembles that can be chosen for a MD simulation. The ensemble is defined by the properties of the system that are held constant. The most commonly used are NVE, NVT, NPT and NPγT. The NVE (microcanonical) ensemble is the most basic ensemble to simulate, since a simulation with a fixed number of particles in a box at a set energy is by definition an NVE ensemble. The additional coupling of a temperature bath, can add fluctuations to the energy, while keeping a constant temperature, creating an NVT (canonical) ensemble. Similarly a pressure bath can be coupled to the box walls to make the volume dynamic creating an NPT ensemble. NPγT is a special ensemble used in bilayer simulations [15–18] where an NPT simulation does not accurately reproduce the lipid properties such as membrane thickness or area per lipid. An artificial surface tension can be applied through an NPγT ensemble to achieve the correct experimental values [15].

Controlling the temperature of a simulation involves changing the velocities of the atoms in the system, since temperature and velocities can be related through the equipartition theorem:

$$T = \frac{1}{N_f k_b} \sum_i m_i |\vec{v}|_i^2$$

where N_f is the number of degree of freedom in the system (equal to $3N - 3$), k_b is Boltzmann's constant and $m_i, \vec{v}_i$ are the mass and velocities of each of the atoms. Velocity rescaling is a trivial method for controlling velocities where every N steps the system temperature is calculated using the equipartition theorem and the velocities are all rescaled appropriately so that the total system temperature is at the desired temperature [19]. This causes significant instantaneous perturbations to the system and therefore do not represent any physical ensemble. It is therefore mainly used only for energy minimizations and not runtime MD simulations.

Berendsen [20, 21] and Nose-Hoover [22, 23] thermostats take a much more physical approach by coupling the system to an external heat bath. The Berendsen thermostat scales the velocities proportionally to the difference in temperature from the desired temperature so that the system approaches the desired temperature exponentially. This method is extremely useful for bringing a system to a desired temperature but does not recreate a proper ensemble. A proper physical ensemble can be recreated by the Nose-Hoover thermostat which adds a frictional term to the equations of motion, which allows the for temperature fluctuations. The temperature of the system fluctuates, but the frictional term is coupled to a heat bath so that the total temperature of the combined system and heatbath is conserved.

Similar to how temperature thermostat coupling is used to control the system temperature, pressure barostat control the system pressure. Berendsen barostat changes the dimension of the simulation box as well as the position of the atoms

so that the system is driven to the appropriate pressure [20]. Although this produces the correct average pressure, it does not yield a physical NPT ensemble. For a true NPT ensemble, Parrinello-Rahman pressure coupling is used. This approach applies a modification to the equation of motion to include the box boundaries in order to couple the pressure of the system [24, 25].

2.3.6 Update Configuration and Output

After the equations of motion have been solved with the proper alterations to include proper thermostat/barostat control for the appropriate ensembles, the positions and velocities of the atoms are updated to the new time $t = t + \delta t$. The positions and velocities are saved to a trajectory file as often as necessary for the simulation. Saving both positions and velocities every step is often redundant since the steps are so small that there is little change from one step to another and this creates a very large amount of data to be stored. Furthermore, it is also unwise to save trajectories too infrequently, as there will be large jumps in atom positions and could lead to insufficient statistics.

2.4 Potential of Mean Force (PMF)

The potential of mean force (PMF) is a calculated potential that would reproduce the mean force of a system given by $\vec{F} = -\vec{\nabla}V$, first introduced in 1935 by Kirkwood [26]. The PMF can be used as a measure of how the free energy changes as a function of a given reaction coordinate. For example, a PMF curve

for two atoms along a reaction coordinate being the distance between the two would yield the Lennard-Jones potential. Common uses include a free energy map along a chemical reaction and binding or unbinding events [27, 28].

It is difficult to calculate the PMF from a regular unbiased MD simulation due to the statistical nature of a system wanting to spend a majority of its time in the lowest energy state. Similarly, energy barriers may trap a system in an unfavourable conformation. Therefore there are too few statistics inside the phase space regions of energetically unfavourable conformations. To overcome this difficulty several methods of special sampling techniques have been developed to calculate the PMF from MD simulations. The system must be in some way biased so that the energetically unfavourable conformation become more favourable. One such method to overcome small energy barriers is replica-exchange, often associated with proteins and protein folding. Replica-exchange overcomes small energy barriers by exchanging replicas from multiple ensembles at different temperatures [29, 30]. To explore the energy landscape between states with a large energy difference the system must be altered by means of an external bias potential to increase the sampling of the energetically unfavourable conformations.

Bias potentials may be introduced into the system by a number of approaches either dynamically or quasi statically. Standard dynamic methods bias the system by steering the position of a particle giving it either a constant force or a constant velocity. A third type of dynamic approach is the oscillating forward-reverse method by Holland et al. [31], which adds an oscillatory term to the constant velocity method. These dynamic methods force the particle through a reaction

coordinate at a slow enough rate to sufficiently measure all points along the reaction coordinate for proper statistical analysis.

A quasi static bias relies on an ensemble of systems, each with the particle constrained to different small sections of a reaction coordinate. This is done by creating snapshots of the particle at different points along the reaction coordinate and holding it there with a biassing potential. The initial snapshots can be created by pulling a particle in through the reaction coordinate at constant rate, taking snapshot frames at equally spaced time intervals or by letting the particle naturally follow the reaction coordinate (if and only if it is an energy favourable reaction) and taking frames at equally spaced distances along the reaction coordinate [32]. Either of the two methods end up with an ensemble of systems with the particle at varying distances along the reaction coordinate in which to determine the PMF.

To keep the particle in a region of poor sampling a constraining harmonic potential term:

$$V = \frac{1}{2}K(R - R_o)^2$$

is added to the hamiltonian of the system, keeping its position (R) close to the original starting position in the ensemble (R_o) with a spring constant (K). This confines the sampling of the particle to a small region of space in the reaction coordinate.

The resulting ensemble of systems are biased so that the probability of finding the particle at location x along the reaction coordinate is given by the equation:

$$P(x) = \frac{\sum_i^{N_{sims}} n_i(x)}{\sum_i^{N_{sims}} N_i exp\left(\frac{F_i - U_{bias,i}(x)}{k_b T}\right)}$$

Where $P(x)$ is the probability, N_{sims} is the number of independent simulations in the ensemble, $n_i(x)$ is the number of counts the particle was found in the bin at position x, $U_{bias,i}(x)$ is the biased potential of simulation i and F_i is the free energy shift from the ensemble simulation i. The free energy shift of each simulation in the ensemble is given by:

$$F_i = -k_b T ln\left(\sum_{bins} P(x) exp(\frac{-U_{bias,i}}{k_b T})\right)$$

The pair of equations for the unbiased probability $P(x)$ and free energy F_i are a set of self consistent equations. Solving this pair of equations to find the free energy shift of the system can be done using the weighted histogram analysis method (WHAM), if there is sufficient overlap in the ensembles. The WHAM method solves these equations by iteration to self consistency.

An example of the PMF curve for the free energy as a function of the reaction coordinate is given in Figure 2.3. In this example the center of mass of one cholesterol molecule was pulled into a membrane of DMPC lipids with the reaction coordinate being linear distance between it and the center of mass of the methyl group of the lipid tails. Because it is the free energy shift and not the actual energy values that are calculated, an arbitrary constant can be added so that any point of the curve can be assigned the value of zero energy (being 4nm, located in the water for this example). With the example of a membrane bound

molecule there are three important values that can be obtained from the PMF curve: the equilibrium position (Z_o), the energy of insertion (ΔG_i) and the energy to cross through the membrane center (ΔG_{ff}).

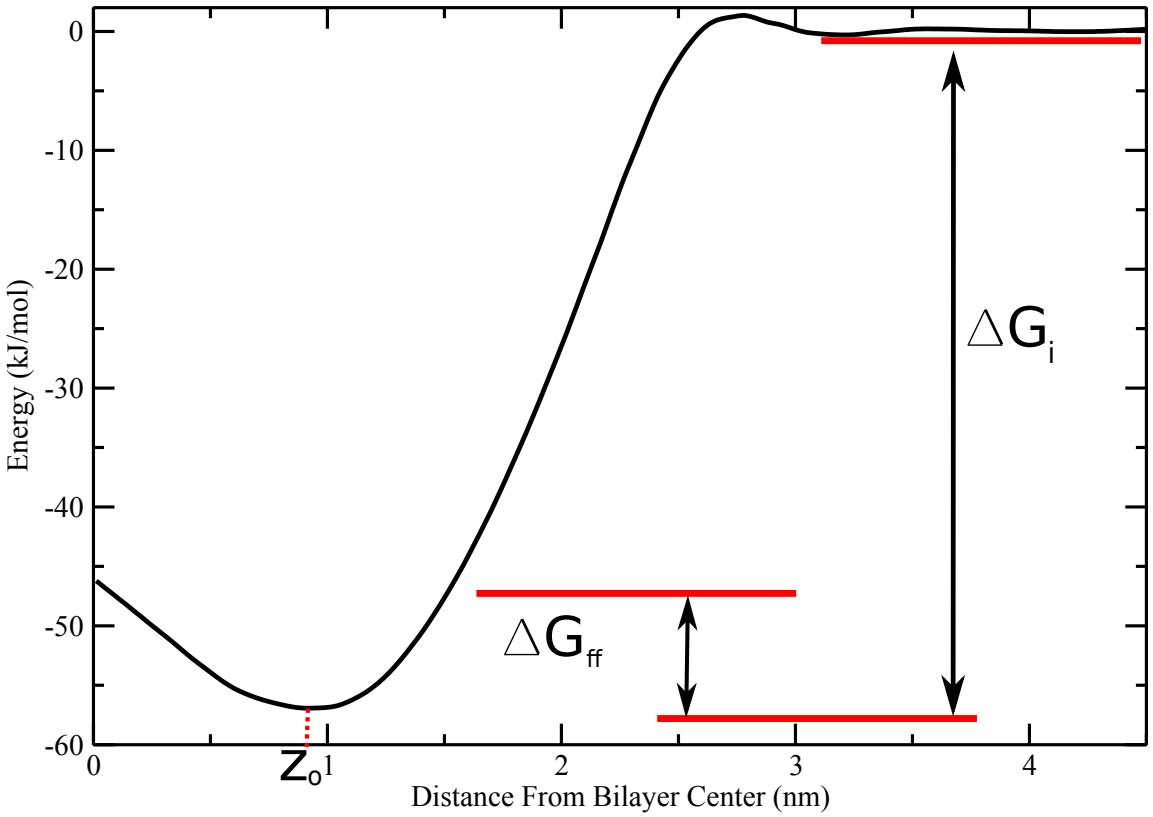

Figure 2.3: A general example of a PMF curve created for cholesterol in a DMPC membrane. Z_o is the minima, representing its equilibrium distance from the bilayer center, ΔG_{ff} is the amount of energy needed to move from one side of the membrane, through the center, into the other side and ΔG_i is the energy difference from outside the membrane to its equilibrium depth.

Typically uncertainties are identified by obtaining a value several times to calculate the standard deviation of the values. This procedure applied to a PMF

curve would require an unreasonably large amount of computation since data set requires an ensemble consisting of many simulations. Therefore the bootstrap method was tested as an effective alternative. A study on the bootstrap analysis method has shown it to be a comparable technique resulting in a reasonable measure to the uncertainty of the PMF comparable to rerunning and recalculating the PMF multiple times. The main flaw of this method is that it can not distern any uncertainties caused by the system being stuck in a local energy minima [33].

Bootstrapping is a common method used in statistical analysis to estimate the uncertainty in a sample of data [34, 35]. The bootstrapping method involves taking a set of N values and from it taking N points at random allowing for duplication. This creates "fake" data sets which are used to recalculate the PMF in order to calculate the uncertainty. The variance calculated from these fake data sets can give an estimate their homogeneity. However, this method assumes that the original data set is large and representative of the whole system. It can not tell for example if the data is missing important regions of phase space.

This method is problematic for calculating the PMF along a reaction coordinate. Selection at random has the possibility of introducing gaps in the data set, which in turn introduces defects in the calculated PMF. Therefore, the Bayesian bootstrapping method is implemented in GROMACS package g_wham, in order to avoid any possibility of gaps when randomly choosing points. Bayesian bootstrapping is a method which takes all of the positions inside of a histograms of position distributions and gives them random weightings unique in each bootstrap iteration. This then generates a new data set, based on the original which

uses all points, ensuring that there are no gaps in the calculation of the PMF [33]. The accuracy of the bootstrapping method to calculate the variance, increases with the number of bootstraps performed in the calculation. It is therefore limit by the computational resources available. The number of bootstraps recommended is at least 100 [33–35].

References

1. Phillips, J. *et al.* Scalable molecular dynamics with NAMD. *Journal of Computational Chemisrty* **26,** 1781–1802 (2005).
2. Brooks, B & et. al. CHARMM: the biomolecular simulation program. *Journal of Computational Chemistry* **30,** 1545–1614 (2009).
3. Berendsen, H, van der Spoel, D & van Drunen, R. GROMACS: A message-passing parallel molecular dynamics implementation. *Computer Physics Communications* **91,** 43–56 (1995).
4. Van Der Spoel, D *et al.* GROMACS: Fast, flexible, and free. *Journal of Computational Chemistry* **26,** 1701–1718 (2005).
5. Kutzner, C *et al.* Best bang for your buck: GPU nodes for GROMACS biomolecular simulations. *Journal of Computational Chemistry* **36,** 1990–2008 (2015).
6. Fletcher, R & Powel, M. A rapidly convergent descent method for minimization. *Computer Journal* **6,** 163–168 (1963).
7. Shanno, D & Kettler, P. Optimal Conditioning of Quasi-Newton Methods. *Mathematics of Computation* **24,** 657–664 (1970).
8. van der Spoel, D *et al.* Gromacs User Manual version 4.5.4. *www.gromacs.org* (2010).
9. Lab, B. N. Protein Data Bank. *Nature New Biology* **233,** 223 (1971).

10. Jo, S., Kim, T., Iyer, V. & Im, W. CHARMM-GUI: A web-based graphical user interface for CHARMM. *Journal of Computational Chemistry* **29,** 1859–1865 (2008).

11. Wassenaar, T., Ingolfsson, H., Bockmann, R., Tieleman, P. & Marrink, S. Computational Lipidomics with insane: A Versatile Tool for Generating Custom Membranes for Molecular Simulations. *Journal of Chemical Theory and Computation* **11,** 2144–2155 (2015).

12. Hockney, R, Goel, S & Eastwood, J. Quiet High Resolution Computer Models of a Plasma. *Journal of Computational Physics* **14,** 148–158 (1974).

13. Darden, T, York, D & Pedersen, L. Particle mesh Ewald: An Nlog(N) method for Ewald sums in large systems. *Journal of chemical Physics* **98,** 10089–10089 (1993).

14. Essmann, U *et al.* A smooth particle mesh ewald potential. *Journal of chemical Physics* **103,** 8577–8592 (1995).

15. Klauda, J. *et al.* Update of the CHARMM All-Atom Additive Force Field for Lipids: Validation on Six Lipid Types. *The Journal of Physical Chemistry B* **114,** 7830–7843 (2010).

16. Feller, S & R, P. On simulating lipid bilayers with an applied surface tension: periodic boundary conditions and undulations. *Biophysical Journal* **71,** 1350–1355 (1996).

17. Klauda, J, Brooks, B, MacKerell, A, Venable, R & W, P. An ab Initio Study on the Torsional Surface of Alkanes and Its Effect on Molecular Simulations of

Alkanes and a DPPC Bilayer. *Journal of Physical Chemistry B* **109,** 5300–5311 (2005).

18. Jo, S, Lim, J J anf Klauda & Im, W. CHARMM-GUI Membrane Builder for Mixed Bilayers and Its Application to Yeast Membranes. *Biophysical Journal* **97,** 50–58 (2009).

19. Bussi, G, Donadio, D & Parrinello, M. Canonical sampling through velocity rescaling. *The Journal of Chemical Physics* **126,** 014101 (2007).

20. Berendsen, H, Postma, J, van Gunsteren, W, DiNola, A & Haak, J. Molecular dynamics with coupling to an external bath. *The Journal of Chemical Physics* **81,** 3684–3690 (1984).

21. Berendsen, H. Transport Properties Computed by Linear Response through Weak Coupling to a Bath. *Computer Simulations in Material Science* **205,** 139–155 (1991).

22. Nose, S. A molecular dynamics method for simulations in the canonical ensemble. *Molecular Physics* **52,** 255–268 (1984).

23. Hoover, W. Canonical dynamics: equilibrium phase-space distributions. *Phys. Rev. A* **31,** 1695–1697 (1985).

24. Parrinello, M & Rahman, A. Polymorphic transitions in single crystals: A new molecular dynamics method. *Journal of Applied Physics* **52,** 7182–7190 (1981).

25. Nose, S & Klein, M. Constant pressure molecular dynamics for molecular systems. *Molecular Physics* **50,** 1055–1076 (1983).

26. Kirkwood, J. G. Statistical Mechanics of Fluid Mixtures. *Journal of Chemical Physics* **3,** 300–313 (1935).

27. Lemkul, J. & Bevan, D. Assessing the Stability of Alzheimer's Amyloid Protofibrils Using Molecular Dynamics. *J. Phys. Chem. B* **114,** 1652–1660 (2010).

28. MacCullum, J., Bennett, D. & Tieleman, P. Transfer of Arginine into Lipid Bilayers is Nonadditive. *Biophysical Journal* **101,** 110–117 (2011).

29. Sugitaa, Y. & Okamoto, Y. Replica-exchange molecular dynamics method for protein folding. *Chemical Physics Letters* **314,** 141–151 (1999).

30. Swendsen, R. & Wang, J. Replica Monte Carlo Simulation of Spin-Glasses. *Physical Review Letters* **57,** 2607–2609 (1986).

31. Holland, B., Vafaei, S. & Tomberli, B. Computer data analysis of the oscillating forward-reverse method. *Journal of Computational Physics* **231,** 4355–4364 (1935).

32. Trzesniak, D., Kunz, A. & van Gunsteren, W. A Comparison of Methods to Compute the Potential of Mean Force. *ChemPhysChem* **8,** 162–169 (2007).

33. Hub, J., de Groot, B. & van der Spoel, D. g_wham-A Free Weighted Histogram Analysis Implementation Including Robust Error and Autocorrelation Estimates. *Journal of Chemical Theory and Computation* **6,** 3713–3720 (2010).

34. Efron, B. & Tibshirani, R. *An introduction to the bootstrap / Brad Efron, Rob Tibshirani.* ISBN: 0412042312 (New York : Chapman & Hall, 1993., 1993).

35. Wehrens, R., Putter, H. & Buydens, L. The bootstrap: a tutorial. *Chemometrics and Intelligent Laboratory Systems* **54,** 35–52 (2000).

Chapter 3

Small molecule interaction with lipid bilayers: A molecular dynamics study of chlorhexidine

3.1 Introduction

Molecular dynamics (MD) simulations have become one of the powerful techniques to analyze the dynamic motion and gross structure of bio-membranes. MD simulations can reproduce the experimental environment of molecules in a computer and provide atomic-level information not detected in experiments. Over the last two years, more advanced force fields specific for lipid molecules have been developed, with experimental results in mind. Mainly, simulations are verified if they can properly reproduce NMR S_{CD} order parameters as well as neutron and x-ray scattering form factors [1–3].

Atomistic molecular dynamic simulations have tremendous utility for providing quantitative thermodynamic and mechanistic analysis of small molecule-lipid interactions. However, the typical time scale of such large simulations are below

200 ns, somewhat insufficient to detect larger molecule displacements or to obtain complete conformational sampling. Such simulations are made all the more difficult when looking for the effects of high concentration of the molecule, which only lengthens the computational time. This can preclude answering the typical key question of a membrane-active compound; where does a given solute reside within a bilayer and what factors govern its membrane binding or partitioning at equilibrium?

Coarse grained force fields have the advantage of having a simplified version of the modelled system which gives it the leverage of needing less computational time, leading to larger and longer simulations. However, coarse grain models have fared much worse in reproducing the thermodynamics of charged molecule-membrane interactions as a function of its protonation state, such as the case of the amino acid arginine important for ion channel modelling [4]. Although it is rare for a particular force field to be able to reproduce every known system, it is important to understand their limitations.

Biguanides are an important class of compounds, which resemble arginine, having multiple tautomers and protonation states. Their particular structure have shown to have extensive medical applications. Proguanil (an antimalarial agent) and Metformin (an antidiabetic compound) are biguanide derivatives, which are available as drugs [5, 6]. Other important compounds in this series are phenformin, buformin, chlorophenylbiguanide, and chlorhexidine. Apart from the well-established antidiabetic and antimalarial effects, biguanide derivatives have been shown to exhibit antimicrobial, antiviral, and antiplaque effects and

also have been known to influence gastric acid secretion [7–9].

We wanted to test the capability of one new lipid force field using data from neutron scattering to predict the partition location of the biguanide derivative drug chlorhexidine (CHX), shown in Figure 3.1. This elongated flexible molecule presents an interesting biophysical modelling challenge with seemingly contradictory components. It is symmetrically composed of a (hydrophobic) hexane linker joining two (polar, hydrophilic) biguanides and (lipophilic) chlorophenyl rings. CHX does not readily dissolve in aqueous solution. It is therefore commonly prepared as CHX digluconate, which allows it to be water soluble and importantly the gluconic acid dissociates with CHX easily so that it can readily interact with a cell membrane [10]. We expect the free-energy competition between these subunits to determine the location of the CHX within a bilayer. We have previously experimentally established the location of the hexane of CHX in DMPC, at two high molar concentrations of 10:1 and 3:1 DMPC:CHX, using neutron diffraction in a manner that yields the time-averaged distribution within the bilayer.

The pKa in water of the similar compound, poly(hexa-methylene-biguanide hydrochloride) (PHMB), was estimated to be around 13.5, meaning in aqueous solution at pH 7, PHMB will most likely exist in its +1 ionized form. Modelling studies have further showed that the most stable form of PHMB is one that has the +1 charge delocalized over the whole biguanide section, as would occur in the conjugated tautomer [11]. For CHX, the pKa of the singly ionized form was estimated to be 10.15, and doubly ionized at 9.55 [12]. The lower pKa indicates the

biguanide in CHX is easier to deprotonate, but harder to protonate, than PHMB. The chlorophenyl is less electron donating than an alkyl group and therefore is comparatively electron withdrawing; withdrawing electron density will make the adjacent N atom more difficult to protonate [12].

However, the pKa of CHX or any biguanide has not been estimated when in an apolar environment. Only recently has it has been shown that the amino acid arginine may remain at least fractionally protonated even when in a low dielectric lipid hydrocarbon environment, although without some form of stabilization from additional negative amino acids or lipid molecules, there is significant disruption to the membrane structure as macroscopic quantities of water associate with the charge inside the normally hydrophobic region [4, 13, 14]. Since our system does not include such a stabilizing negative charge, nor do we see evidence of bulk water in the membrane, we began with the assumption that CHX is neutral, however we tested the +1 and +2 charge forms as well.

We wish to answer the following questions; can a CHX molecule find an equilibrium location in the bilayer (without prior knowledge) within a reasonable simulation time? What are the effects of adding additional charge to the CHX molecule? What are the effects of high concentration of CHX on the limited-sized simulation, and can those perturbations reproduce the experimental results?

3.2 Computational Methods

We constructed an all-atom force field of chlorhexidine from the CHARMM36 force field [15–17] using well established parameters of certain amino acids [18]. Breaking the molecule into three sections as shown in Figure 3.1; the chlorophenyl ring (CPL), biguanide (BGU) and hexane (HEX), for which we selected the bond lengths, angles and torsions from Tyr, Arg, and Lys respectively.

Partial charges were calculated using GAUSSIAN software [19] and methods used for refining all-atom force fields [1]. The partial charges taken from the amino acids Tyr, Arg and Lys to create a first approximation model of chlorhexidine. This model was simulated in a box of methanol to produce a dielectric constant similar to that of the headgroup region of lipids where the molecule has been experimentally observed to reside [20]. The simulation was run for 1 ns, where 500 different snapshots of the molecule were taken 2 ps apart. For each conformation, atomic charges were computed with the DFT method using B3LYP exchange-correlation functional with the cc-pVTZ basis set. The partial charges of each atom were then averaged over the 500 snapshots to achieve a partial charge that takes into account the distribution of conformations during a simulation in a lipid system. The newly obtained charges were then used in the structure of chlorhexidine for further simulations.

Additional information is required for an accurate representation of the bond structure and chemistry of the biguanide sections. Bond resonance has been a topic of much study, including theoretical studies of guanides and biguanides. [21–23]. The general consensus from these quantum chemistry calculations is that the

configuration of the most stable neutral tautomer is characterized by conjugative interaction of the π-bonds, leading to alternating single and double bonds along the backbone, and therefore no hydrogen atom on the central nitrogen atom N3 (See Figure 3.1). This means two hydrogen attached to each of the N2 and N4 nitrogen, and the final hydrogen then rests on either N1 or N5. Placing it on N1 fixes the double bonds to be between C2-N3 and C4-N5. The alternative tautomer would likely be entirely equivalent. A +1 charged CHX involves placing an additional hydrogen on the N5 of just one of the ends of the molecule, and a +2 charge would place a hydrogen on the N5 of both biguanide sections.

An initial 3D structure of the neutral, +1, and +2 charged chemical schematics shown in Figure 3.1 was constructed using the OpenBabel [24, 25] from the appropriate SMILES representation, and then refined by hand in the software Avogadro [26]. The structure was then optimized using self-consistent field theory with closed-shell restricted Hartree-Fock (RHF) wavefunctions to the level of 6-31G* with the software NWChem [27]. The final bond lengths did not differ by more than 0.05 nm from those of the CHARMM36 force field. The final topology of CHX can be found in the supplementary information.

The topology of 1,2-dimyristoyl-3-*sn*-phosphatidylcholine (DMPC) was obtained from the Stockholm lipids website [1, 2]. Initial coordinates of a 128-lipid DMPC bilayer in an 8x8x2 configuration were obtained from CHARMM-GUI [28] with 30 TIP3P water molecules per lipid. The system was checked for correctness by running a pure bilayer simulation for 100 ns at 303 K and 323 K. Such lipid force fields are continually being validated and refined, and reproduce the

essential characteristics of pure lipid bilayers accurately [29, 30].

All simulations were performed using the GROMACS simulation software (version 4.6.1) [31] for 100 ns at 323 K followed by another 100 ns at 309 K, under periodic boundary conditions in a simple orthorhombic box. Systems containing charged CHX models were neutralized by adding Cl ions into the water in order to achieve a system with zero net charge. The temperature of the system was maintained by independently coupling the lipids, solvent, and CHX to an external temperature bath with a coupling constant of 1.0 ps using a Nose-Hoover thermostat. The pressure was kept at 1.013 bar in the lateral and normal directions independently by weakly coupling to a semi-isotropic pressure bath, using an isothermal compressibility of 4.5×10^{-5} bar^{-1} and a coupling constant of 10 ps.

A 2-fs time step with a Leap-Frog integrator was used. The Verlet list group scheme was used to for its optimal usage with GPUs for an increased simulation speed-up. The Verlet list scheme keeps a buffered list with exact cut-offs which are updated every 20 steps. Both the Coulomb and LJ potentials are shifted to zero with an exact cut-off value of 1.4 nm.

Neutron scattering is a technique to investigate the property of matter by scattering elementary particles called neutrons, off of the matter in which to investigate. In such a scattering experiment the neutron's momentum is altered when passing close to a nuclei. In elastic collisions, where no energy is transferred into the sample matter, the neutron is simply redirected by an angle θ. When studying membranes, ordered stacks of membranes are used as samples

to create a crystalline structure in the direction normal to the surface. In such a structure, Bragg peaks appear at values of θ caused by the reciprocal lattice spacing (equal to the distance between stacks of membranes). This condition has peaks at angles which satisfy the Bragg equation $n\lambda = 2dsin(\theta)$, where n is an integer (1,2,3...), λ is the neutron's wavelength and d is the reciprocal spacing.

Each nucleus scatters a neutron based off of its cross-sectional area. The total cross-section is the ratio of the total number of particles scattered to the flux of the incident beam, integrated over all directions $\sigma_{tot} = \int \frac{d\sigma}{d\omega} d\omega$. The neutron scattering length b is defined as $b^2 = \frac{d\sigma}{d\omega}$. So for a single nuclei, the total cross-section is $\sigma_{tot} = 4\pi b^2$. Since it is usually not possible to resolve individual atoms the concept of scattering length density is utilized which sums the scattering amplitude of all atoms within the volume. The scattering length density is calculated through the fourier transform of the structure factors obtained from the area under bragg peak as a result of the scattering experiment. A simulated neutron scattering length profile is calculated by determining the number density of each atom type in the simulation box along the z-dimension and multiplying the scattering length b for each specific element.

Since there is a difference in the scattering length of different isotopes, substitution of an element for another one of its isotopes can be done to create a label visible by this technique. Since biological samples contain a high number of hydrogen atoms ($b = -0.374 \times 10^{-12}$cm) they can be exchanged for deuterium ($b = 0.667 \times 10^{-12}$cm) to create a large contrast between the two samples. Subtracting the normalized scattering length density profiles of both labeled and

unlabeled samples should in theory leave behind only the distribution of the labeled section.

3.3 Results

Initially, two systems were constructed where a single neutral CHX was added to the simulation box, either outside the membrane in the water, or in the middle of the bilayer among the lipid terminal methyls. The latter case involves "exploding" the bilayer by artificially scaling the distance between lipids in each direction until sufficient room is made for the CHX, then slowly iterate between rescaling and energy minimization until the bilayer is reassembled. No lipids were removed. Solvating with water, and equilibration followed, as described above.

Figure 3.2 shows the the center of mass distribution for the hexane region of CHX during the subsequent 100 ns NPT runs at 323 K, for both simulations. In the course of reassembling the bilayer, the CHX starting from the centre was no longer quite in the center, but starting a location $\sim$ 0.2 nm higher, it quickly adopts a new location at $\sim$ 1 nm where it remains for the remainder of the simulation. The CHX started from the water however, continues to oscillate with nearly 1 nm amplitude in the water until $\sim$ 10 ns, at which point it begins to interact more strongly with the lipids. Just before $\sim$ 15 ns, it rapidly inserts into the bilayer, and the two systems become indistinguishable in structure and energy. CHX is clearly highly mobile in water phase, but reaches an equilibrium location

in the membrane interior that remains for the rest of the 100 ns simulation.

It is likely that at the end, both simulations reflect the free-energy minimum location of CHX in DMPC bilayers, and it is unlikely they will eventually come out of the bilayer with continuation of the simulation past 100 ns. Figure 3.2 also shows the system potential energy of the water-born CHX during the run. The potential energy change upon CHX insertion cannot be seen visually, however, following the methods of Schiferl and Wallace, level changes can be tested for statistical significance via sampling two regions of interest in the energy [32]. Testing whether the mean energy from 1 to 10.0 ns (from 10,000 data points), is different from the mean from 80 to 100 ns (from 20,000 data points) shows statistical significance ($p < 0.001$, Cohen's $d = 0.19$), whereas two different sets of data drawn from 1 to 4 ns and 4 to 8 ns are not statistically different ($p > 0.2$). Thus the CHX insertion can be seen from the noisy energy data as a small, but highly significant effect.

Confident an equilibrium position for CHX exists, and that a 100 ns time frame was sufficient, we constructed simulations of 4 and 12 CHX within a 128 lipid DMPC bilayer, where all the CHX begin in the water layer, equally divided on opposite sides of the bilayer. In order to facilitate the insertion of such a large number of molecules, the simulations were initially run for 100 ns at 323 K, before an additional 100 ns simulation was run at 303 K. Figure 3.3 shows the individual insertion of 12 CHX, beginning with four around 5 ns, and ending with the last insertion at 35 ns. Data shown are spline fits to reduce noise and provide clarity of the trend. No appreciable aggregation of the CHX was seen in the simulation,

although one could argue that after the first 4 molecules inserted, the others very quickly followed suit as a group. The drop in system energy is more clear in Figure 3.3, and the energy of insertion was calculated to be 706 ± 101 kJ/mol. This is less on a per molecule basis than the single CHX simulation, and probably a reflection of some inter-CHX association, as well as the partial insertion of 1-3 CHX at the end of the equilibration period and beginning of the simulation. At the end of the simulation the location of the twelve CHX seem to be randomly distributed between the center of the bilayer and 1.3 nm. We will show below that the full time- and system-averaged distribution of the CHX is more localized than Figure 3.3 would suggest. Simulations with a +1 and +2 charged CHX show qualitatively similar behaviour to the neutral case; insertion in the first 10-40 ns, with a concomitant decrease in system energy.

While not every case of a single CHX insertion passed statistical significance, every 323 K insertion of 4 and 12 CHX did. However, the size of the effect was small, and in Table 3.1 we present the spread of values of the energy of insertion calculated from a 4 ns range average at the simulation beginning versus the end. As expected, the energy of insertion of the more polar +2 charged CHX was less than +1 charged and neutral CHX, since the neutral CHX will sequester itself further from the water into the hydrocarbons than either the charged species. Below, we will confirm this.

Since the 303 K simulations followed on from the 323 K runs, we do not expect any change of state in the course of the run, and in fact, none of the very small changes in the energy level for the 1 or 4 CHX runs passed any statisti-

cal test for significance, indicating stable equilibrium and no energy drift over 100 ns. However, the 12 CHX at 303 K simulations showed a small but significant drift in energy, also shown in Table 3.1. At this high concentration and lower temperature, true equilibration may take longer than 100 ns. In this case, as we will see below, since the neutral CHX are more free to explore a greater region of the bilayer center, the energy drift is larger than the +2 charged CHX, which has established a much narrower distribution in the bilayer, indicative of less mobility. In either case, we do not expect any changes to our structural analysis below, as these energy drifts are so small, they can only be detected with statistical analysis.

The principle difference between the 1, 4, and 12 CHX simulations comes in the final insertion depth of CHX. To measure this, we compare our results with the neutron diffraction data from Komljenovic et al., where we determined the depth of deuterium labelled CHX hexane in DMPC at concentrations of 1:3 and 1:10 CHX:DMPC using crystallographic methods and isotopic labelling. [20] The simulation results are shown in Figure 3.4 as the time- and sample-averaged location of the CHX hexane hydrogen across the bilayer, in principle, a direct correspondence to the previous neutron diffraction experiments. In both the neutral or charged cases, there is a narrow, $0.6 - 0.8$ nm width Gaussian-shaped mass distribution of CHX in the bilayer.

For each CHX simulated, there is a small concentration dependence in the location of the CHX, and a more significant dependence on CHX charge. For the case of neutral CHX, the final position of the hexane is 0.8 nm from the bilayer

centre, although in the crowded environment of 12:128 CHX:DMPC, the extra CHX molecules find extra room in the center of the bilayer. Only at 303 K do we see the effect of reduced lipid chain motion forcing the CHX equilibrium location toward the bilayer center with increasing concentration. For the +1 and +2 charged cases, the charge pulls the CHX closer to the hydrophobic/hydrophilic interface, to a higher location of 1.1 and 1.3 nm respectively. At high concentrations, CHX is no longer crowded to the center of the bilayer, but rather increasing the amount of CHX moves them further out, towards the aqueous interface.

However, none of the simulations agree with the experimentally determined mass density of the same hexane deuterium label shown as the dashed line in the lower panel of Figure 3.4. In that case, we measured the hexane to be much higher in the membrane, at 1.6 nm from the bilayer center. The reason appears to be differences in the bilayer structure between simulation and experiment, and notably, the much deeper penetration of water into the simulated membrane. This has the effect of lowering the water interface, to which the CHX is clearly attracted, deeper into the bilayer.

Figure 3.5 shows the neutron scattering length density for the 1 and 12 CHX simulated systems, separated into bilayer and water components. Only half the bilayer is shown, starting from the central lipid methyls shifted to be at 0 nm, and extending to the water layer at the right. Neutron scattering length density is analogous to the more commonly measured electron density, with slight differences in the interpretation of Figure 3.5. The dip in signal in the bilayer center is due to the negative neutron scattering length of the CH_3 hydrogen. The

peak around 1.2-1.5 nm is not the high number of electrons of the phosphate, but rather is representative of the low density of hydrogen around the glycerol-ester backbone. [33]

Overall, there is little difference in the curve shapes between the simulations. The extra mass of the higher number of CHX can be seen in the curves of the 12 CHX over the 1 CHX. Most importantly, however, the bilayer experiences 0.3 nm thinning with the +2 charge over the neutral simulation. As the CHX moves from the bilayer center to the surface, the bilayer thins in response. In all cases the water layer shape remains roughly the same, showing two layers of hydration. The first layer penetrates into the bilayer to the level of the phosphates, and are the direct hydration of the choline headgroups (6-10 waters per lipid), and the remaining layer is bulk water.

We also include the experimental data of Komljenovic et al. in the lower panel of Figure 3.5 for the concentration of 1:10 CHX:DMPC at 309 K. [20] The bilayer data is obtained with a composition of 8% ^2H_2O, which renders the water "invisible" to neutrons and the resulting data is entirely due to scattering from only the lipids and CHX, directly comparable to the simulation data. We see that the structure of the bilayer interior is well simulated, however, the headgroups are broader and the bilayer is thicker. Repeating the experiment with higher concentration of ^2H_2O, and subtracting the results, gives the water profile shown in Figure 3.5. The experiment firmly rules out water penetrating deeply into the headgroups, effectively moving the hydrophilic/hydrophobic interface much higher in the bilayer, where the CHX follows suit.

To see this result more clearly, we compare simulations of pure DMPC without CHX to previously unpublished data on the distribution of water and two key components of the lipid bilayer; 1.) the hydrogen of the *sn*-1 acyl chain terminal methyl and 2.) the nine hydrogen of the choline methyl groups. (Experimental methods can be found in supplementary information.) Our simulations of pure DMPC bilayers reproduce the published results without issue, and the key parameters of the simulation, the area per lipid and bilayer thickness, are provided in Table 3.2. [1, 2] Figure 3.6 shows the distribution of these lipid groups (lower panel) and the overall bilayer and water (upper panel). We see that the distribution of terminal methyls are reproduced very well. The overall distribution of the choline methyl groups is not as well represented, the experiment indicating a 0.2 nm thicker membrane and slightly wider distribution. The same experimentally determined 0.2 nm thickness difference is seen also seen in the overall bilayer structure. Although the plateau in the acyl chain region is not as well defined in the simulation, the overall impression is a remarkable comparison between simulation and experiment on bilayer structure.

However, the experiment is unambiguous on the exclusion of inter-bilayer water from the phosphate region and below. If we define the hydrophobic/hydrophilic interface to be the half-max position of the water distribution, the experiment indicates that to be 1.9 nm, and the simulation at 1.6 nm. There are several important differences in the two systems that prevent a direct and fair comparison; lower hydration in the neutron diffraction, and poor experimental resolution in the validation of the simulation parameters, that may contribute to

this discrepancy, and which we will further review in the discussion.

Figure 3.7 shows the S_{CD} order parameters of averaged over both $sn-1$ and $sn-2$ tails for each CHX model. The order parameter was calculated as: $S_{CD} = \frac{3}{2}\langle cos^2(\theta)\rangle - \frac{1}{2}$, where θ for atom i is the angle made between the vector made by connecting the centres of atoms $i-1$ and $i+1$ and the bilayer normal. The simulation results slightly underestimates the experimental values for pure DMPC (upper frame) performed at 308 K, which is a known property of the Slipids force field [1]. The splitting of order parameter for the second carbon in the *sn*-2 chain is not well reproduced, however, the overall underestimation of S_{CD} indicates the lipids are more, rather than less, disordered and all in the L_α phase.

The effect of CHX on the order parameter of the lipid chains was negligible at the lower concentrations and only showed deviation from the pure DMPC system at the highest 12:128 concentrations. The change in disorder of the acyl chains was also dependent on the charge of the CHX. The neutral CHX exhibits an ordering effect on the DMPC chains, which is in complete contrast to the charged models which lower the chain order. The difference in the effect between the +1 and +2 charge are minimal with the +2 charge affecting the chains at a slightly higher position than the +1 charge CHX, due to its higher equilibrium position.

In the lower panel of Figure 3.7, we show previously unpublished experimental NMR lipid order parameters for 10:1 CHX in DMPC at 308 K. (NMR experimental methods can be found in supplementary information.) The simu-

lations achieve very good agreement in magnitude and shape of the curve. The simulations slightly overstate the values of S_{CD} for carbons 4 through 11.

Order parameters for the six carbons at the central HEX group of CHX were also calculated. The results however did not give any further insight, with unchanging values of approximately 0.12 to 0.14 for each carbon at all concentrations and charges.

The hydrogen atoms in the biguanide section of CHX act as hydrogen bond donors with the ability to establish hydrogen bonds with the oxygen atoms of the lipid molecules. The lifetime of these hydrogen bonds has been observed to be on the order of the length of the simulations. Figure 3.8 shows the minimum distance between the hydrogen on the BGU section of the +1 CHX and the lipid phosphate oxygen at 323 K. After the insertion of the molecule, the hydrogen atom stays at a close $\sim$ 0.2 nm from the lipid oxygen atom, with small jumps where it switches from lipid to lipid.

Table 3.3 shows the average number of hydrogen bonds made during the last 50 ns of each simulation, after all of the CHX molecules have inserted into the bilayer. The neutral CHX makes on average 1.5 hydrogen bonds per molecule once inserted into the membrane. The charged CHX models have additional hydrogen atoms, which allow for additional bonds to be made with the lipids. The +1 charge CHX molecule makes an average of 2.5 hydrogen bonds, while the +2 CHX makes 3.5. As the concentration of CHX increases, the amount of hydrogen bonds decreases, possibly due to competition for hydrogen bond donors from the lipids.

The general conformation of the CHX molecule as being either compressed or expanded, was measured by tracing the distance between the two chlorine atoms of the chlorophenyl rings located on the ends of the molecule. Initially while the CHX molecule was in water, a broad distribution of Cl-Cl distances was observed varying from 0.2-3.0 nm (Figure 3.9). This corresponds to a wide range of changing conformations from its compressed state to an extended state. After insertion into the membrane the distribution narrows significantly suggesting that there exists a more stable conformation. The distribution of distances is centred around $\sim$ 1.5 nm, which is neither the most compressed state nor the most expanded state of the molecule but rather a "wedge" shape. Figure 3.10 shows an example of this configuration. Note that the chlorine atoms generally point down or in the plane of the bilayer, but almost never point upwards towards the water.

3.4 Discussion

The simulation's Stockholm-lipids parameters (Slipids) are refined based in large part on simulated liquid alkane density, and verified using experimentally determined membrane structural parameters provided by Kucerka et al. [1, 2, 34]. Our simulations of pure DMPC bilayers reproduce the published results without issue. Note that the double-layered distribution of water seen in Figure 3.5 appears in every simulation, and is a consequence of the chosen parametrization of the lipids. Similar simulations in turn form the basis of the experimental analysis of

the small angle scattering (X-ray and neutron combined) of Kucerka et al., where the double-layers can also be seen. There is little comment to be found in these papers on this second, more deeply penetrating layer of water; our data, and similar data from other neutron diffraction experiments do not find such water distributions.

The discrepancy could be a consequence of the fact that Kucerka et al. use dilute, small unilamellar vesicles versus our aligned, slightly dehydrated lamellar membrane stacks with approximately 5 water molecules per lipid. Another possibility is the fact that in Kucerka's model, the water is modelled as the absence of lipid; the molecular volume probability is kept at all points. It is difficult to asses this point, since the data fitting analysis of Kucerka et al. is likely over-parameterized, and no error estimation of the fitted parameters are provided. Indeed, less imposing water distributions can fit the data equally well [35]. Nevertheless, we believe the Slipids parameter set to be state-of-the-art, and the measured structural parameters of Kucerka et al. to be the most self-consistent and reasonable to date.

Whatever the case, even though the experiments do not agree on where the lipid-water interface lies, they both agree qualitatively that that is where the CHX molecule resides. The depth of CHX had little dependence on the concentration of the molecules used, rather it was more dependent on the charge. The neutral CHX were distributed around 0.8 nm from the bilayer center and were observed to spend time at the center at higher concentrations. The charged CHX models were seen further out of the membrane at 1.1 and 1.3 nm respectively and were

not seen at the center of the membrane.

The more CHX added to the DMPC membrane, the thinner it becomes, increasing the area per lipid accordingly. The charge of the CHX determined the degree of deformation of the membrane. The neutral model had a minimal effect to the change in area as well as the thickness and ordered the lipid chains. Both of the charged models had similar but more pronounced deformations to the area and thickness, however it lowered the chain order.

Initial placement of a membrane-active molecule into a simulation presents an interesting challenge. On the one hand, a membrane-protein system can be computationally large, and since simulation times are necessarily relatively short, they may not be long enough for whole body equilibration and rearrangement of the system so that the protein finds its appropriate place in the bilayer. In such cases, experimental information is required to set up the system properly. [36, 37] For smaller molecules like CHX, one can hope for rapid diffusion to overcome this problem, unless there is some unforeseen energy barrier that traps the molecule in a metastable location.

Neither neutrality or charge prevents the molecule from seeking the same most energetically favourable position within the bilayer within a reasonable amount of time. However, an increase in the concentration of CHX increases the amount of intermolecular interactions and thus increases the amount of time needed for the system to reach an equilibrium state. At a concentration of 12:128 CHX:DMPC the molecules had to be started close to the membrane to reduce the amount of time where the molecules interacted with one another in the wa-

ter before finding their way into the membrane. Higher concentrations are not possible under these same time scales for this reason.

Remarkably our results confirm our experiments that a DMPC bilayer can accommodate a significant number of highly charged molecules without significant disruption to the underlying bilayer structure. This has two important consequences. First, +2 charged CHX is not a good candidate for umbrella sampling technique to determine the free energy profile in the bilayer. Any attempt to hold the location of a lone charged CHX deeper in the bilayer than its free energy location will severely distort the bilayer by opening a hole above it that will draw in water. This has been seen before in the case of arginine [38], and was the impetus for our brute-force methods here. Second, our results call into question the biological relevance of DMPC as a membrane mimic in studies of CHX. The remarkable capacity of DMPC to incorporate CHX is much higher than the minimum inhibitory concentration of the drug, which has been observed to be as low as 0.5 µg/ml for certain bacteria [39]. This corresponds to a CHX:lipid ratio of approximately 1:100 compared to our highest concentration of 12:128. We have demonstrated the rapid hydrophilic/phobic interface seeking ability of CHX, however DMPC must be more structurally robust than the components of bacterial, yeast, and viral membranes.

In conclusion, we have conducted a series of molecular dynamics simulations of chlorhexidine in DMPC. The Slipids force field serves as a state-of-the-art parameter set to reproduce many pure lipid bilayer properties very well, and serves as a basis of our simulations. Here we have seen for the first time how

the Slipids DMPC can accommodate a high concentration of solute molecules, even +2 charged, with little change in structural integrity. This is in total agreement with our experience with experimental samples of the same concentration. However, for the case of the molecule chlorhexidine, which quickly seeks the hydrophilic/hydrophobic interface, the Slipids presents a water/lipid interface at a different location than was experimentally measured. This may be a consequence of the sample type, or the parameter set itself, and must be considered further.

Table 3.1: Statistical analysis of the system energy

	Insertion Energy kJ/mol/CHX	12 CHX Drift in Energy kJ/mol/100 ns
Neutral CHX	50-60	627
+1 charge CHX	30-40	378
+2 charge CHX	25-30	182

Table 3.2: Simulated membrane parameters.

		323 K		303 K	
		Area/lipid ($Å^2$)	Thickness (Å)	Area/lipid ($Å^2$)	Thickness (Å)
	Pure DMPC	62.44(2)	28.2(2)	61.16(2)	29.1(2)
Neutral	1:128	63.50(1)	29.0(2)	61.55(1)	30.0(2)
	4:128	64.71(1)	29.2(2)	62.38(1)	29.0(2)
	12:128	66.38(1)	29.6(2)	64.38(1)	28.6(2)
+1 charge	1:128	63.55(1)	27.8(2)	61.07(1)	29.8(2)
	4:128	64.62(1)	28.4(2)	62.48(1)	28.4(2)
	12:128	67.54(1)	28.4(2)	65.37(1)	28.8(2)
+2 charge	1:128	63.34(1)	28.2(2)	61.48(1)	27.8(2)
	4:128	64.52(1)	28.4(2)	62.40(1)	29.0(2)
	12:128	68.00(3)	27.4(2)	66.18(1)	27.2(2)

Table 3.3: Number of hydrogen bonds between CHX biguanide and lipid phosphate oxygen.

		323 K		303 K	
		H-bonds	per CHX	H-bonds	per CHX
Neutral	1:128	1.16	1.16	1.50	1.50
	4:128	2.25	1.39	5.56	1.39
	12:128	3.22	0.96	13.03	1.09
+1 charge	1:128	2.44	2.44	2.44	2.44
	4:128	9.54	2.39	10.87	2.72
	12:128	28.01	2.34	29.00	2.42
+2 charge	1:128	3.19	3.19	3.41	3.41
	4:128	11.58	2.90	15.60	3.90
	12:128	35.81	2.98	41.30	3.44

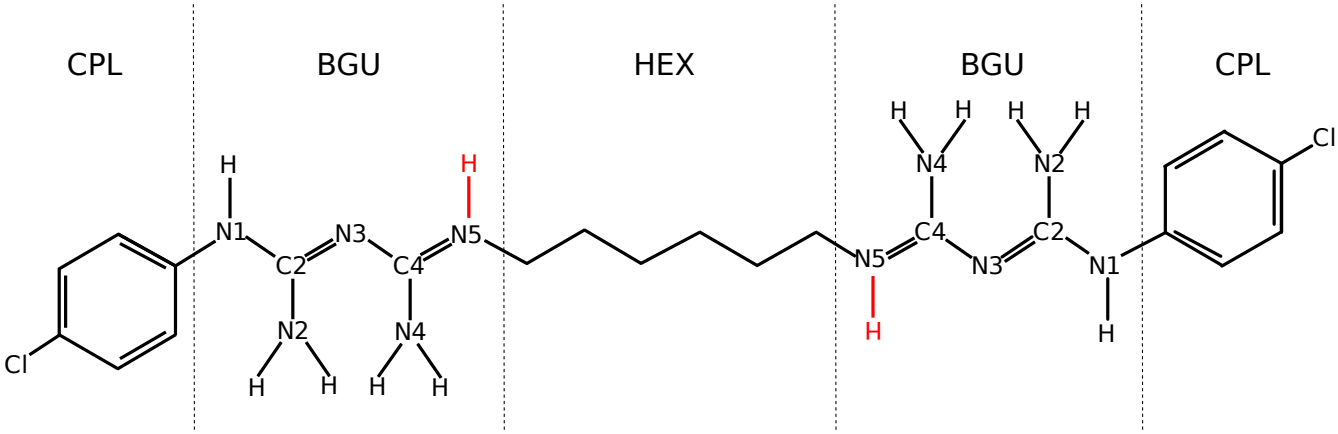

Figure 3.1: Chlorhexidine representation with three groups; chlorophenyl (CPL), biguanide (BGU) and hexane (HEX). Additional hydrogen atoms needed to create a CHX models with +1 and +2 charge are shown on the biguanide N5.

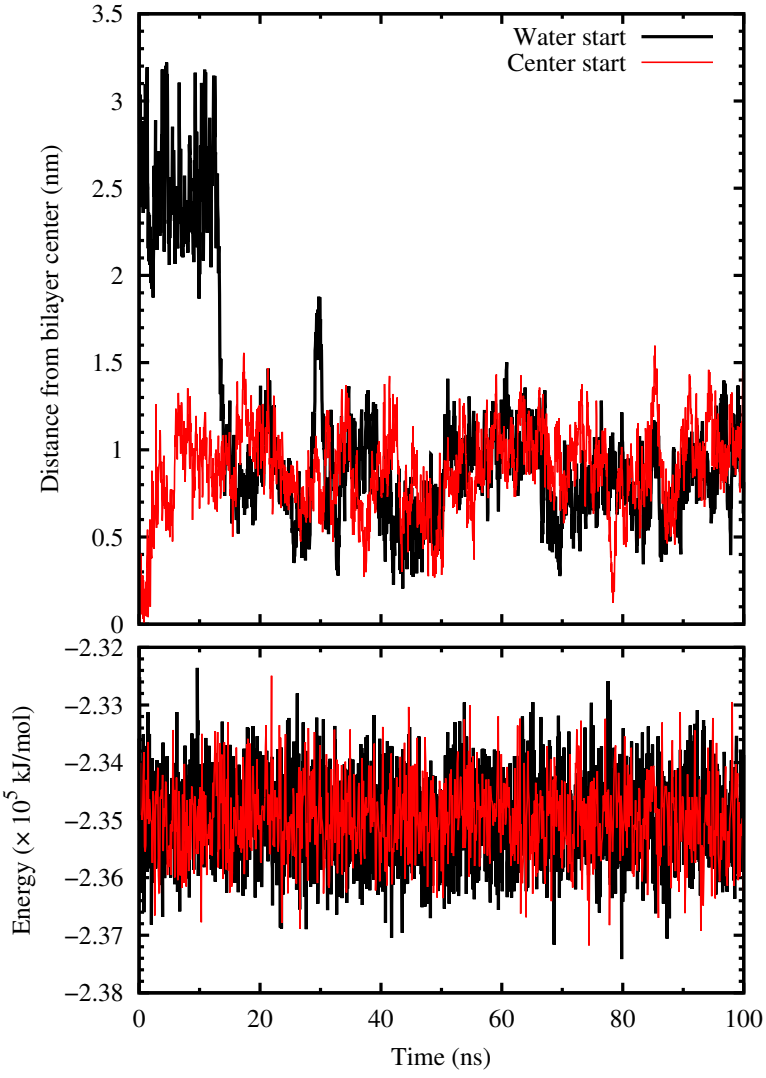

Figure 3.2: Comparison of the distance between the center of mass of HEX and the lipid terminal methyls (upper frame) and the system potential energy (lower frame) for chlorhexidine simulations started from outside the bilayer in the water (black) or the center of the membrane (red). The potential energy is lowered by a small but statistically significant amount as the CHX molecule finds its preferred depth.

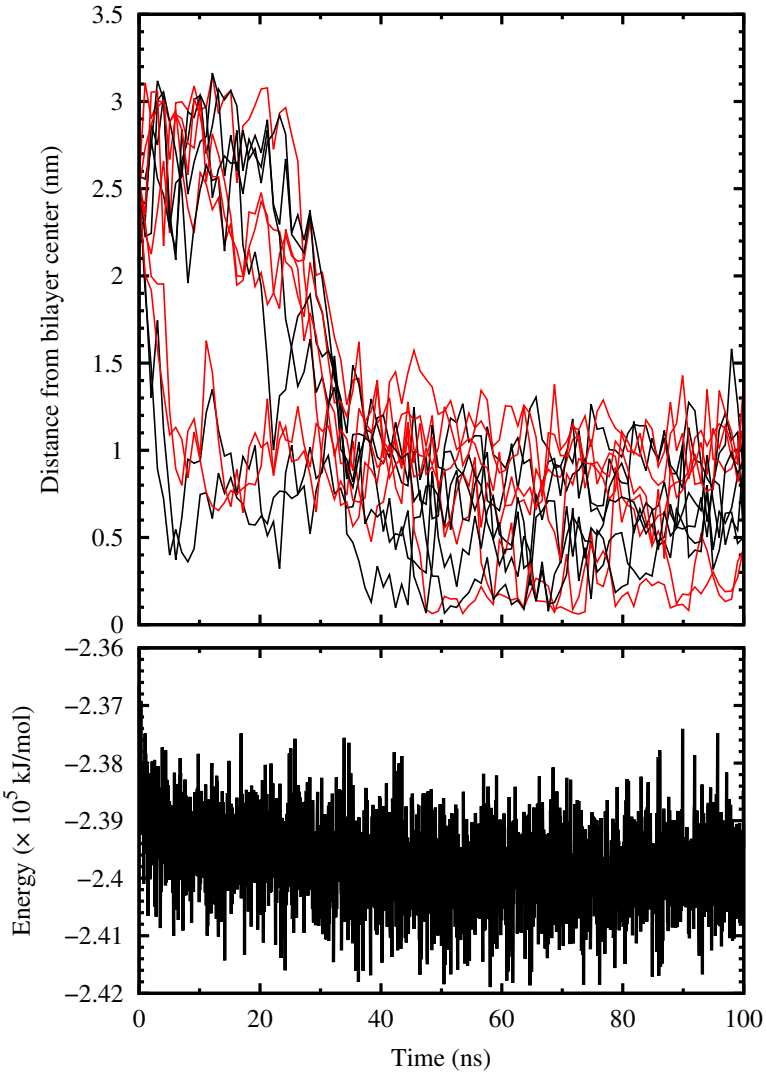

Figure 3.3: (Upper panel) Distance between the center of mass of all twelve neutral CHX HEX and the lipid terminal methyls, showing insertion of each at various times. The traces have been smoothed and some have been colored for clarity. (Lower panel) The system potential energy.

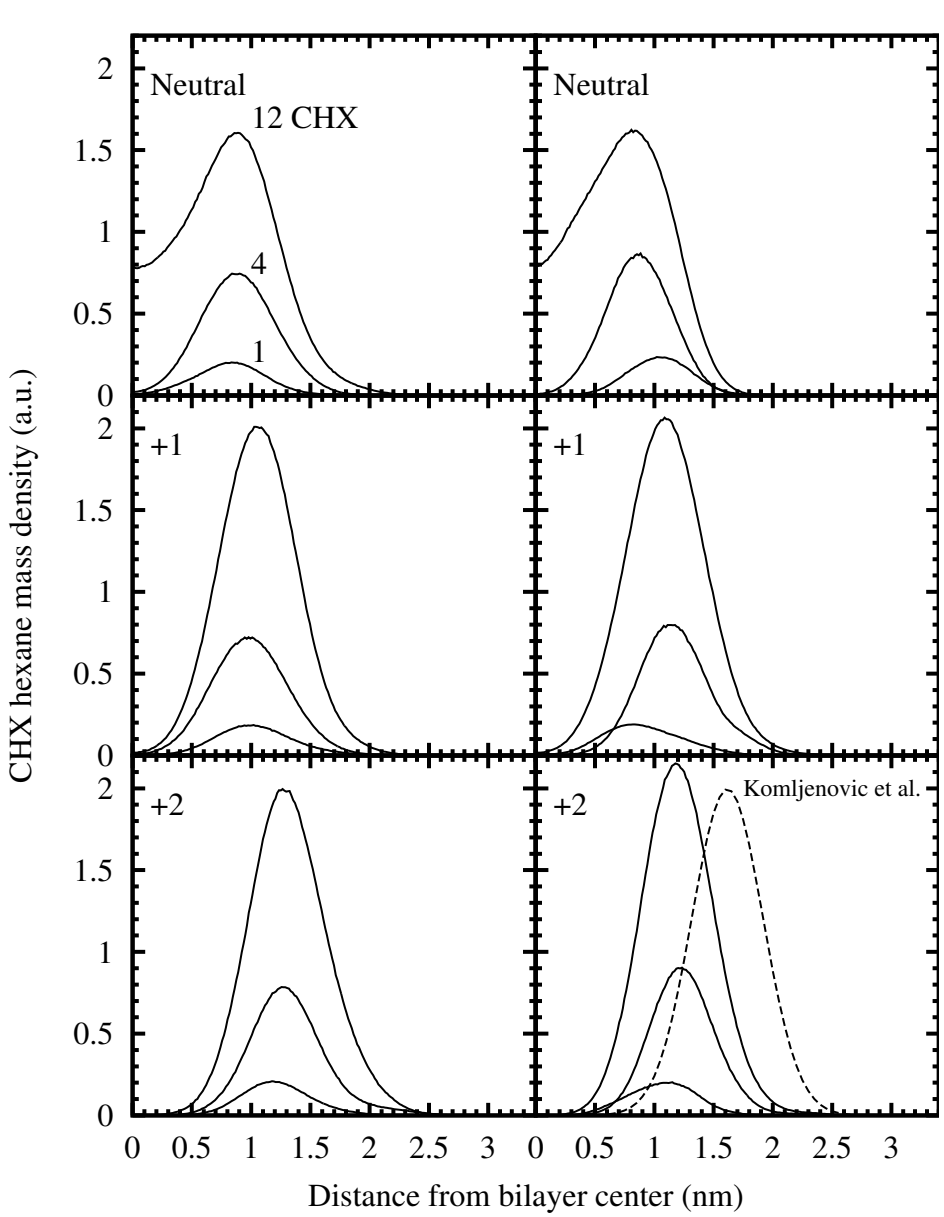

Figure 3.4: HEX distributions for each concentration (1:128, 4:128, 12:128 CHX:DMPC) of neutral (upper frame), +1 charged (center frame) and +2 charged CHX (lower frame) at both 323K and 303K. The HEX distribution determined by neutron scattering is added to the bottom right frame for comparison [20].

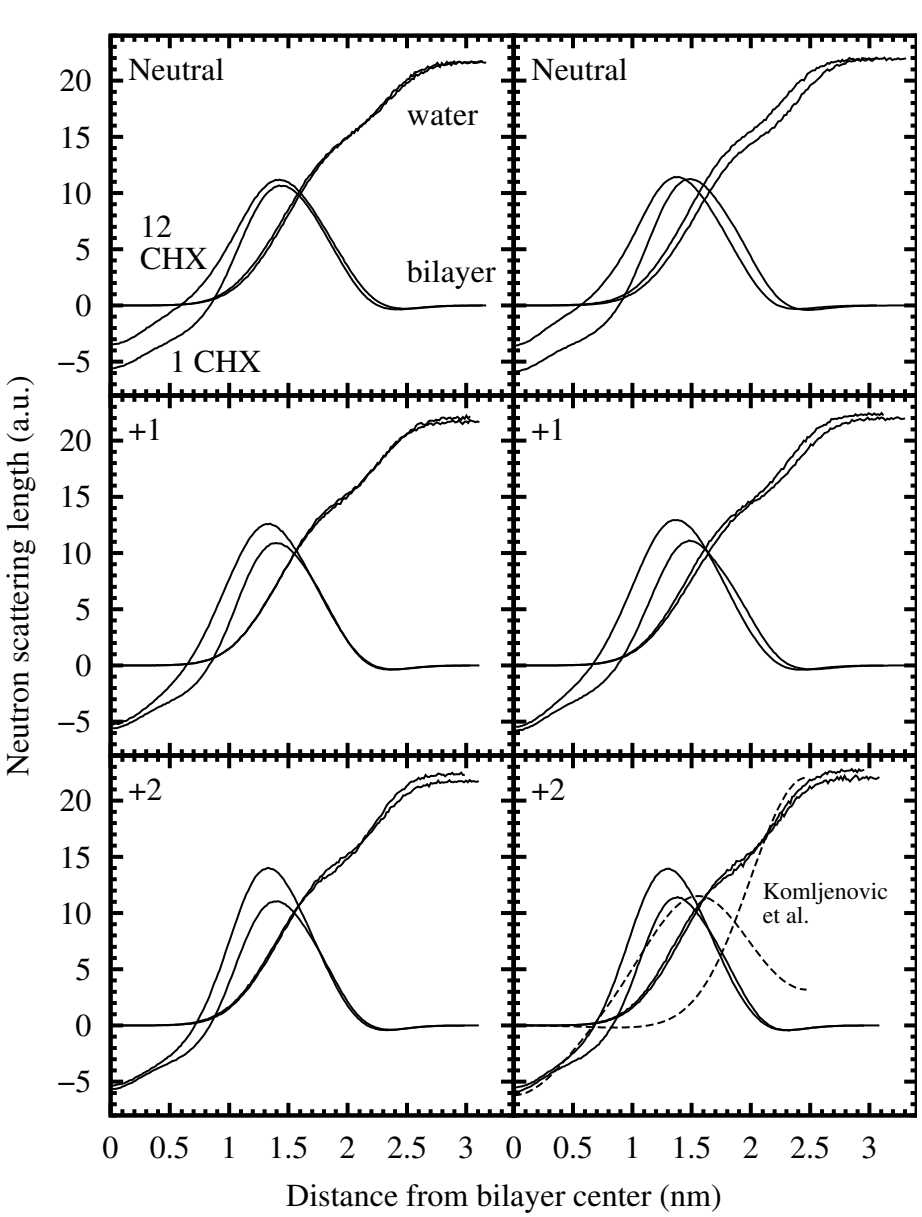

Figure 3.5: Comparison of the neutron scattering length density of CHX:DMPC bilayers or the extra-bilayer water profiles for the 1:128 and 12:128 CHX:DMPC concentrations. The dotted line in the bottom right frame represents the results from neutron scattering from Komljenovic et al., at 1:10 CHX:DMPC [20]

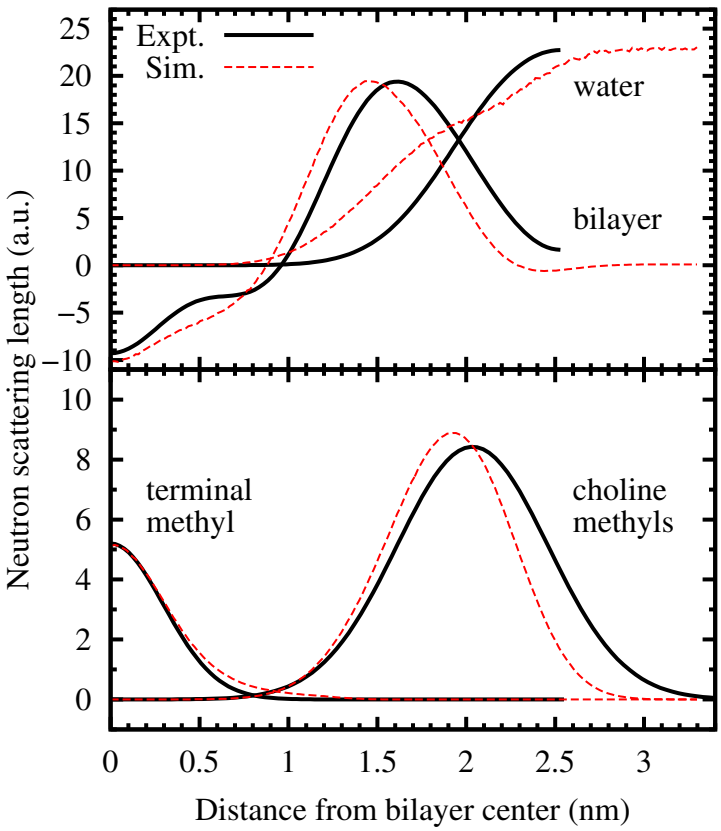

Figure 3.6: Comparison of the experimental (solid) and simulated (dashed) neutron scattering length density of either the bilayer or external water penetration (upper frame) as well as the neutron scattering length density (mass distribution) of the terminal and choline methyl hydrogen (lower frame)

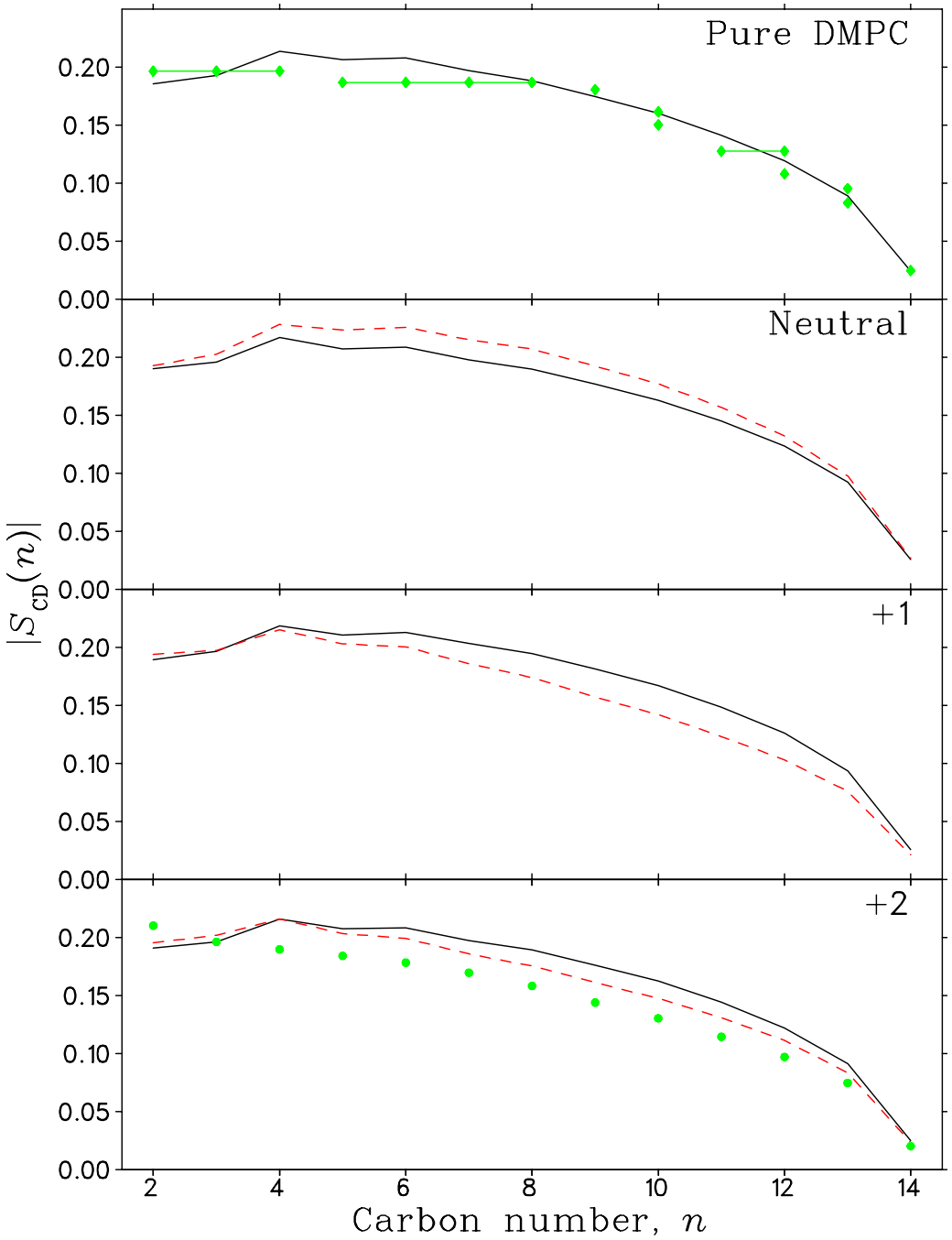

Figure 3.7: DMPC simulated lipid deuterium order parameters of 1:128 (solid) and 12:128 (dashed) CHX:DMPC concentrations at 308 K. Experimental data, also at 308 K, are also shown for pure DMPC (diamonds, upper frame) and at 1:10 CHX:DMPC concentration (circles, lower frame)

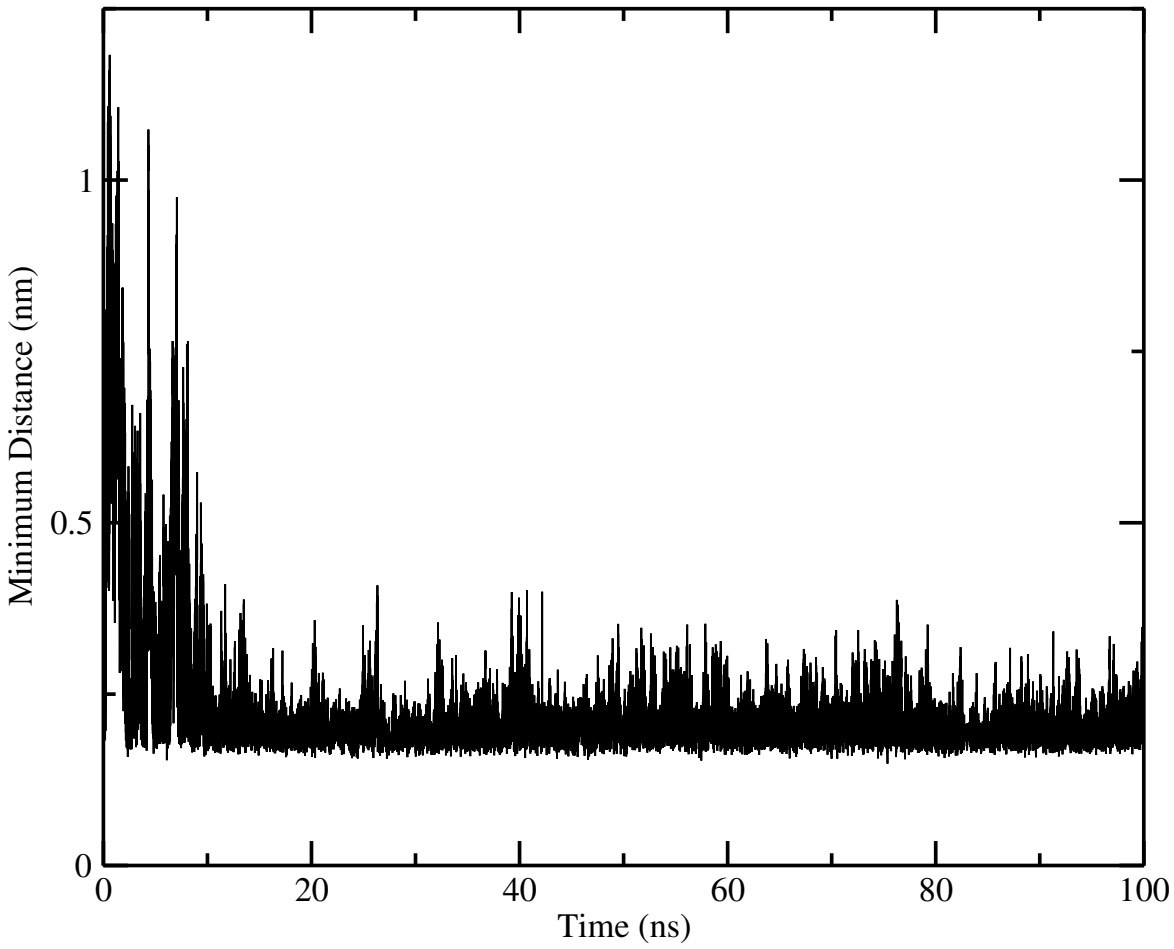

Figure 3.8: Minimum distance between the additional hydrogen of the biguanide (BGU) group and the lipid phosphate oxygen for the +1 charged CHX at 323 K

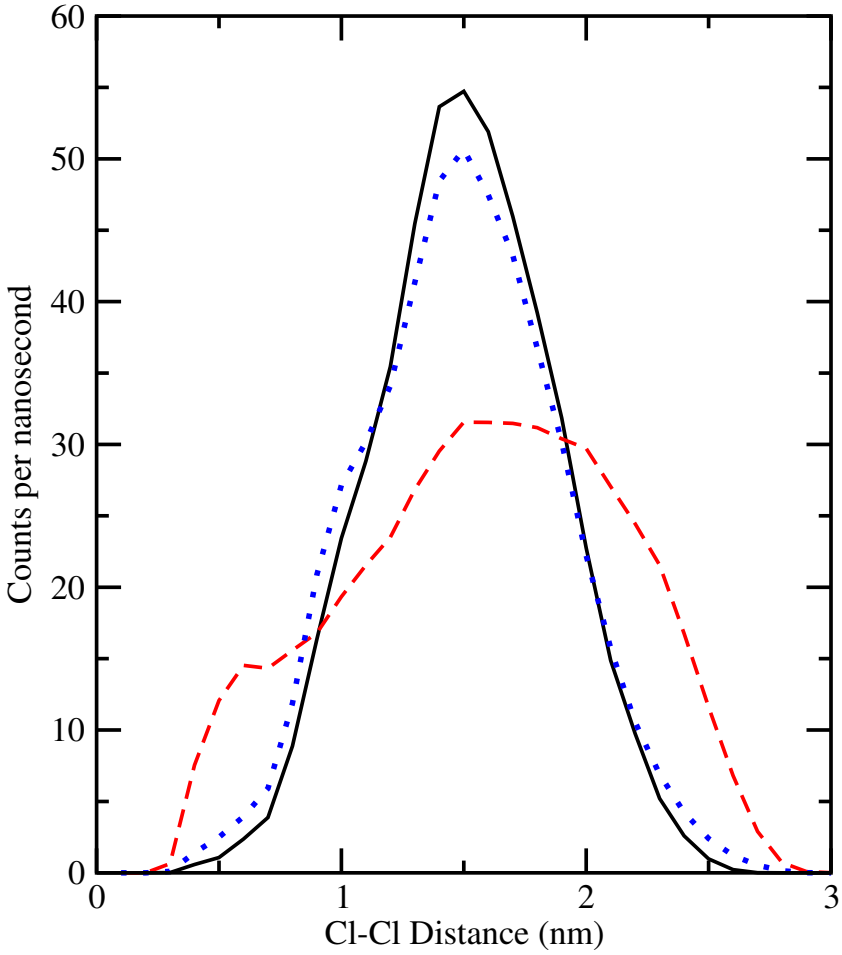

Figure 3.9: Cl-Cl distance histogram of twelve +2 charged CHX during the first 10 ns at 323K before insertion (dashed), for 10 ns after insertion (dotted), and the last 10 ns at 309K (solid)

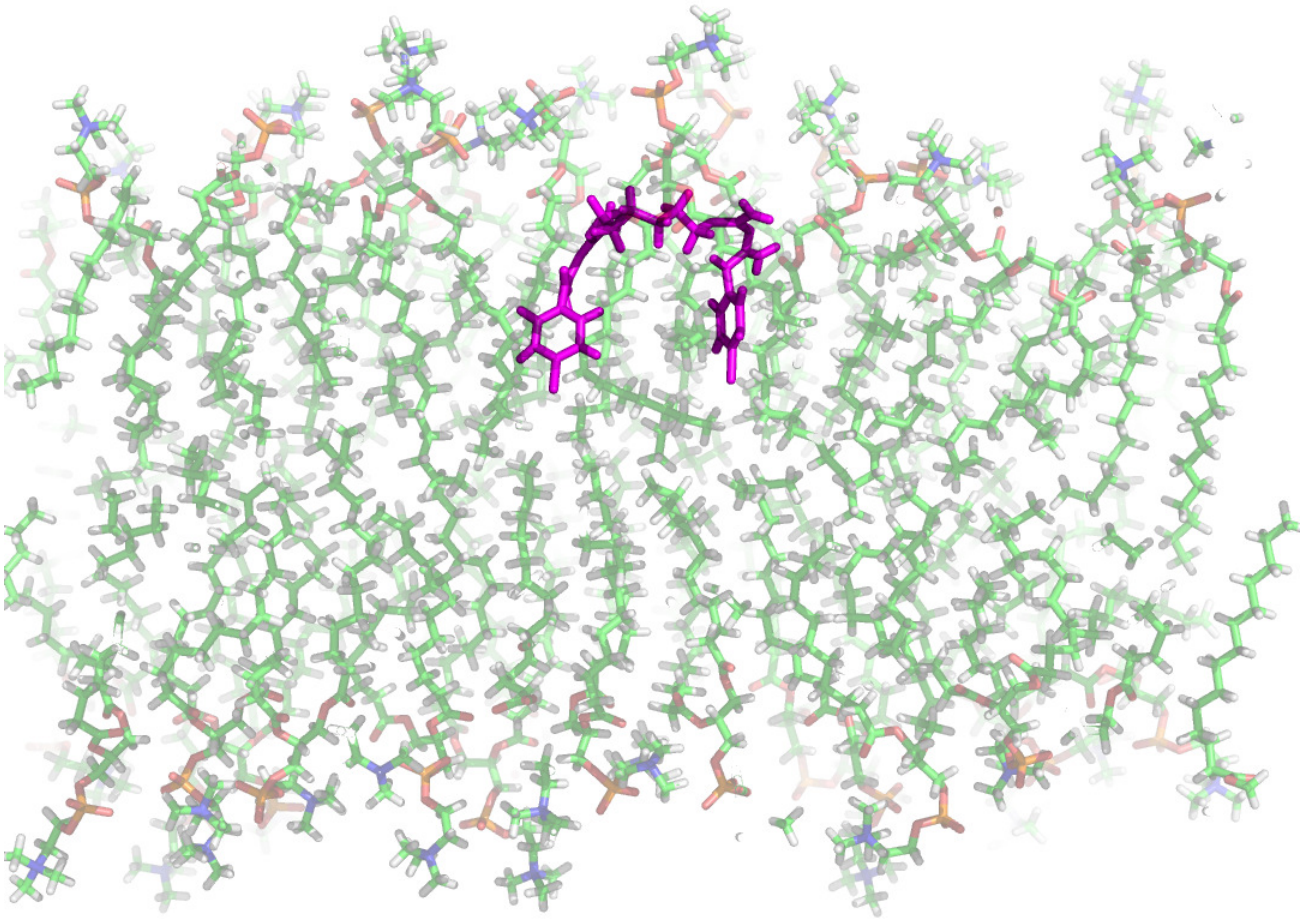

Figure 3.10: Simulation snapshot of the neutral CHX molecule (solid purple) after insertion into DMPC at 323 K

References

1. Jambeck, J. & Lyubartsev, A. Derivation and Systematic Validation of a Refined All-Atom Force Field for Phosphatidylcholine Lipids. *The Journal of Physical Chemistry B* **116,** 3164–3179 (10 2012).

2. Jambeck, J. & Lyubartsev, A. Another Piece of the Membrane Puzzle: Extending Slipids Further. *Journal of Chemical Theory and Computation* **9,** 774–784 (2013).

3. Kucerka, N, Katsaras, J & Nagle, J. Comparing membrane simulations to scattering experiments: introducing the SIMtoEXP software. *The Journal of membrane biology* **235,** 43–50 (2010).

4. Vorobyov, I., Li, L. & Allen, T. W. Assessing Atomistic and Coarse-Grained Force Fields for Protein-Lipid Interactions: the Formidable Challenge of an Ionizable Side Chain in a Membrane. *Journal of Physical Chemistry B* **112,** 9588–9602 (2008).

5. Campbell, R. K., White, J. & Saulie, B. A. Metformin: a new oral biguanide. *Clinical Therapeutics* **18,** 360–371 (1996).

6. Uchiyama, H. *et al.* Quinine-resistant Severe Falciparum Malaria Effectively Treated with Atovaquone and Proguanil Hydrochloride Combination Therapy. *Internal Medicine* **43,** 624–627 (2004).

7. Thomas, L., Russell, A. & Maillard, J.-Y. Antimicrobial activity of chlorhexidine diacetate and benzalkonium chloride against Pseudomonas aeruginosa

and its response to biocide residues. *Journal of Applied Microbiology* **98,** 533–543 (2005).

8. Denys, A, Machlański, T, Bialek, J & Mrozicki, S. Relationships between chemical structure and antiviral activity of some biguanide derivatives. *Zentralblatt Für Bakteriologie, Parasitenkunde, Infektionskrankheiten Und Hygiene. Erste Abteilung Originale. Reihe B: Hygiene, Präventive Medizin* **164,** 85–89 (1977).

9. Tanzer, J. M., Slee, A. M. & Kamay, B. A. Structural requirements of guanide, biguanide, and bisbiguanide agents for antiplaque activity. *Antimicrobial Agents And Chemotherapy* **12,** 721–729 (1977).

10. Greenstein, G., Berman, C. & Jaffin, R. Chlorhexidine. An adjunct to periodontal therapy. *J. Periodontol.* **57,** 370–377 (1986).

11. Blackburn, R. S., Harvey, A., Kettle, L. L., Payne, J. D. & Russell, S. J. Sorption of Poly(hexamethylenebiguanide) on Cellulose: Mechanism of Binding and Molecular Recognition. *Langmuir* **22,** 5636–5644 (2006).

12. Blackburn, R. S. *et al.* Sorption of Chlorhexidine on Cellulose: Mechanism of Binding and Molecular Recognition. *Journal of Physical Chemistry B* **111,** 8775–8784 (2007).

13. Yoo, J. & Cui, Q. Does Arginine Remain Protonated in the Lipid Membrane? Insights from Microscopic pK_a Calculations. *Biophysical Journal: Biophysical Letters* **94,** L61–L63 (2008).

14. Li, L., Vorobyov, I. & Allen, T. W. Potential of Mean Force and pKa Profile Calculation for a Lipid Membrane-Exposed Arginine Side Chain. *Journal of Physical Chemistry B* **112,** 9574–9587 (2008).

15. MacKerel Jr., A. *et al.* in (ed et al., P. v. R. S.) 271–277 (John Wiley & Sons: Chichester, 1998).

16. Brooks, B. *et al.* CHARMM: A Program for Macromolecular Energy, Minimization, and Dynamics Calculations. *Journal of Computational Chemistry* **4,** 187–217 (1983).

17. Brooks, B & et. al. CHARMM: the biomolecular simulation program. *Journal of Computational Chemistry* **30,** 1545–1614 (2009).

18. Van Gunsteren, W. F. *et al. Biomolecular Simulation: The GROMOS96 manual and user guide.* Zürich, Switzerland: Hochschulverlag AG an der ETH Zürich. 1996.

19. Frisch, M. J. *et al. Gaussian 09 Revision B.01* Gaussian Inc. Wallingford CT 2009.

20. Komljenović, I., Marquardt, D., Harroun, T. A. & Sternin, E. Location of chlorhexidine in DMPC model membranes: a neutron diffraction study. *Chemistry and Physics of Lipids* **163,** 480–487 (2010).

21. Adane, L. & Bharatam, P. V. Tautomeric Preferences and Electron Delocalization in Biurets, Thiobiurets, and Dithiobiurets: An *Ab Initio* Study. *International Journal of Quantum Chemistry* **108** (2008).

22. Bharatam, P. V., Patel, D. S. & Iqbal, P. Pharmacophoric Features of Biguanide Derivatives: An Electronic and Structural Analysis. *Journal of Medicinal Chemistry* **48,** 7615–7622 (2005).

23. Maksić, Z. B. & Kovačević, B. Absolute Proton Affinity of Some Polyguanides. *Journal of Organic Chemistry* **65,** 3303–3309 (2000).

24. Guha, R. *et al.* The Blue Obelisk–Interoperability in Chemical Informatics. *Journal of Chemical Information and Modeling* **46,** 991–998 (2006).

25. O'Boyle, N. M. *et al. OpenBable* v2.2.3. 2011.

26. Hanwell, M. D. *et al. Avogadro: an advanced semantic chemical editor, visualization, and analysis platform* v1.0.3. 2012.

27. Valiev, M. *et al.* NWChem: A comprehensive and scalable open-source solution for large scale molecular simulations. *Computer Physics Communications* **181,** 1477–1489 (2010).

28. Jo, S., Kim, T., Iyer, V. & Im, W. CHARMM-GUI: A web-based graphical user interface for CHARMM. *Journal of Computational Chemistry* **29,** 1859–1865 (2008).

29. Kukol, A. Lipid Models for United-Atom Molecular Dynamics Simulations of Proteins. *Journal of Chemical Theory and Computation* **5,** 615–626 (2009).

30. Poger, D. & Mark, A. E. On the Validation of Molecular Dynamics Simulations of Saturated and cis-Monounsaturated Phosphatidylcholine Lipid Bilayers: A Comparison with Experiment. *Journal of Chemical Theory and Computation* **6,** 325–336 (2010).

31. Hess, B., Kutzner, C., van der Spoel, D. & Lindahl, E. GROMACS 4: Algorithms for Highly Efficient, Load-Balanced, and Scalable Molecular Simulation. *Journal of Chemical Theory and Computation* **4,** 435–447 (2008).

32. Schiferl, S. K. & Wallace, D. C. Statistical errors in molecular dynamics averages. *Journal of Chemical Physics* **83,** 5203–5209 (1995).

33. Kučerka, N. *et al.* Lipid Bilayer Structure Determined by the Simultaneous Analysis of Neutron and X-Ray Scattering Data. *Biophysical Journal* **95,** 2356–2367 (2008).

34. Kučerka, N., Nieh, M & Katsaras, J. Fluid phase lipid areas and bilayer thicknesses of commonly used phosphatidylcholines as a function of temperature. *Biochimica et Biophysica Acta* **1808,** 2761–2771 (2011).

35. Kučerka, N., Nagle, J. F., Feller, S. E. & Balgavý, P. Models to analyze small-angle neutron scattering from unilamellar lipid vesicles. *Physical Review E* **051903,** 1–9 (2004).

36. Basyn, F., Spies, B., Bouffioux, O., Thomas, A. & Brasseur, R. Insertion of X-ray structures of proteins in membranes. *Journal of Molecular Graphics and Modelling* **22,** 11–21 (2003).

37. Balali-Mood, K., Harroun, T. A. & Bradshaw, J. P. Membrane-bound ARF1 peptide: interpretation of neutron diffraction data by molecular dynamics simulation methods. *Molecular Membrane Biology* **22,** 379–388 (2005).

38. MacCullum, J., Bennett, D. & Tieleman, P. Transfer of Arginine into Lipid Bilayers is Nonadditive. *Biophysical Journal* **101,** 110–117 (2011).

39. Fraise, A, Maillard, J & Sattar, S. *Russell, Hugo and Ayliffe's Principles and Practice of Disinfection, Preservation and Sterilization [electronic resource].* (Hoboken : Wiley, 2012., 2012).

Chapter 4

A MARTINI extension for Pseudomonas aeruginosa PAO1 lipopolysaccharide

4.1 Introduction

Pseudomonas aeruginosa is a gram-negative bacterium, often found in soil and plants, which is a known opportunistic human pathogen. It targets those who are immunodeficient or otherwise compromised, causing infection [1, 2]. *P. aeruginosa* has been shown to be non-susceptible to all but a select few antibiotics [3]. Antibiotic resistance is a characteristic of many gram negative bacteria, in part due to their unique composition and electrostatics of their cell envelope.

Gram negative bacteria have a cell envelope consisting of an inner membrane, periplasm and an outer membrane. The outer membrane is an asymmetric membrane with a large component of the outer leaflet being lipopolysaccharide (LPS) which can cover about 75 % of the outer surface [4, 5]. The inner leaflet is composed of a mixture of phospholipids, with different headgroup and hydrocarbon

tail chain lengths. Analysis of the outer membrane has determined that the most prominent headgroup is phosphoethanolamine (PE), and the most common tails are 18:1 and 16:0 [6, 7].

LPS as its name suggests, is a molecule with a mixture of both lipid and sugar components. Many different forms of the LPS molecule exist in nature but all with the similar general form. LPS consists of lipid A which is composed of 5-6 fatty acid acyl tails attached to a disaccharide backbone that creates a hydrophobic region anchoring it into the membrane. Attached to the lipid A is the core oligosaccharide which consists of short chain of sugars and has a large amount of negative charge. There is then the O polysaccharide side chain, a chain of repeating sugar chains which vary in length from 1-30 units depending on the bacteria and environment [8]

Molecular dynamics (MD) simulations are currently a very powerful tool from observing the dynamics of biological systems. Many simulations provide detail at an atomic resolution using an all-atom (AA) approach. A number of AA LPS simulations have been reported for LPS, including those for *Escherichia coli* [9, 10], and *P. aeruginosa* [11–13]. The largest of these simulations incorporate 72 LPS in a single bilayer leaflet.

While AA simulations have proven to be very effective, since a detailed and effective simulation of a cell membrane requires hundreds of thousands of atoms, AA simulations are limited to small system sizes and time scales limiting the sampling of conformal space. Coarse grained (CG) simulations have been created to overcome this limitation. The MARTINI force field has made tremendous

progress in providing a useful method for studying the mechanics of biomolecules on both large size and time scales [14]. CG models reduce the internal degrees of freedom of a molecule by averaging out some atomic detail, mapping approximately 4 heavy atoms and their associated hydrogen to 1 pseudo-atom. A key feature is the fair reproduction of structural and thermodynamic data [15, 16]. The result is a system with much fewer atoms, making it considerably more computationally efficient.

The MARTINI force field has a robust collection of phospholipids and sterols for simulation, and has been extended to both carbohydrates [17] and glycolipids [18, 19], and importantly now includes polarizable water [20]. However, to the best of our knowledge, only a single CG force field for LPS has been developed [21], and has been tested exclusively in non-polarized water and uses DPPE (16:0,16:0 PE) as the base layer, which does not incorporate the effects of the abundant unsaturated lipid tails present in *P. aeruginosa* [6, 7]. A model for LPS has been cited as an important missing element of the MARTINI collection [15, 22].

A single *P. aeruginosa* cell is pill shaped, approximately 0.5-1 um wide and 1-5 um tall. If this cell was coated in LPS, this corresponds to approximately 100,000 - 1,000,000 LPS molecules. Current attempts to simulate AA LPS systems have been limited to very small systems due to the large size of the LPS molecule [10, 13]. Therefore to simulate even the smallest of Pseudomonas aeruginosa bacteria cells, an AA approach would be too computationally intensive to simulate on reasonable timescales.

In this report, we construct a MARTINI compatible LPS model from an AA

simulation of the rough LPS from *P. aeruginosa* [13]. This requires construction of new carbohydrates and designing a new AA-to-CG atom mapping. Refining bonds and angles were undertaken to reproduce the calculated dynamics of the AA model. We are able to increase the size of the simulated membrane several fold, while improving computational efficiency. Finally, we compare our results to neutron scattering experiments on the structure of LPS.

4.2 Methods

4.2.1 MARTINI Parameterization

The coarse graining of LPS was done using the bottom up approach, building on AA simulations, meaning that the AA LPS simulations were mapped into virtual particles at the location of the center of mass of the atom collection they represent. The final decision on the mapping is shown in the schematic of Figure 4.1. In many regions, the MARTINI particles are entirely consistent with previous simulations of lipids and saccharides [23]. To provide the highly negative charge of the LPS molecule, eight of the particles were given a -1 charge corresponding to the most electronegative parts of the AA model, and the others were given no charge (see topology at http://www.physics.brocku.ca/MARTINI/ for complete particle assignments).

The bonded parameters for the CG force field are determined from these virtual mapped particles of the AA simulation, and are measured by constructing histograms of the bond length between virtual particles over the entire simula-

tion. The height and peak center of these histograms represent the equilibrium length and spring strength for that bond. The same is done with angles between triplets of virtual atoms in the simulations. Dihedrals however, were omitted as explained in the results section. The construction of the AA membrane simulations used for parameterization are discussed below.

Most often, the choice of virtual particles fortuitously led to a Gaussian-shaped single peak, but this is not always guaranteed. Restrictions among competing bond/angle/dihedral parameters in the underlying AA force field can distort the histogram shape, or add second, smaller peak values. However, the force field between virtual particles used was always harmonic, and cannot reproduce overly complex distributions. However, the non-Gaussian distributions account for a small fraction of the model, and can still be fit with a Gaussian to capture the majority of its conformational distributions. Thus all recorded histograms were fit to single Gaussian curves using the *fityk* program [24]. If the distribution was split into more than a single peak, the most prominent peak was used.

The height and center of these Gaussian curves were then used as the standard in which to match during a simulation utilizing the newly made CG force field. The strength and center of the harmonic bond and angle potentials were iteratively adjusted until their distribution matched that of the virtual particles from the AA simulation. The first set of iterations were performed on a symmetric LPS bilayer, so that any changes in the per-lipid area was reflected on both sides of the membrane equally, and therefore the system was able to stretch or

shrink as required without falling apart.

For the very first iteration, the initial bond equilibrium length was set to the exact centers of the histograms. The bond strengths were split into 3 categories: the first containing very sharp and narrow peaks were given values of 50,000 kJ mol^{-1} nm^{-2}, wide and histograms with multiple peaks were given a low value of 1,000 kJ mol^{-1} nm^{-2}, and wide but determinate peaks were given an intermediate value of 20,000 kJ mol^{-1} nm^{-2}. All angles were given zero strength as to not interfere with the equilibrating of the bond lengths.

The masses of each CG particle were taken to be the sum of the constituent atoms in which it represented. The charges were set to either 0 or -1, as suggested for the MARTINI force field [16]. The particle types were chosen from the default martini particle types to accurately capture the approximate polarity of each particle, although no attempts were made to adjust their non-bonded interaction parameters. The reduced size 'S' particles were used for the ring structures due to the fact most were the smaller 3-1 mapping, compared to the regular 4-1 mapping used by MARTINI.

The CG simulation was then run for 1 ns at a step of 0.002 and histograms of all of the 72 bonds were created and compared to that from the AA simulation. The values for the equilibrium length r_0, for the iteration i, was calculated as

$$r_0^i = r_0^{i-1} + (r_0^{AA} - r_0^{CG})$$

where r_0^{AA} was the center of the distribution of the AA sim and r_0^{CG} was the center of the histogram for the current iteration of the CG force field. The bond strength k, for the iteration i, was calculated as

$k^i = k^{i-1} \left(\frac{A^{AA}}{A^{CG}} \right)$

where A_{AA} and A_{CG} are the amplitudes of the AA and current CG histograms respectively.

Once at least 80% of the bonds were within 0.1 nm of the AA equilibrium length and within 1% of the height difference, the angles were added into the force field, each with an equilibrium angle corresponding to the center of each AA histogram of angles, and with a strength of 100 kJ/mol. Subsequently, *both* angles and bonds were adjusted after each additional iteration using the equations above, modified for angle center and strength.

Once the largest conformational changes of the membrane occurred and the system was more stable, the bilayer was truncated to create a monolayer of LPS which was placed on top of a monolayer layer of CG 16:0-18:1-phosphatidylethanolamine (POPE) from an equilibrated symmetric POPE simulation [16]. Iterations were then continued until the system was again stable, where the timestep was increased to 0.02 ps and run for 10 ns for each iteration. Once 80% of the bonds were again within 0.1 nm of the AA equilibrium length and within 1% height difference each iteration was run for 100 ns. Iterations were continued until 100% of the bonds were within 0.1 nm and 1% hight from the AA simulation histograms and the angles within 1° and 10% height unless restricted by limitations. The limitations were that no bond strength could be more than 50,000 kJ mol^{-1} nm^{-2}, no angle strength over 1000 kJ mol^{-1} nm^{-2} and no equilibrium angle below 0° or higher than 180 °. Angles within ring structures were also removed since the rings are made of 3 particles, meaning fixing the bond lengths also fixes the an-

gles between them. The tolerance for angles was lower than the bonds due to the fact that the AA histograms were not fit as well by a single gaussian due to the fact they had multiple equilibrium angles, creating a wider distribution.

4.2.2 Membrane Construction

A total of four starting membrane configurations were created, an AA LPS/POPE, an AA LPS/LPS, a CG LPS/POPE and a CG LPS/LPS. The AA LPS/POPE simulation consisted of 49 LPS, 120 POPE, 9800 TIP3P water molecules and 196 Ca ions(4 per LPS). The AA LPS/LPS simulation consisted of 98 LPS, 9800 water molecules and 392 Ca ions. The CG LPS/POPE simulation consisted of 1152 LPS, 3184 POPE, 83984 polarized water molecules and 4608 Ca ions. The CG LPS/LPS simulation consisted of 2304 LPS, 80000 polarized water molecules and 9216 Ca ions. Both water models, ions and POPE used the preexisting MARTINI force field parameters.

The starting configuration and topology for all AA LPS simulations were created from an pre-equilibrated LPS/di9:0-PE asymmetric membrane, originally published by Kirschner et al. using their glycam-based force field [13]. This system was simulated for a further 10 ns to confirm the system was well equilibrated. The LPS half of this equilibrated membrane was then extracted from the final frame of the simulation. First, this extracted LPS monolayer was duplicated and rotated 180° to create a symmetric LPS (LPS/LPS) membrane. Secondly, to create an asymmetric AA LPS/POPE membrane, a pre-equilibrated membrane built from CHARMM-GUI membrane builder, containing 300 POPE/POPE

molecules was simulated for an additional 10 ns, again to confirm stable equilibrium [25]. Since the glycam based force field originally published by Kirschner et al. [13] did not contain the parameters for a POPE molecule, the Slipids [26, 27] force field parameters were utilized. The area A of the simulation box of the Kirschner et. al.'s LPS/di9:0PE membrane and that of the pure POPE/POPE simulation were compared to determine the correct number N of POPE molecules needed to match the area per lipid values for the AA LPS/POPE according to:

$$N_{\mathrm{LPS/POPE}} = \left(\frac{A_{\mathrm{LPS/di9:0PE}}}{A_{\mathrm{POPE/POPE}}}\right) \times \left(\frac{2}{N_{\mathrm{POPE/POPE}}}\right)$$

The 300 POPE/POPE configuration was then cut down to size using the software Avogadro [28], removing a layer of POPE and leaving the correct number of lipids as calculated above, matching the LPS/di9:0PE box size. A total of 120 POPE lipids were used for the supporting bottom leaflet.

The starting configuration for a CG LPS monolayer was constructed using the final frame of the 10 ns AA LPS/di9:0-PE simulation. The center of mass of each CG particle was calculated using the center of mass of the atoms which it represents. This monolayer was duplicated and rotated to create the two identical sides of the CG LPS/LPS. To create a much larger system this system was duplicated 16 times and placed in a 4×4 grid. This new system was equilibrated for 250 ns before it was used to create the CG LPS/POPE membrane by removing the LPS monolayer and placing it onto a POPE monolayer using the same methods as the AA simulations.

4.2.3 Simulation Parameters

All simulations were performed using the GROMACS simulation software (version 5.0.4) [29–31]. All CG simulation were performed in an orthorhombic box with periodic boundary conditions. The systems were first equilibrated with a 1 ns NVT ensemble followed by a 1 ns NPT ensemble. The AA LPS/LPS system showed a large deviation in its original energy and and therefore was subjected to another equilibration period of 200 ns. The final equilibrated systems were then used as the starting configurations for the subsequent 750 ns AA and 3000 ns CG production MD simulations. Following the 3000 ns CG simulations, all polarized water molecules were converted to regular MARTINI water molecules and continued further as described in the results section below.

The temperature of the system was maintained at 309 K by independently coupling the lipids and solvent separately to an external temperature bath with a coupling constant of 5.0 ps using a Nose-Hoover thermostat. The pressure was kept at 1 bar in the lateral and normal directions semi-isotropically using the Parrinello-Rahman barostat, using an isothermal compressibility of 4.5×10^{-5} bar^{-1} and a coupling constant of 5 ps. A 20 fs (CG) and 2 fs (AA) time step with a Leap-Frog integrator was used. The Verlet list group scheme was used to for its optimal usage with GPUs for an increased simulation speed-up. The Verlet list scheme keeps a buffered list with exact cut-offs which are updated every 10 steps. Potentials are shifted to zero with an exact cut-off value of 1.2 nm. PME was used for the long-range electrostatics, with an electrostatic screening constant (ϵ_r) of 15 with the use of non polarized water and 2.5 with the use of

polarized water.

4.3 Results

4.3.1 Bonded Parameters

The selection of MARTINI atoms was chosen in order to minimize the amount of bimodal distributions in the bond distances between two connected virtual particles. This is done by avoiding making a virtual particle that contains an internal degree of freedom with more than one favourable conformation. This was not completely avoidable with a 4-1, or even 5-1, mapping, however, through trial and error, all excluded conformations occurred much less often than the primary conformation. An example of a conformation that was removed when mapping from AA to CG is the C-OH tail on the 0GA ring. This chain can have two conformations, rotated about the carbon atom, and the OH can face one of two directions. The CG virtual atom however merges this tail with the ring carbon which does not allow for any internal freedom to have both conformations. This degree of freedom was "frozen" into the CG bead as either one conformation or the other. Since using the average of both would lead to a model that did not represent either, one distribution was chosen at random since either conformation was equally likely.

Figure 4.2 shows each of the bonds associated with the 0GA ring of the LPS molecule. This small section of the molecule contains a good representation of each of the typical agreements between AA and CG. A majority of the bonds

within the entire LPS molecule were similar to the right-most black and green curves, where a single Gaussian distribution fits the data very well. The mid-range blue curve shows a split in the distribution, where 2 internal conformations are clearly seen in the AA case. Here, the second peak was chosen to be modelled in the CG. The left-most red curve represents a common bond between two ring atoms, which are tightly bound. The limiting spring constant of 50,000 kJ mol^{-1} nm^{-2} held the bond-length to the correct value, however provided a slightly looser bond, and thus wider distribution, than observed in the AA simulation. Switching the type of bond from a harmonic spring type to a constraint type, however did not fare any better, by creating a bond which was too stiff. Since neither a harmonic bond nor the constraint algorithm could accurately fit this bond, the harmonic bond was chosen since it showed to be more stable during long simulation runs.

Bond angles were subject to the iterative construction process as well. Figure 4.3 shows the distribution of angles in the 0GA group. The narrow distributions below 80° are the internal angles to the 0GA ring. Since the ring structure is made of three particles creating a triangle, setting bonded parameters for both the bonds and angles is redundant. Therefore, only bond parameters for these particles were used. Two of the distributions show a bimodal distribution in the AA case due to the C-OH tail described above; the smallest angle however can still be well modelled with one CG distribution without loss of generality. However, choosing the bond length distribution above makes the choice of which angle distribution the CG model will adopt. Softer angle constraints for the re-

maining angles reproduce very well the broad distributions of angles the sugar moieties can adopt.

Dihedrals are not included in standard lipid MARTINI force-fields; there are simply no rotatable groups of consequence [23]. Likewise, only a few are optionally included in the carbohydrate force field, as few groups showed a preferred orientations, ring conformations (chair, boat, etc.) are completely neglected, and different anomers have the same topology [17]. One or two proper dihedrals were included in the extension of CG lipid models to glycolipids, in order to control the relative orientation of the disaccharide with respect to the lipid. However, one major drawback is the requirement of a shorter timestep by half to prevent instabilities arising from tension in the glycosidic links [19]. With this in mind, early during the creation of the LPS force field, an attempt was made to add dihedrals between each of the sugar residues of the molecule, despite the increase in complexity in attempting to hold a branched chain of sugars at a "correct" orientation. It was discovered that the resulting instability led to using an unacceptably small time step of 1 fs, down from the planned 20 fs.

A decision was thus made to forgo all dihedrals. The consequences of this are illustrated in Figure 4.4, which shows several key dihedral distributions both with and without explicit terms. In only one instance does this decision negatively deviate from the AA case. In Figure 4.4A, we see the narrow distribution of the torsion between LKO and 0KO, which could be well matched in the CG by including a proper dihedral. Without the explicit dihedral, it no longer adopts a preferred orientation. In all other cases, however, either there was no preferred

orientation (e.g. WLL→6GA, Figure 4.4C), or steric interactions held dihedrals to the correct preferred orientations (e.g. WLL→6GA, Figure 4.4D). In one case, (e.g. 3H1→WLL, Figure 4.4B), steric interactions were 180° from the AA orientation. In view of these results, we felt that relying on steric interactions for the principal structure organizing mechanism was the better trade-off for keeping stability and computational efficiency.

4.3.2 Structural Features

Both AA and CG simulations display the essential structure of the bilayer, and are in very good agreement with each other. Figure 4.9 shows a snapshot of the CG simulations, the lipids and water separated for clarity. The bilayer structural profile is shown in Figures 4.5 and 4.6, for the LPS/LPS and LPS/POPE simulations respectively. In these figures, we plot the normalized number density of the major components; lipid-A, core oligosaccharide, POPE, water and Ca^{2+} ions, and with the CG beads weighted to the number of atoms they represent. We use the normalized number density, rather than electron density, for future comparison with scattering density profile analysis, which "involves the parsing of the lipid molecule into components whose volume probability distributions follow simple analytical functional forms" [32].

For the symmetric LPS/LPS bilayer, Figure 4.5, the lipid-A moiety extends ± 1.5 nm from the bilayer center, whereas the core oligosaccharide extends outwards from ~ 1.2 nm to ~ 4.2 nm, with a plateau in number density clearly visible in the AA simulation. The oligosaccharide domain contains a fixed density of

waters penetrating from outside, and the majority of Ca^{2+} ions are concentrated deep within the core. The CG model of LPS does an excellent job in reproducing the density plots of the AA model, capturing most of the structural features. Although there is a general loss of detail, the location of each of the distributions of each of the components are in agreement.

The membrane bilayer center was set to be the center of the lipid-A distribution, however the CG distribution of lipid-A is somewhat wider than that of the AA. The center of the core oligosaccharide distribution also differs slightly, with the CG distribution being 0.1 nm closer to the center of the membrane. The CG core oligosaccharide is slightly thinner than the AA model, leading to an overall thinner membrane, cf. Table 4.1. The distribution of calcium ions are in complete agreement in both simulations, likely because the core oligosaccharide in this region is the same for both simulations.

Small differences between the CG and AA number density distributions can be attributed to the larger CG simulation size. The larger CG simulations allow for undulations in the membrane as seen in Figure 4.9, not present in the smaller AA simulation. Undulations in the membrane widen the distributions, and shows water at the center of the membrane even though Figure 4.9, demonstrates an apparent water boundary.

The greatest difference between the AA and CG simulations are the water profiles associated with the LPS. Since the CG membrane is thinner, the water begins to enter the membrane closer to the center, and penetrates all the way through the membrane. A plateau in the water profile near the center of the

LPS is seen in both AA and CG simulations. The AA plateau, however, is much more pronounced than the CG presumably due to the nature of 4-1 molecular mapping of the water in the CG model.

The plateau of water appears near the distribution of Ca ions. It is therefore able to provide a hydration shell for the ions as seen in previous atomistic simulations and experimental evidence [12, 13, 33, 34]. Figure 4.8 shows the radial distribution of water surrounding the Ca ions. It should be noted that in the MARTINI force field, the ions have the first hydration shell built into their parametrization, therefore the first peak corresponding to the first hydration shell is missing from the CG radial distribution. The second and third hydration shell however are present and in general agreement between the AA and CG simulations.

For the LPS/POPE membrane simulations, the center of the membrane was chosen to be the point of equal atom number density between LPS and POPE, as seen in Figure 4.6. Again, we see the water penetration of the core oligosaccharide and lipid-A, and the concentration of Ca^{2+} ions at the core-lipid-A boundary. In contrast to the LPS/LPS simulation, the LPS/POPE AA simulation shows that the water does not penetrate through the POPE side. The POPE layer created a water barrier in the AA simulations, about 0.7 nm wide. The CG LPS/POPE simulation seems to have water penetrating through the center of the membrane and ~ 0.4 nm into the POPE half, with a minimum water concentration of about 1.5 % by atom number. However, as seen in Figure 4.9, little to no water is visible on the bilayer region, however, projecting the vertical undulations of the

large simulation onto the simulation box normal may give rise to artifacts in the distribution of water.

An estimate to the size of the undulations will give insight to the distribution of water. The distribution of the terminal methyl groups of the AA model, or the terminal virtual particle of the CG model, around the average bilayer midplane arises from a convolution of acyl chain flexibility and bilayer undulations. The small AA simulation size restricts the membrane's undulations, and therefore any increase in distribution width of the CG model will likely be due to undulations now possible due to the more expansive system size. Figure 4.7 demonstrates the wider distribution of terminal methyls for the CG simulation in comparison to the AA simulations. Fitting to a Gaussian, the standard deviation increases from 0.187 nm in the AA to 0.371 nm in the CG LPS/POPE. Using the AA value as the estimate of the chain conformation contribution to the CG distribution, we can deconvolve the contribution due to the undulations where we find the amplitude to be 0.236 nm. This may account for some of the observed water penetration into the POPE half mentioned above.

The water at the center of the LPS/LPS bilayer occur in individual channels, as seen in Figure 4.9. With the lipid removed, water pores of various sizes can be seen to occur in the simulation and are stable for the duration. This is not what has been expected from experimental data; although neutron scattering data indicates that there is likely some amount of water in the bilayer center, the picture from experiment was not one of channels or pores [33, 34]. Indeed, no simulation to date matches the measured neutron scattering length density (NSLD) profiles

reported so far. For comparison Figure 4.7 also shows the distribution of the terminal methyl groups for the LPS/LPS case. Again we see that the CG distribution is wider than the AA with values of 0.267 nm and 0.230 nm respectively. Deconvolving contribution to the chain conformation from the total gives an undulation amplitude of 0.138 nm. These smaller undulations are plainly visible in Figure 4.9.

In Figure 4.10, we compare our computed neutron scattering length density profiles with that of Abraham et al. [34] and Kucerka et al. [33]. In these reports, the LPS was isolated from *P. aeruginosa* PAO1, however it contained a mixture of rough and smooth forms, with some O-antigen polysaccharide not present to our simulation. Nevertheless, it has been reported that Ca^{+2} causes a collapse of the carbohydrate chains [35], meaning we would not expect a wildly different bilayer thickness. Further, the nature of the experimental sample means that only LPS/LPS bilayers could be measured, and at a less than total hydration of 84% relative humidity. However the reported thickness of the bilayer was in agreement with fully hydrated bilayers [36].

In the top panel of Figure 4.10, we calculate a theoretical NSLD under the same experimental conditions of fully deuterated water, ^2H_2O, and scaled our calculated profile by a constant to approximate the reported data. If we consider the initial decrease in water concentration as indicating the thickness extent of the LPS, then the experimental data indicate a membrane at least 1 nm thicker than simulation. However, the plateau of water penetration into the core oligosachhraide is not visible in the neutron data; neither is the expected

dip of the CH_3-rich hydrophobic chain as pronounced as seen in the simulated data. When using 8% ^2H_2O, water is effectively invisible to neutrons, and the lower panel of Figure 4.10 shows the NLSD dominated by scattering of the lipid only. While the overall thickness of the bilayer seems correct after accounting for the additional O-antigen polysaccharide in the experimental sample, we are confronted again by the lack of expected dip in the NLSD of the C^1H_3-rich hydrophobic chain at the bilayer center.

There maybe two possible explanations for these discrepancies. First, the inherent low-resolution scattering data, combined with higher acyl chain disorder than what is found in the simulation, will smooth over much of the missing decrease in NSLD at the bilayer center. Second, the O-antigen polysaccharide collapse and low hydration levels may prevent as much water penetration into the core oligosaccharide as is seen in the simulation. These discrepancies need further examination.

Equilibrium times for the CG simulations were shown to take longer than expected, typically on the order of 1-2 μs. This was seen to be caused by the slow diffusion of water and ions into the membrane. Kirschner et al. also noted a long equilibration time ranging on the order of about 500 ns for the AA simulations [13]. A direct comparison, however, can not be made with the AA simulation due to the fact the CG simulation was so much larger, and is therefore expected to take even longer to equilibrate. However, due to the speed increase of CG simulations, they are still computationally less intensive overall.

It is somewhat debatable whether all the simulations reached a final equilib-

rium in the simulated 750 ns for the AA, and 3000 ns for the CG simulations. To illustrate this, the evolution of the average lipid area is shown in Figure 4.11 for the AA simulation, and Figure 4.12 for the CG simulation. The area per lipid of the LPS/LPS systems appear to be reaching an equilibrium value increasing only marginally throughout the final microsecond of the simulation with polarized water and decreasing marginally with the non polarized water. This is directly correlated to the amount of water measured in the center of the membrane. The slow diffusion of water into/out of the membrane is the limiting factor to speed at which the system reaches equilibrium. The starting configuration of the system is therefore of vital importance for setting up the symmetric LPS/LPS membrane. In the final microsecond of each of the LPS/LPS systems the change in the number of water molecules in/out of the center of the membrane is reduced to below a 2% change, reaching its equilibrium number. The LPS/POPE system however, is robust in that it does not contain water pores and therefore the system equilibrated much faster with a steadier value for the area per lipid.

In both LPS/LPS, and LPS/POPE simulations, the average lipid area for the CG is 20% larger than the AA. There is no experimental reference point to the area per lipid of LPS, however the area per lipid of symmetric POPE/POPE vesicles was recently measured to be 0.58 nm^2 at 35 °C, and increases to 0.61 nm^2 at 55 °C [32], which can be used as a basis comparison for our LPS/POPE system. The POPE/POPE membrane used to build the base of our asymmetric membranes had an area per lipid of 0.634 nm^2 when using the MARTINI polarized

water model, which is much larger than the experimental value of 0.580 nm^2 [32]. However, when the polarized water was replaced by the non polarized model, the membrane compressed to a value of 0.594 nm^2, much closer to the experimental value. This prompted us to then also simulate our two CG LPS systems with the nonpolarized water. The results are shown in Figure 4.12 which shows that the area per lipid of LPS/LPS decreasing from 1.719 nm^2 to 1.613 nm^2. The nonpolarized water more accurately reproduced the AA area per lipid of LPS with a value 14% above the AA results in comparison to the 20% overshot value observed with polarized water.

An inherent problem with the use of the current MARTINI nonpolarized water model is that it has been observed to freeze at temperatures above 0 °C, especially in the presence of a nucleation site such as an ordered membrane [16, 20, 23]. This adverse effect was witnessed in our LPS/POPE simulations. To counter this effect we first replaced 10% of the water molecules with the antifreeze particles, however the freezing still persisted. The area per lipid during the first 1000 ns this simulation showed a decrease similar to that of the LPS/LPS stimulation dropping from 1.817 nm^2 to 1.629 nm^2. Raising the temperature was seen to be the only solution to thaw the ice problem, however the water needed to be above 50 °C in addition to having the antifreeze particles. We determined that these fixes altered our system too much to be compared to previous results and was not a consequence of our parameterization since it did not occur in our LPS/LPS system, therefore, we did not push this aspect of study any further.

The large area for the CG LPS is due to two factors that are difficult to sepa-

rate. First, in order to be completely compliant with the MARTINI force field, we made no attempt to adjust the non-bonded interaction parameters of the standard MARTINI atom types. Second, a single CG water bead is actually 4 water molecules in one, which has implications in the volume of space occupied by water penetrating through the bilayer. We believe though, that these limitations of CG are offset by the success of reproducing the bonded parameters, which is reflected in the overall reproducibility of the bilayer structure.

In both of the LPS/LPS simulations, we see a $0.7 \sim 1\%$ increase in lipid area over the duration of the run, with signs of the AA simulation becoming more stable in the first third of the simulation, and in the last 20% of the CG simulation. In both cases, we see the LPS/POPE simulations decreasing in their average lipid areas, more so for the AA with a 2% decrease, but perhaps reaching a plateau in the last 20% of the simulation. We believe that we may have one or two few POPE in the AA case. In the CG LPS/POPE, there are signs of reaching equilibration midway through the simulation. Table 4.1 reports the final area per lipid from the last 100 ns of the AA and last 250 ns of CG simulations.

Finally, the lipid diffusion rates were computed from each simulation, and are reported in Table 4.1. In the LPS/POPE simulations we observe a tenfold larger diffusion rate of POPE in the CG in comparison to in AA, as expected from the MARTINI lipids due to the smoother configurational space. [16, 23] The diffusion rate of the LPS molecules are negligibly small in comparison to the POPE, being on the order of 10^3 times smaller, due to their much larger size.

4.4 Conclusion

The primary motivation for this study is to incorporate models of membrane active and gram-negative targeting antibiotics at relatively high concentrations, extending the size and scope of systems reasonably achievable by AA simulations. Consider for example, chlorhexidine, an effective agent that attacks the membranes of bacteria, yeast, and enveloped viruses [37, 38]. First, chlorhexidine can pass through the outer membrane of gram-negative bacteria before compromising the inner membrane and eliciting a cell-destroying response. We wish to see why chlorhexidine seems to have a different interaction with LPS containing membranes than to bilayers of standard phospholipids. Second, we have seen experimentally that standard phospholipids can accommodate very large concentrations of the drug without disruption. Since we also want to study the effect of concentration on the membrane structure, adding that many chlorhexidine molecules greatly increases the scale of computations to many hundreds of lipids and many dozens of chlorhexidine.

Additional uses of the model proposed in this study are vast, and expanding as the MARTINI force field continues to grow its library of available molecules. Already, it contains a large number of different lipids which, in combination with LPS, can build a realistic outer membrane of a bacterial cell or with the advancements in computational power, even a full bacterial cell. With a simulated outer membrane the mechanics of a bacterial cell can be better studied as well as the mechanism and interaction of different proteins, as well as small molecules. The greatest usage could be in the study of antibacterial drugs, learning their

interaction with the membrane of bacteria, enhancements to previous drugs as well as studying new ones can become more accessible.

Our MARTINI-based CG model has approximately 24× the number of LPS per leaflet than the AA simulation, yet it has 8× fewer atoms and uses a 10× larger timestep, which corresponds to an theoretical 80× speed increase. On equivalent computational systems our AA simulation was capable or running at an average 654 ns day^{-1} LPS^{-1}, while the CG was averaging 60,385 ns day^{-1} LPS^{-1}, an actual 92× speed increase. Thus MARTINI force field is capable of massive scale simulations of LPS membranes suitable for additional work. A gromacs compatible .itp topology file can be found in the supplementary data for easy access and usage.

We have identified 3 main limitations of our model. First, our CG LPS model was tested in both, polarized and non-polarized water environments with mixed results. The model more closely mimics the area per lipid and thickness of the AA simulations in the presence of nonpolarized water, however due to the limitations of the current CG water models, care must be taken to ensure that the water does not freeze. Second, the starting configuration of LPS is of vital importance to the stability and equilibration time of the system. We noted that the LPS/LPS system is highly susceptible to water in the center of the membrane. The water creates channels through the membrane which take a very long time to equilibrate as the water is slow to enter and leave these pores. An asymmetric LPS/phospholipid membrane however, does not have this problem for the phospholipid monolayer provides an adequate water barrier so that pores can

not form.

Finally, not as a limitation to the model but more of a limitation of this study, we have not explored the effects of changing the base layer of phospholipids. Since the LPS molecule is so large, an increase or decrease in the number of phospholipids on the base layer of the LPS/POPE would unlikely cause an LPS to change sides of the bilayer but rather cause curvature in the membrane. This could affect most of the bilayer properties studied in this paper. Further, the study of how different phospholipids or mixtures of phospholipids as the base layer affect the behaviours of LPS is still unknown. In this study we matched the number of POPE molecules to match the area of the LPS monolayer, however studying the change in the lateral pressure of the membrane as well as induced curvature due to an surplus or absence of POPE or due to replacing some POPE with different phospholipids would be an important extension to this study.

4.5 Acknowledgements

This work was supported by the Natural Sciences and Engineering Research Council of Canada, the Shared Hierarchical Academic Research Computing Network (SHARCNET: www.sharcnet.ca), and Compute/Calcul Canada.

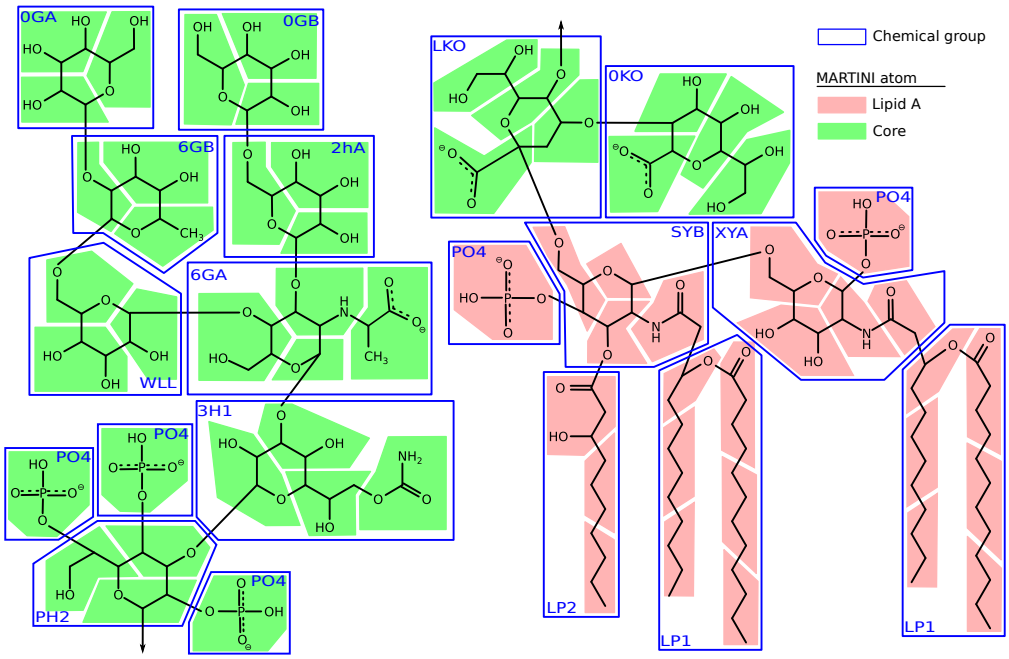

Figure 4.1: Schematic of the lipopolysaccharide of *P. aeruginosa* used for simulation. Residues and groups are drawn in boxes, with the naming convention used by Kirschner et al. [13]. Shaded areas indicate coarse grain atom groupings.

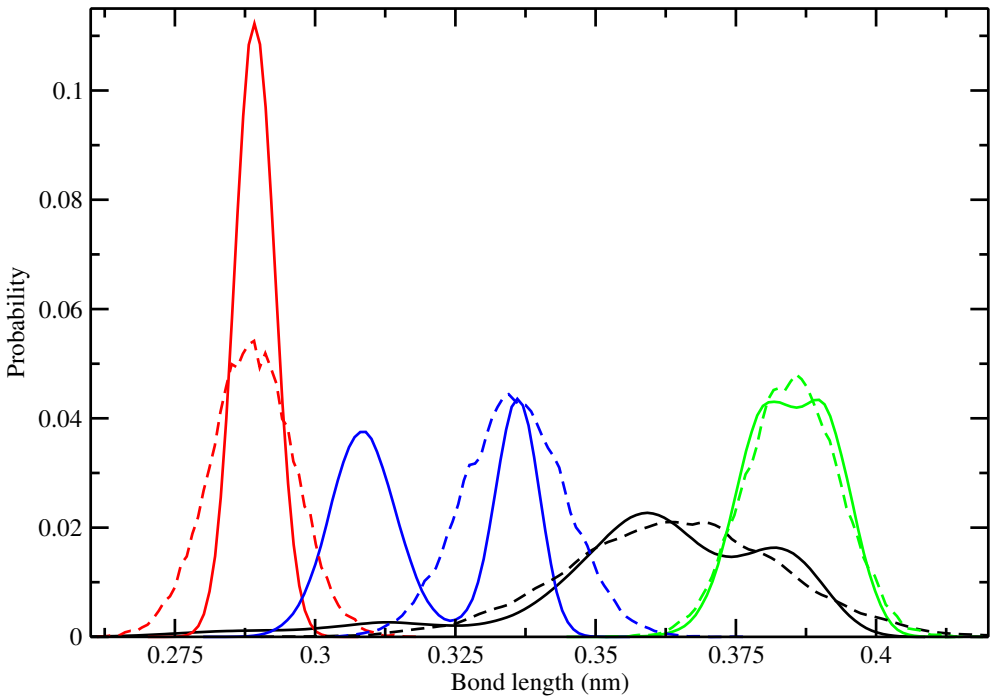

Figure 4.2: Distribution of bond lengths for all of the coarse-grained bonds of inside and connecting to the group 0GA, coloured to emphasise the four different bonds. (Colour online.) Both the AA (solid lines, based on virtual particles) and CG (dotted lines) are shown for a 10 ns period.

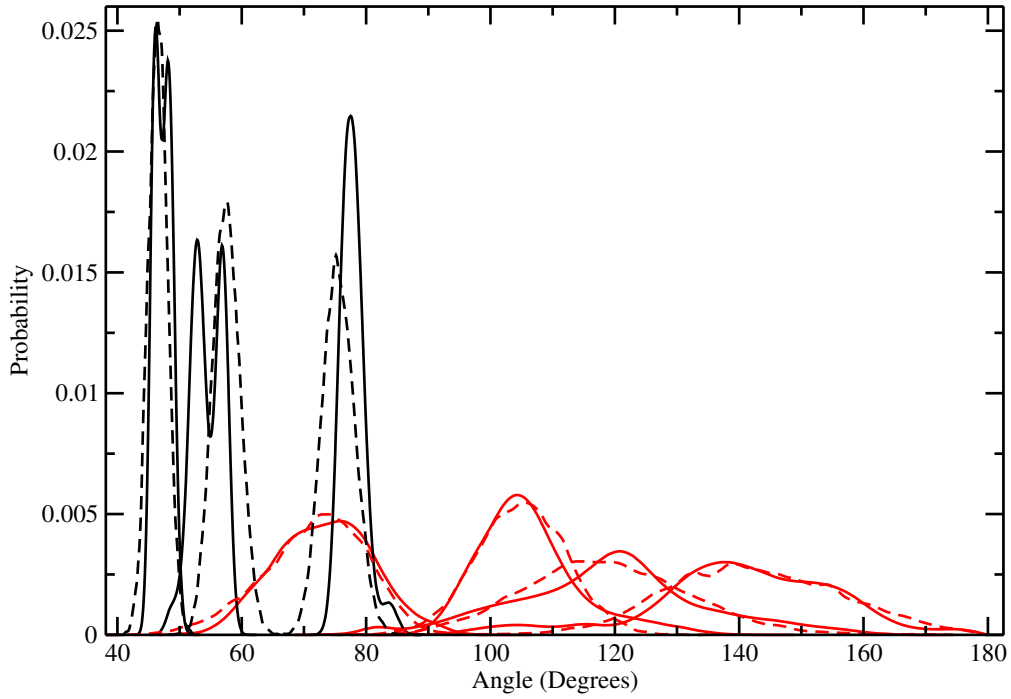

Figure 4.3: Distribution of bond angles for all of the coarse-grained angles of group 0GA. (Color online.) Both the AA (solid lines, based on virtual particles) and CG (dotted lines)are shown for a 10 ns period. The black lines all $< 80^\circ$ represent the three internal ring angles, while the red lines $> 70^\circ$ represent external angles, including the bond between 0GA and 6GB.

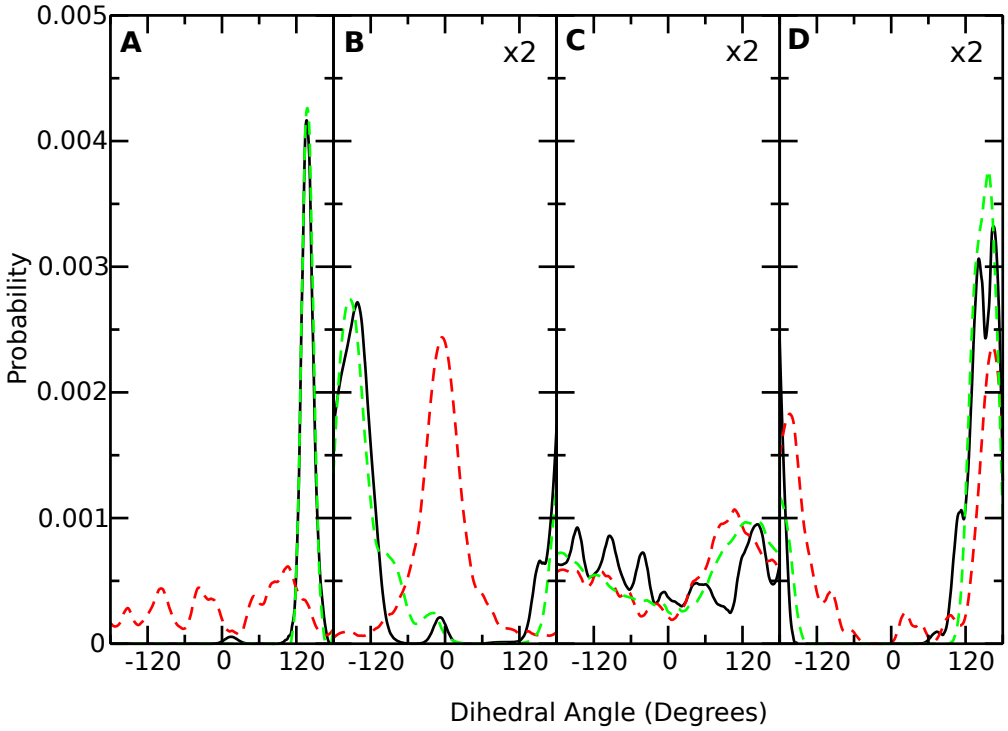

Figure 4.4: (Color online) Example dihedral distributions of AA (solid lines), CG with explicit dihedral terms (dotted green), and CG with no explicit dihedral terms (dotted red). Torsions shown represent those for the bonds connecting the groups: A) LKO→ 0KO, B) 3H1→WLL, C) WLL→6GA, and D) 2hA→0GB.

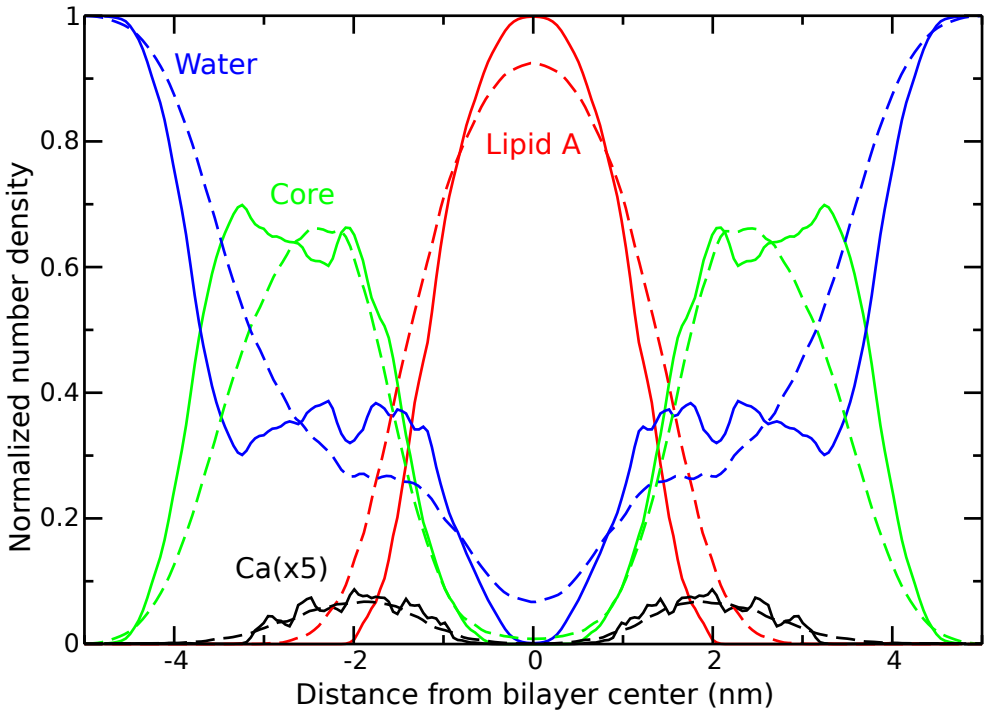

Figure 4.5: Normalized number density of the various components of the symmetric LPS/LPS bilayer, both AA (solid lines) and CG (dashed lines). (Color online.) The Ca^{2+} ion distribution has been multiplied 5× for clarity.

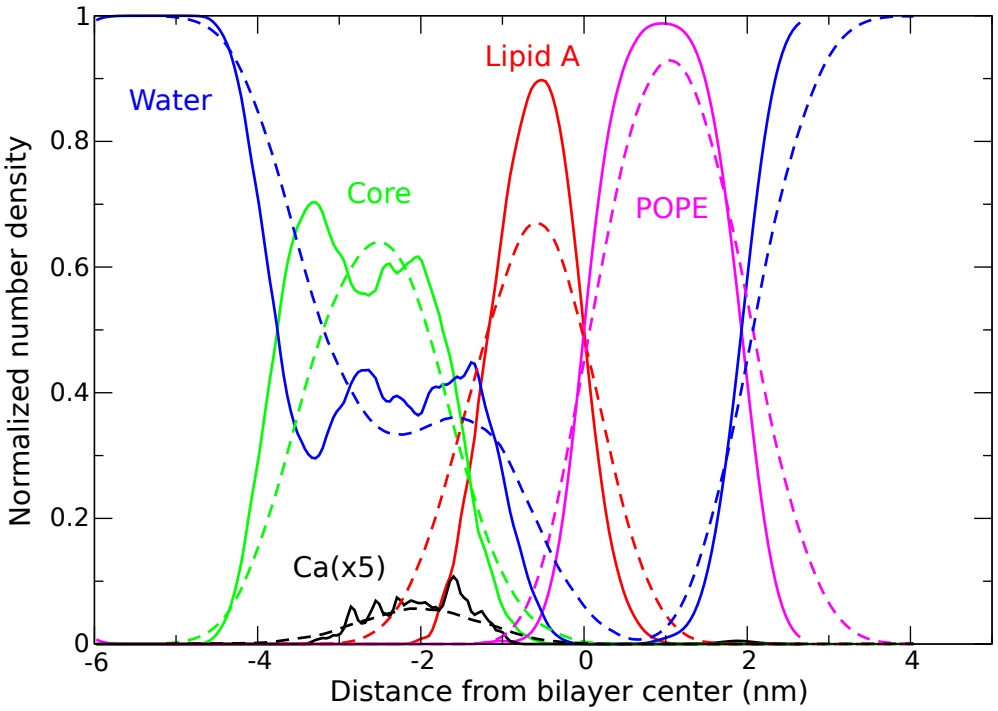

Figure 4.6: Normalized number density of the various components of the asymmetric LPS/POPE bilayer, both AA (solid lines) and CG (dashed lines). (Color online.) The Ca^{2+} ion distribution has been multiplied $5\times$ for clarity.

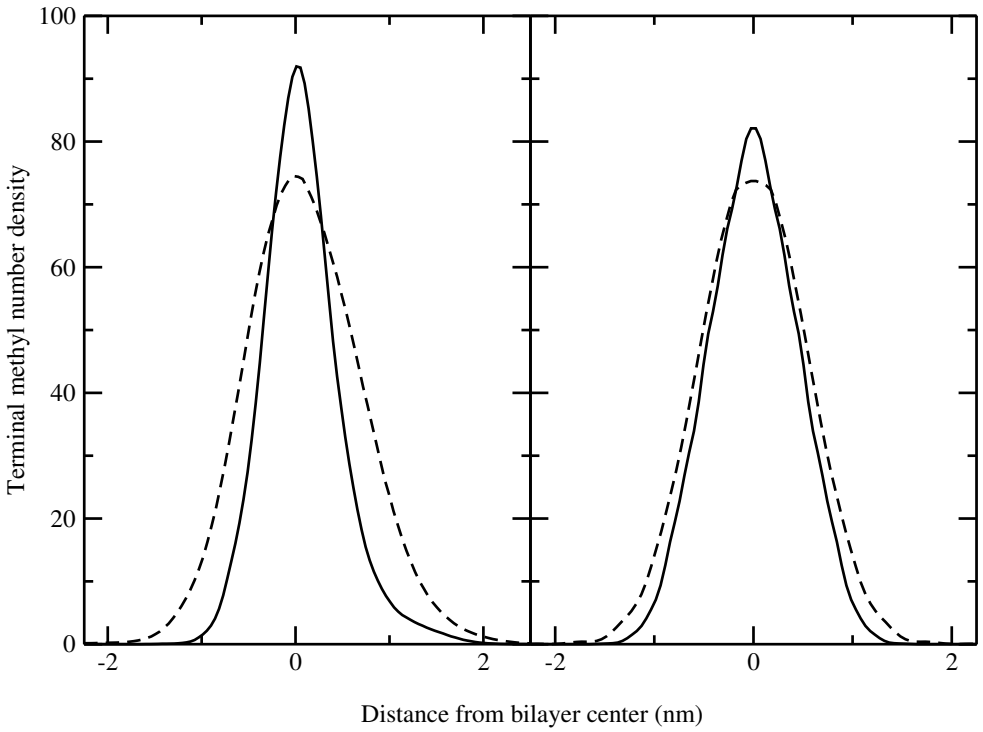

Figure 4.7: Number density of the terminal methyl (AA solid lines) or terminal virtual particle (CG dashed lines) for LPS/POPE (left) and LPS/LPS (right). The expansion in the CG distribution is attributed to undulations caused by the increased system size.

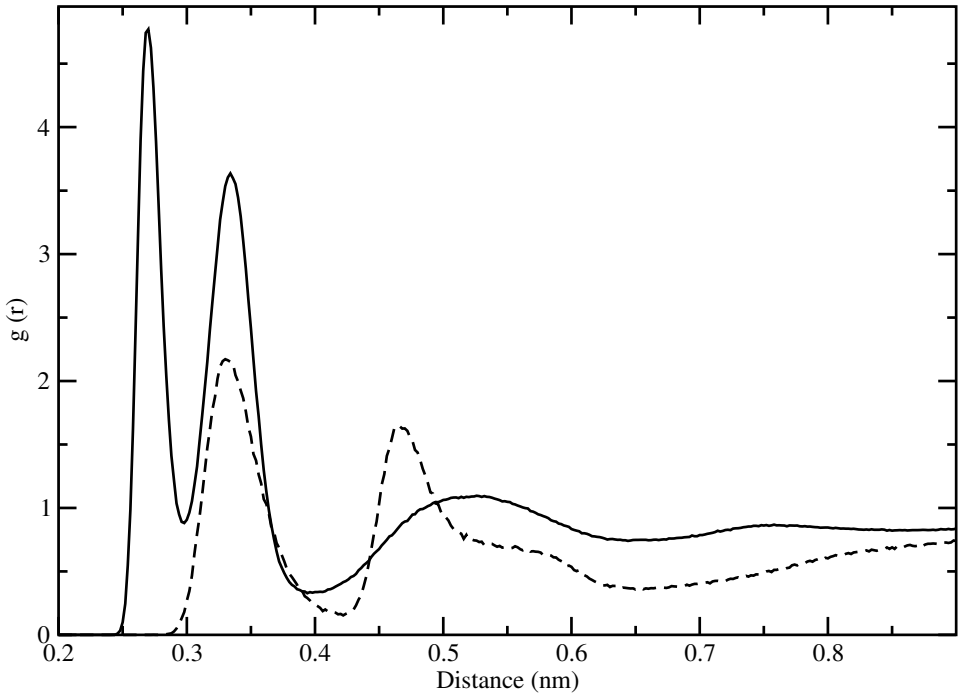

Figure 4.8: Radial distribution function showing the first 3 hydration shells of calcium ion for the AA(solid lines) as well as the second and third hydration shells for the CG(dashed lines) simulations (first hydration shell is implicit in the MARTINI ion model).

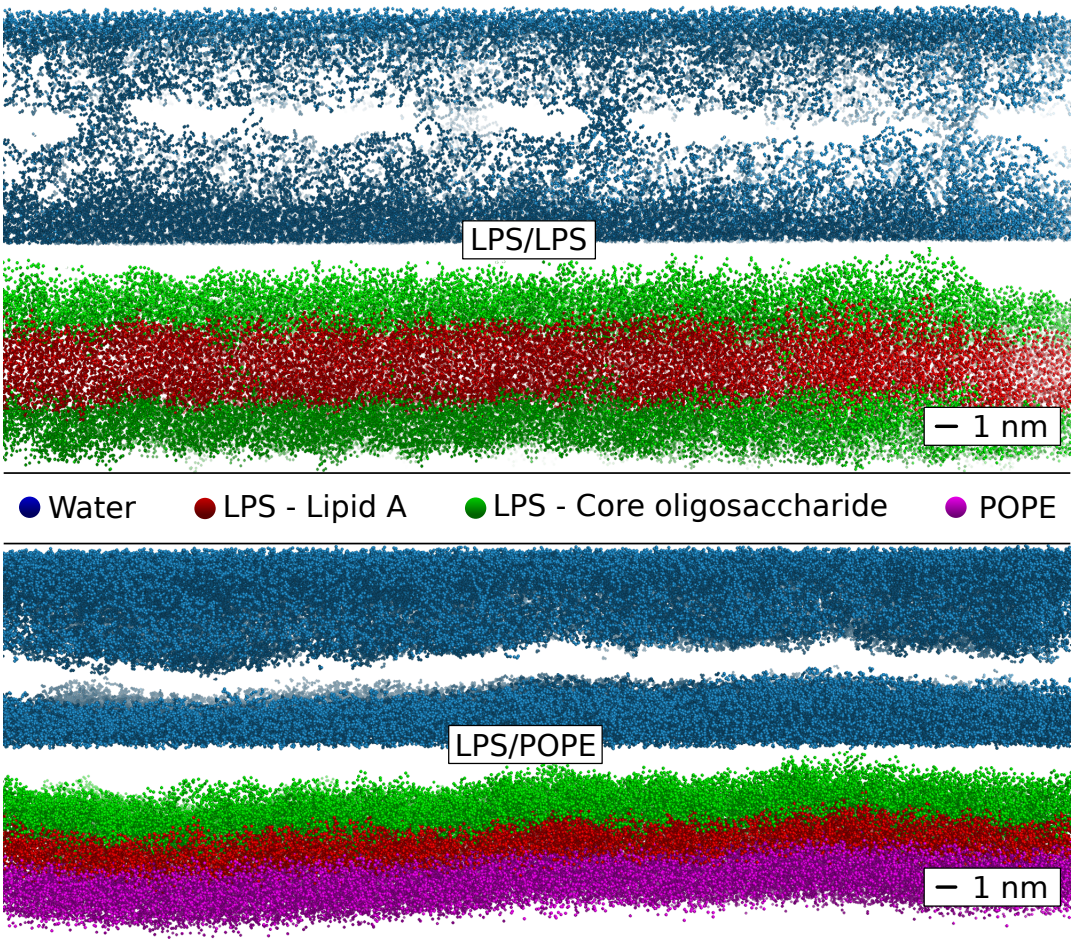

Figure 4.9: Snapshots of the coarse grained simulations, with the water separated from the lipids for clarity. Colour coding of the components are consistent with the schematic of Figs. 4.1, 4.5 and 4.6. (Top) LPS/LPS. (Bottom) LPS/POPE with the LPS in the top layer. Scale bars are approximate.

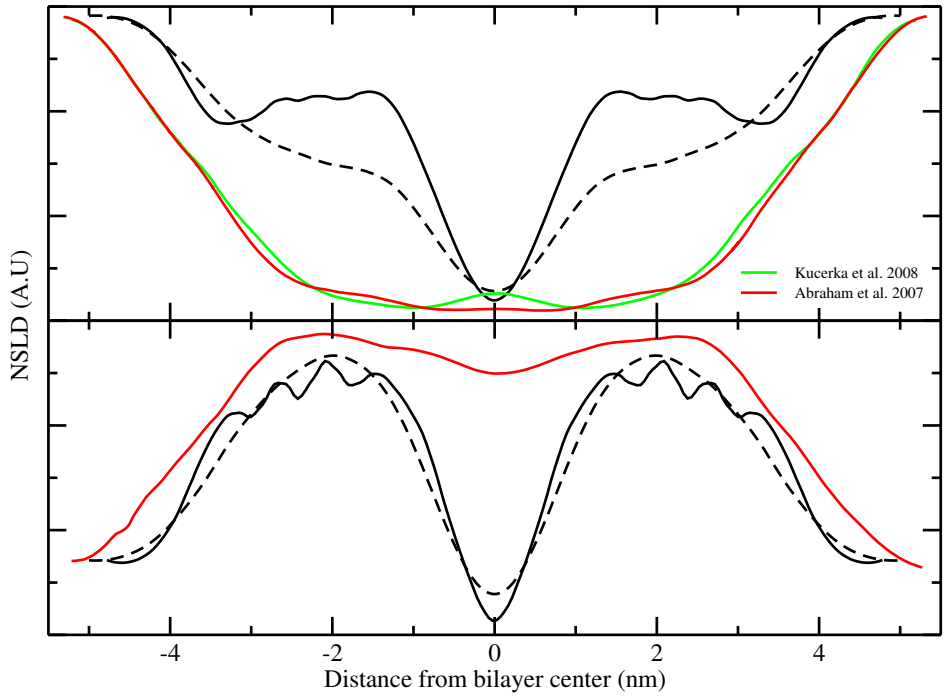

Figure 4.10: Comparison of the neutron scattering length density of the LPS/LPS simulations with data from Abraham et al. [34] (solid red line) and Kucerka et al. [33] (solid green line). (Color online.) The NSLD was computed for both the AA (solid black lines) and CG (dashed black lines). (Top) The NSLD for the whole water/lipid system, with 100% ^2H_2O. (Bottom) The NSLD with 8% ^2H_2O, for which water is essentially invisible to neutrons, and the resulting curve is primarily due to scattering from the lipids. The computed NSLD was scaled by a constant to visually match the experimental data.

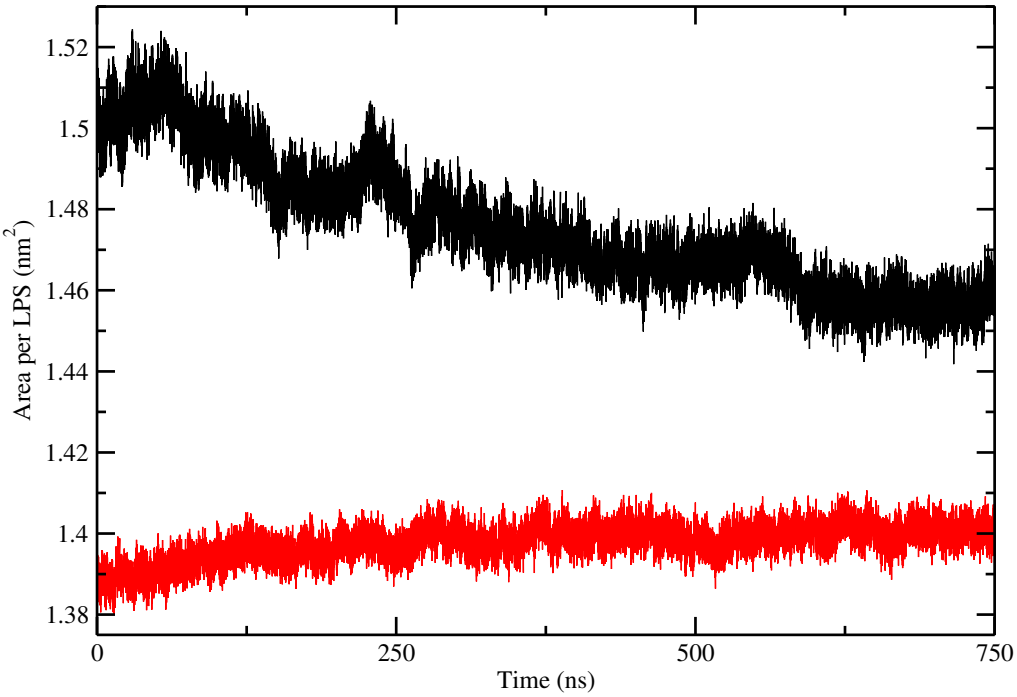

Figure 4.11: Time evolution of the area per lipid of AA LPS/POPE (black) and AA LPS/LPS(red).

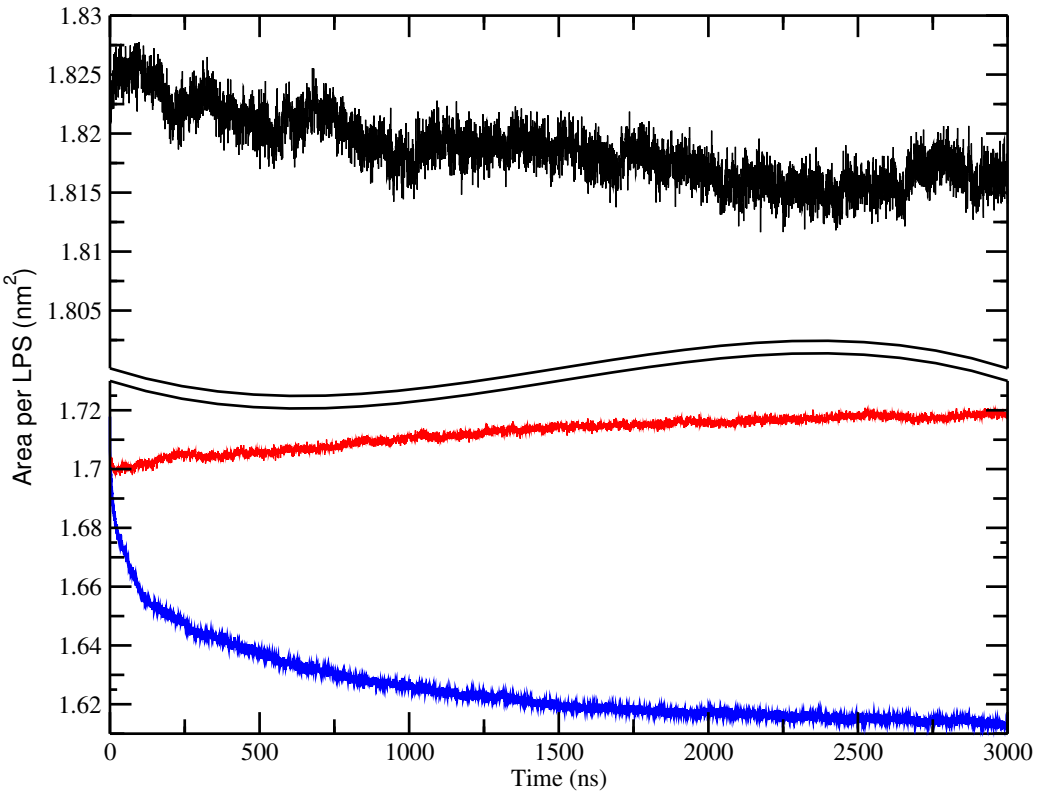

Figure 4.12: Time evolution of the area per lipid of CG LPS/POPE (black), CG LPS/LPS with polarized water(red) and CG LPS/LPS with nonpolarized water(blue).

Table 4.1: Membrane Physical Properties

System	APL_{LPS}(nm^2)	APL_{POPE}(nm^2)	Thickness (nm)	D_{LPS} (10^{-10}cm^{2}s^{-1})	D_{POPE} (10^{-7}cm^{2}s^{-1})
AA LPS/LPS	1.400	-	7.64	2.90	-
AA LPS/POPE	1.460	0.599	5.82	4.19	0.153
CG LPS/LPS	1.718	-	7.08	1.33	-
CG LPS/POPE	1.816	0.657	5.79	0.91	1.89
CG LPS/LPS (non-pol.)	1.613	-	7.30	1.40	-
CG LPS/POPE (non-pol.)	1.629	0.589	6.20	0.92	1.94

References

1. Rahme, L. G. *et al.* Use of model plant hosts to identify Pseudomonas aeruginosa virulence factors. *Proceedings of the National Academy of Sciences of the United States of America* **94,** 13245–13250 (1997).

2. Mahajan-Miklos, S., Tan, M. W., Rahme, L. G. & Ausubel, F. M. Molecular mechanisms of bacterial virulence elucidated using a Pseudomonas aeruginosa-Caenorhabditis elegans pathogenesis model. *Cell* **96,** 47–56 (1999).

3. Lomovskaya, O., Lomovskaya, O., Totrov, M. & Totrov, M. Guest commentary. *Society* **187,** 1879–1883 (2005).

4. Hancock, R. E. W. & Nikaido, H. Outer membranes of gram-negative bacteria. XIX. Isolation from Pseudomonas aeruginosa PAO1 and use in reconstitution and definition of the permeability barrier. *Journal of Bacteriology* **136,** 381–390 (1978).

5. Caroff, M. & Karibian, D. Structure of bacterial lipopolysaccharides. *Carbohydrate Research* **338,** 2431–2447 (2003).

6. Bobo, R. a. & Eagon, R. G. Lipids of cell walls of Pseudomonas aeruginosa and Brucella abortus. *Canadian journal of microbiology* **14,** 503–513 (1968).

7. Gilleland, H. E. & Lyle, R. D. Chemical alterations in cell envelopes of polymyxin-resistant Pseudomonas aeruginosa isolates. *Journal of Bacteriology* **138,** 839–845 (1979).

8. Schnaitman, C. a. & Klena, J. D. Genetics of lipopolysaccharide biosynthesis in enteric bacteria. *Microbiological reviews* **57,** 655–682 (1993).

9. Piggot, T. J., Holdbrook, D. A. & Khalid, S. Electroporation of the *E. coli* and *S. Aureus* Membranes: Molecular Dynamics Simulations of Complex Bacterial Membranes. *Journal of Physical Chemistry B* **115,** 13381–13388 (2011).

10. Wu, E. L. *et al.* Molecular dynamics and NMR spectroscopy studies of E. coli lipopolyUse of an efflux pump inhibitor to determine the prevalence of efflux pump-mediated fluoroquinolone resistance and multidrug resistance in Pseudomonas aeruginosa. saccharide structure and dynamics. *Biophysical Journal* **105,** 1444–1455 (2013).

11. Lins, R. D. & Straatsma, T. P. Computer simulation of the rough lipopolysaccharide membrane of Pseudomonas aeruginosa. *Biophysical Journal* **81,** 1037–1046 (2001).

12. Schroll, R. M. & Straatsma, T. P. Molecular structure of the outer bacterial membrane of Pseudomonas aeruginosa via classical simulation. *Biopolymers* **65,** 395–407 (2002).

13. Kirschner, K. N., Lins, R. D., Maass, A. & Soares, T. A. A glycam-based force field for simulations of lipopolysaccharide membranes: Parametrization and validation. *Journal of Chemical Theory and Computation* **8,** 4719–4731 (2012).

14. Marrink, S. J., Risselada, H. J., Yefimov, S., Tieleman, D. P. & Vries, A. H. D. The MARTINI Force Field : Coarse Grained Model for Biomolecular Simulations. **111,** 7812–7824 (2007).

15. Marrink, S. & Tieleman, P. Perspective on the Martini model. *Chemical Society Reviews* **42,** 6801–6822 (2013).

16. Marrink, S., de Vries, A. & Mark, A. Coarse Grained Model for Semiquantitative Lipid Simulations. *The Journal of Physical Chemistry B* **108,** 750–760 (2004).

17. Lopez, C. *et al.* Martini Coarse-Grained Force Field: Extension to Carbohydrate. *Journal of Chemical Theory and Computation* **5,** 3195–3210 (12 2009).

18. Lopez, C. A., Sovova, Z., Eerden, F. J. V., Vries, A. H. D. & Marrink, S. J. Martini force field parameters for glycolipids Martini force field parameters for glycolipids. *Journal of Chemical Theory and Computation* (2013).

19. López, C. A., Sovova, Z., Van Eerden, F. J., De Vries, A. H. & Marrink, S. J. Martini force field parameters for glycolipids. *Journal of Chemical Theory and Computation* **9,** 1694–1708 (2013).

20. Yesylevskyy, S., Schafer, L., Sengupta, D. & Marrink, S. Polarizable Water Model for the Coarse-Grained MARTINI Force Field. *PLOS Computational Biology* **6,** 1–17 (2010).

21. Ma, H., Irudayanathan, F. J., Jiang, W. & Nangia, S. Simulating Gram-Negative Bacterial Outer Membrane: A Coarse Grain Model. *The Journal of Physical Chemistry B.* ISSN: 1520-6106 (2015).

22. Periole, X. & Marrink, S. J. The martini coarse-grained force field. *Methods in Molecular Biology* **924,** 533–565 (2013).

23. Marrink, S., Risselada, J., Yefimov, S., Tieleman, P. & de Vries, A. The MARTINI Force Field: Coarse Grained Model for Biomolecular Simulations. *The Journal of Physical Chemistry B* **111,** 7812–7824 (27 2007).

24. Wojdyr, M. Fityk: A general-purpose peak fitting program. *Journal of Applied Crystallography* **43,** 1126–1128 (2010).

25. Jo, S., Kim, T., Iyer, V. & Im, W. CHARMM-GUI: A web-based graphical user interface for CHARMM. *Journal of Computational Chemistry* **29,** 1859–1865 (2008).

26. Jambeck, J. & Lyubartsev, A. Derivation and Systematic Validation of a Refined All-Atom Force Field for Phosphatidylcholine Lipids. *The Journal of Physical Chemistry B* **116,** 3164–3179 (10 2012).

27. Jambeck, J. & Lyubartsev, A. Another Piece of the Membrane Puzzle: Extending Slipids Further. *Journal of Chemical Theory and Computation* **9,** 774–784 (2013).

28. Hanwell, M. D. *et al.* Avogadro: An advanced semantic chemical editor, visualization, and analysis platform. *Journal of Cheminformatics* **4,** 1–17 (2012).

29. Bekker, H *et al.* in *Physics Computing '92* (eds DeGroot, R. & Nadrchal, J) 252–256 (World Scientific Publishing, 1993). ISBN: 981-02-1245-3.

30. Van Der Spoel, D *et al.* GROMACS: Fast, flexible, and free. *Journal of Computational Chemistry* **26,** 1701–1718 (2005).

31. Berendsen, H, van der Spoel, D & van Drunen, R. GROMACS: A message-passing parallel molecular dynamics implementation. *Computer Physics Communications* **91,** 43–56 (1995).

32. Kucerka, N. *et al.* Molecular Structures of Fluid Phosphatidylethanolamine Bilayers Obtained from Simulation-to-Experiment Comparisons and Experimental Scattering Density Profiles. *Journal of Physical Chemistry B* **119,** 1947–1956 (2014).

33. Kučerka, N. *et al.* Lipid Bilayer Structure Determined by the Simultaneous Analysis of Neutron and X-Ray Scattering Data. *Biophysical Journal* **95,** 2356–2367 (2008).

34. Abraham, T. *et al.* Neutron diffraction study of pseudomonas aeruginosa lipopolysaccharide bilayers. *Journal of Physical Chemistry B* **111,** 2477–2483 (2007).

35. Schneck, E. *et al.* Calcium ions induce collapse of charged O-side chains of lipopolysaccharides from *Pseudomonas aeruginosa*. *JJ. R. Soc. Interface* **6,** S671–S678 (2009).

36. Oliveira, R. G. *et al.* Crucial roles of charged saccharide moieties in survival of gram negative bacteria against protamine revealed by combination of grazing incidence x-ray structural characterizations and Monte Carlo simulations. *Physical Review E* **81,** 041901 (2010).

37. Komljenović, I., Marquardt, D., Harroun, T. A. & Sternin, E. Location of chlorhexidine in DMPC model membranes: a neutron diffraction study. *Chemistry and Physics of Lipids* **163,** 480–487 (2010).

38. Van Oosten, B. *et al.* Small molecule interaction with lipid bilayers: A molecular dynamics study of chlorhexidine. *Journal of Molecular Graphics and Modelling* **48,** 96–104 (2014).

Chapter 5

A MARTINI extension for chlorhexidine

5.1 Introduction

Chlorhexidine (CHX) is an effective antibacterial drug which attacks the membrane of key bacteria, yeasts, as well as certain viruses, making it a leading component in many mouth rinses, industrial cleansers and medical cleaning solutions [1–4]. At low concentrations of 0.5 mg/L, it is able to stop the bacteria from reproducing, limiting the spread of contamination, while a concentration of 10 mg/L is enough to lyse the cell, eliminating most of the bacterial culture [5].

Although the usage of CHX has been widely explored, the molecular mechanism of CHX uptake is still under investigation. CHX has been shown to cause damage to the outer layers of bacteria or yeast cells [6], however this was not shown to be the major cause of cell death. It was found that CHX partitions into the plasma membrane and cytoplasm of cells, where cell leakage of intracellular components followed leading to cell lysis [7]. At high concentrations of CHX, the intracellular components of the bacteria are seen to coagulate due to increased

sugar concentrations and the amount of leakage is reduced [8].

In our earlier studies, we have tested CHX in a model 1,2-dimyristoyl-sn-glycero-3-phosphocholine (DMPC) membrane [9, 10] in order to investigate the interaction of CHX with model lipid bilayers. We showed through experimental neutron scattering and Langmuir monolayers [9] as well as molecular dynamics simulations [10] that CHX has a high affinity for DMPC. However, experimentally we also observed that the membrane can absorb a remarkable amount of CHX molecules, as high as 1:3 CHX:DMPC, without losing its bilayer structure in any significant way. This seemingly contradicts previous observations of CHX's lytic properties.

Our earlier simulation studies were fully atomistic and therefore limited in size to a small patch of membrane, as well as a small number of CHX molecules. Unsatisfied with this type of MD simulation, we identified that a much larger lipid membrane as well as long simulation times was required in order for the CHX molecules to incorporate themselves into the membrane.

The overarching goal of the MARTINI force field has been to overcome such problems by reducing the computational complexity of the system using a mapping of approximately 4 heavy atoms to 1 virtual particle [11, 12]. This reduces the total amount of atoms by an approximate factor of 10 and also allows for a time step 10 times larger, corresponding to an approximate $100\times$ computational efficiency gain. This reduces the amount of calculations in order to increase the flexibility to allow for both larger systems and longer time scales to be simulated.

Here we propose a coarse grained model for three charged CHX models:

CHX^{0+}, CHX^{1+}, and CHX^{2+} fully compatible with the MARTINI force field. We compare and contrast the structure, orientation and location inside of a DMPC membrane between our all atom (AA) and coarse grained (CG) models. With these models it should be possible then to conduct a large, unbiased simulation, approaching the expected minimum inhibitory concentration.

5.2 MARTINI Parametrization

The coarse-graining method utilized to create the CHX models was based on our previous study of lipopolysaccharides which showed success utilizing a bottom up approach, building a coarse grained model based on AA simulations [13]. An AA coordinate file of CHX in a water box was converted to CG by mapping real atoms to virtual particles at the location of the center of mass of the atom collection they represent, as shown in the schematic of Figure 5.1. The mapping was chosen to be similar to the virtual particle choice in the amino acids Tyr, Arg and Lys used in the MARTINI force field version 2.2P, as these amino acids guided our original choices for the chlorophenol (CPL), biguanide (BGU) and hexane (HEX) residues of our AA CHX model. [12, 14] See Figure 5.1 for a schematic of the atom groupings and naming of CHX.

A 100 ns AA simulation of CHX in a water-filled box using our previously published topology was used to construct histograms of the probability distributions of bond lengths, angles, and dihedrals of the CG-mapped centres of mass. CG simulations of CHX in water were then performed and the resulting CG

histograms of bonds, angles, and dihedrals were directly compared to the respective AA histograms. Due to the choice of virtual particles, the histograms for the bond and angle parameters were for the most part Gaussian-shaped and single peaked. The dihedrals however, were not as well behaved. Generally, steric interactions did a good job in recreating the dihedral histograms, however weak spring terms were added in the biguanide section as well as the hexane linker chain to keep them planar as observed in the AA simulations.

The spring strength and harmonic equilibrium parameters were iteratively adjusted using 100 ns CG simulations until all distribution for bonds, angles and dihedrals matched those from the AA simulations. For the very first iteration, the initial bond equilibrium length was set to the exact centres of the AA histograms. The bonds inside the ring structures were chosen to be constrained, while all other bonded parameters were set to be harmonic with initial spring strength of 1,000 kJ mol^{-1} nm^{-2}, angles of 100 kJ mol^{-1} deg^{-2} and dihedrals of 1 kJ mol^{-1} deg^{-2}. Each CG particles' mass was taken to be the sum of the constituent atoms in which it represented and their charges were set to 0. Particle types were chosen from the pre-existing types contained in the MARTINI force field to ensure compatibility. The 3-to-1 mapping using *S*-type particles were chosen for the ring structures.

In order to test for the effects of a hydrophobic environment versus water solvent on the bond parameters, additional bond length, angle, and dihedral distribution histograms were created for a 100 ns AA simulation for 1 CHX in a 128 DMPC membrane. The topology for DMPC was taken from Slipids, which

has a superior record of matching neutron diffraction data and recreating apolar environments. [15, 16] A 128 CG DPPC (di16:0-PC) membrane model was downloaded from the MARTINI website and converted to 128 DMPC (di14:0-PC) by removing 1 particle from the end of each tail. The virtual particles for the 14 carbons of the DMPC acyl chain they are meant to represent were re-assigned and re-weighted. The first carbonyl was assigned to the CG backbone atom, and the remaining 13 carbons split 5-5-3 among the three CG atoms. The membrane was then equilibrated for 100 ns [12]. One CHX molecule was then added and simulated for another 100 ns in order for it to have enough time to enter the membrane and again become equilibrated.

The iterative parameterization process was repeated to arrive at a CG topology for CHX when in the membrane. Density plots locating the depth in the bilayer of the CPL, BGU and HEX sections of CHX were also considered in this part of the process. The particle types were adjusted until the depths of all three sections matched. At this point the CHX model was split into three; neutral, +1 and +2 charged CHX models. For the charged models, the neutral *P4* particle of BGU section closest to HEX section (particles 5 & 8) was changed to a +1 charged *Qd* type (only one BGU for the +1 charge and both BGU for the +2 model). The iterative process for the bonded parameters were then continued with 100 ns simulations with simulation until the histograms met those of the AA CHX in a DMPC membrane. All particle types, masses and charge can be found in topology (*.itp) files deposited at http://www.physics.brocku.ca/MARTINI/.

5.3 CHX Parameterization Validation

The CG bilayer system of CHX and DMPC reproduces the expected bilayer structural profile. Figure 5.2 shows the volume probability of the lipid-only components of the CG membrane along the bilayer normal. There are two common definitions of membrane thicknessD_{HH} and D_{B} marked as dashed lines. D_{HH}, being the headgroup-to-headgroup distance, and D_{B}, defined as where the water profile drops to a volume probability of 50%. Both of these are used as a measure of bilayer thickness to help establish a reference point for the location depth of CHX. The MARTINI atom types for CG-CHX were specifically chosen such that the whole molecule resides the same distance from the bilayer centre as determined by the AA-CHX, which has been shown to be in agreement with experimental neutron diffraction results. [10]

The resulting distributions of the three CHX sections, and for all three charge models, are shown in the lower part of Figure 5.2, for the right-half of the bilayer. CHX sits just below the hydrophobic/aqueous interface at $D_{\mathrm{HH}}/2$. For the AA models, the centre of the CHX distributions shift further away from the centre of the membrane with increasing charge. In the CG model, adding the charge to the BGU particle pulls all of the sections out of the membrane, correctly repositioning all three sections of the CHX molecule.

Figures 5.3, 5.4 and 5.5 compare the AA and CG distributions for all of the CHX bond lengths, angles and dihedrals respectively. Since the molecule is symmetrical, only the bonded terms of the one side of the molecule are shown since the equivalent distributions of the opposite side are identical. The bonded terms

of the rings are also omitted since constraints are used here, the bonds and angles of the ring structure are trivially matched with very sharp, narrow distributions.

The bond length distributions are mostly single peaked and moderately symmetric, and could be reproduced with a simple harmonic spring term due to the low amount of internal degrees of freedom inside each of the virtual particle assignments. There was a single exception between the two particles of the BGU section, which was doubly peaked (Figure 5.3 B). For this, the average length was taken as the centre and the half width at half max (HWHM) was matched with that of the more prominent peak. The effects of the surrounding environment being water or DMPC made little difference to the bond length distributions.

Many of the angle terms were also singly peaked and could also be reproduced with a harmonic spring term (Figure 5.4). For angles with more than one peak, the average angle was taken as the centre. Angles approaching 180° are difficult to reproduce with harmonic terms. The harmonic spring term could either accurately reproduce the potential strength, ie. distribution width, or the equilibrium position, but not both simultaneously. Figure 5.4 D demonstrates an angle approaching 180° which reproduces the proper equilibrium position, however the potential strength is marginally too large making the distribution narrower. The surrounding environment has a small effect on the angle distributions. In the aqueous environment, CHX has a larger range of conformational changes, corresponding to the widening of the angle distributions in water as compared to in DMPC. Since CHX resides primarily inside of the membrane, the final CG model was based on fitting the distributions from the DMPC environment rather

than those from the water. Despite this choice, the water distributions are still fit fairly well.

The dihedral terms are the most difficult of the parameters to match due to the fact that the virtual particles rarely make dihedral distributions that fit the typical functions used for torsions, ie. that are sinusoidal. In most cases it was not possible to achieve the correct equilibrium angle nor the proper potential strength. Therefore we attempted to get an overall agreement in general distribution shape, with the correct number and location of maxima and minima, using a combination of cosine dihedral terms. Figure 5.5 A shows that a cosine dihedral term correctly recreated two minimas at this proper location. Figure 5.5 B, C and D show a single peaked cosine matching the distribution as best as possible. The surrounding environment has a large effect on the dihedral terms of CHX, with a general increase in the width of the distribution of angles in water compared to inside DMPC. Again, we chose the dihedral tems which could best recreate the distributions in a DMPC environment rather than in water. We see in Figure 5.5 B, that this can have some adverse effects where in water the dihedral term creates a narrower distribution where there should be a wider one, limiting the flexibility of the molecule.

To measure the overall effect of limiting the internal degrees of freedom during the coarse graining process, the distance between virtual particles 1 and 12 was recorded. These are the particles on the ends of the molecule and thus their distance corresponds to an extended versus folded conformation, and are compared with the intra-Cl to Cl atom distance of AA simulations. Previous AA

simulations [10] demonstrated that CHX^{1+} spends time alternating between an extended and folded conformation in water, however has a narrower distribution, in a semi-folded conformation, once it has entered the membrane. This result was reproduced in this study, shown in Figure 5.6. The AA CHX spends time with Cl-Cl distances ranging from 0.4-2.7 nm, with no preferred conformation in water. However, in DMPC it has a much narrower distribution ranging from 1.1-2.4 nm, centred at 1.7 nm. The CG model recreates this same effect; in water, the CG model has no preferred extended or folded orientation, while in DMPC the distribution significantly narrows into a semi-folded state. The CG distribution in DMPC is not as narrow as the AA simulation, with a HWHM of 0.99 in comparison to the HWHM of 0.39 nm for the AA distribution. The two-dimensional, x/y radius of gyration of CHX^{1+} while in the membrane was calculated to be 0.56 nm, one-third the most probable end-to-end dimension. This difference is easily attributed to a random orientation, made possible by the large inter-CHX^{1+} even at high concentrations.

5.4 Model Discussion

The CG model for CHX that is presented in this paper has great potential to enhance the study of CHX through the use of molecular dynamics. The model was created as an extension to the MARTINI force field, using its particle types so that it is both forward and backwards compatible with future force field releases. As the MARTINI force field continues to extend its library of molecules,

so does the potential to study the antibacterial effectiveness of CHX in different environments. As per most MARTINI simulations, we gain an approximate one order of magnitude speed increase from utilizing a larger time step and another order of magnitude from the decrease in the number of particles simulated. Table 5.1 compares the system size and computational cost to simulate the 1:100 and 1:10 CHX:DMPC concentrations for both the AA and CG simulations. All simulations were run on the same computer utilizing 8 threads and a single GPU. Although the CG simulations have a much larger system and are simulated for longer periods, the computational cost remains similar to that of the smaller AA simulations. Without the efficiency gain of using a coarse grain model, this study would not have been reasonable, as such an AA simulation would have an outrageously large computational cost.

The biggest compromise made in the creation of our model, and indeed with any such model of a membrane active molecule, is that it could not completely fit the bonded parameters in both aqueous and lipid environments. In our model we chose to fit to the parameters in a lipid bilayer because we are interested in the study of CHX in membranes, rather than in water. Nevertheless, we have shown that our model does not suffer a large negative effect in an aqueous solution due to this parameterization choice. However there may be subtle consequences that affect its mechanics in an aqueous solution.

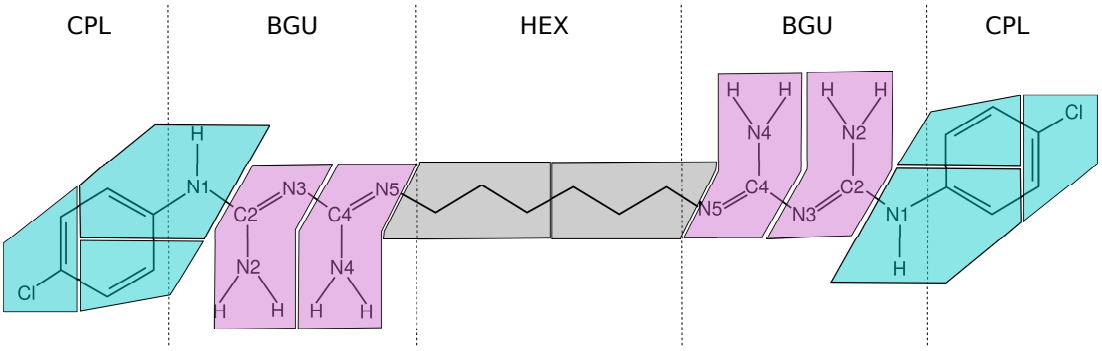

Figure 5.1: CG mapping and naming schematic of CHX sections and virtual particles

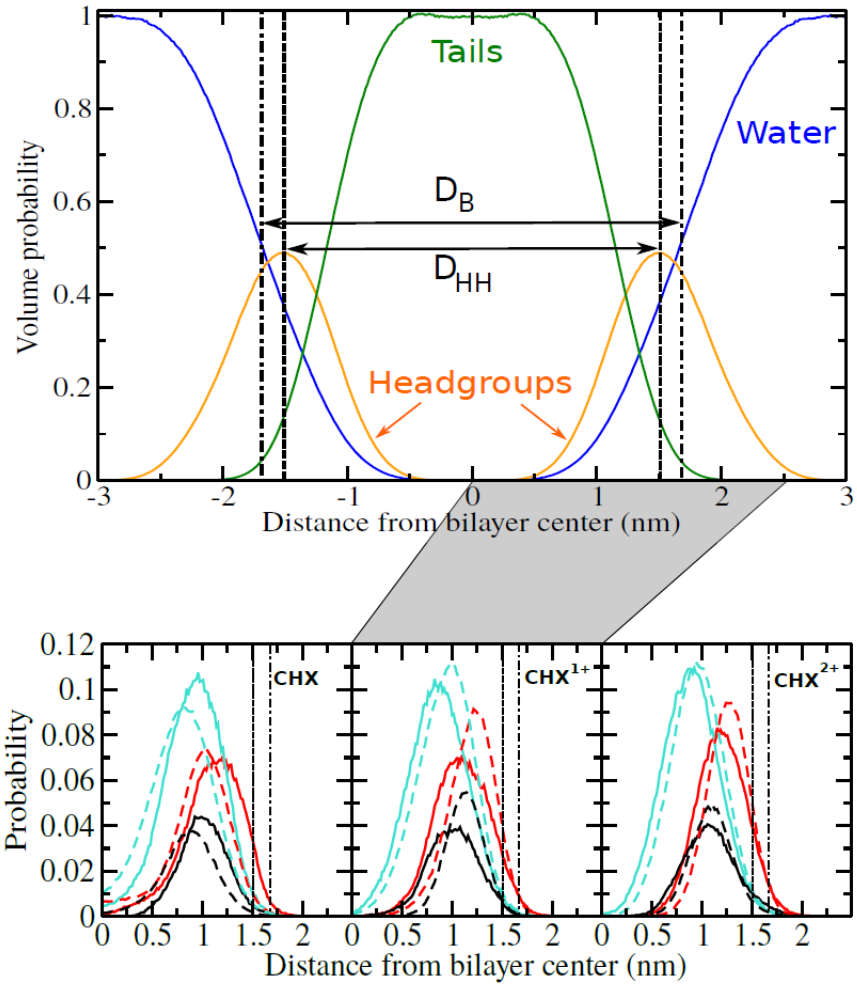

Figure 5.2: Volume probability of AA DMPC system with D_B (width of membrane with less than 50% volume probability of water) and D_{HH} (headgroup to headgroup width) thickness values marked (top). Volume probability of each of the 3 CHX sections: CPL (teal), BGU (red) and HEX (black) for the CHX^{0+}, CHX^{1+}, and CHX^{2+} models (bottom).

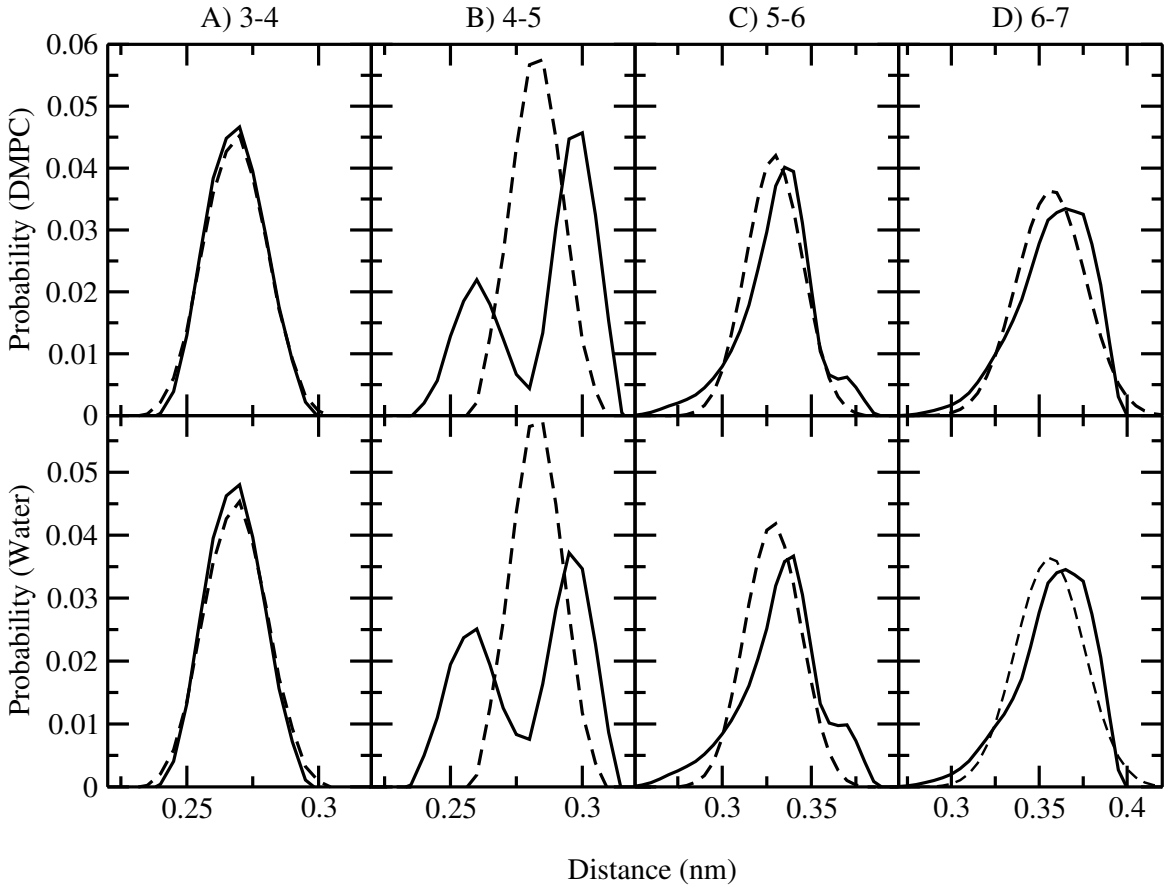

Figure 5.3: Bond distributions for AA (solid lines) and CG (dashed lines) CHX in DMPC (top row) and water (bottom row) between particles A) 3-4, B) 4-5, C) 5-6 and D) 6-7.

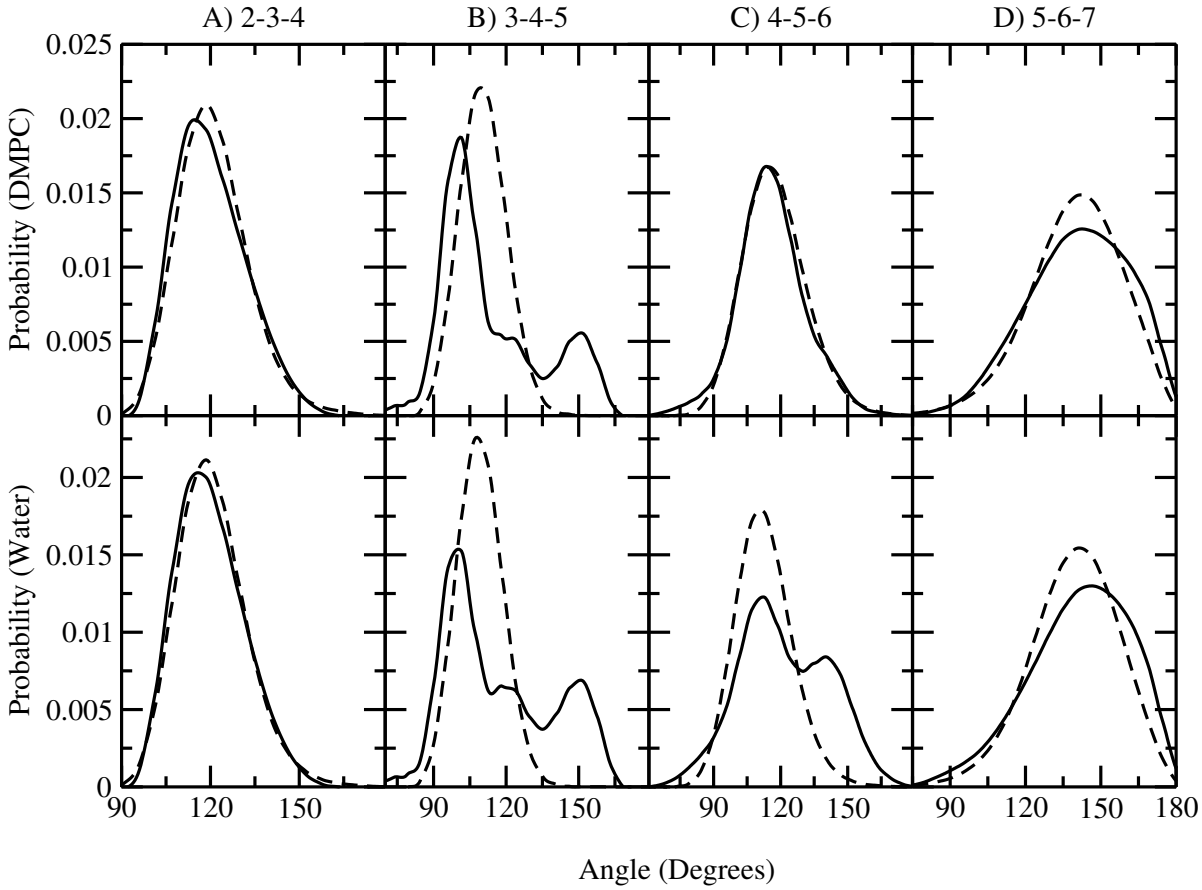

Figure 5.4: Angle distributions for AA (solid lines) and CG (dashed lines) CHX in DMPC (top row) and water (bottom row) between particles A) 2-3-4, B) 3-4-5, C) 4-5-6 and D) 5-6-7.

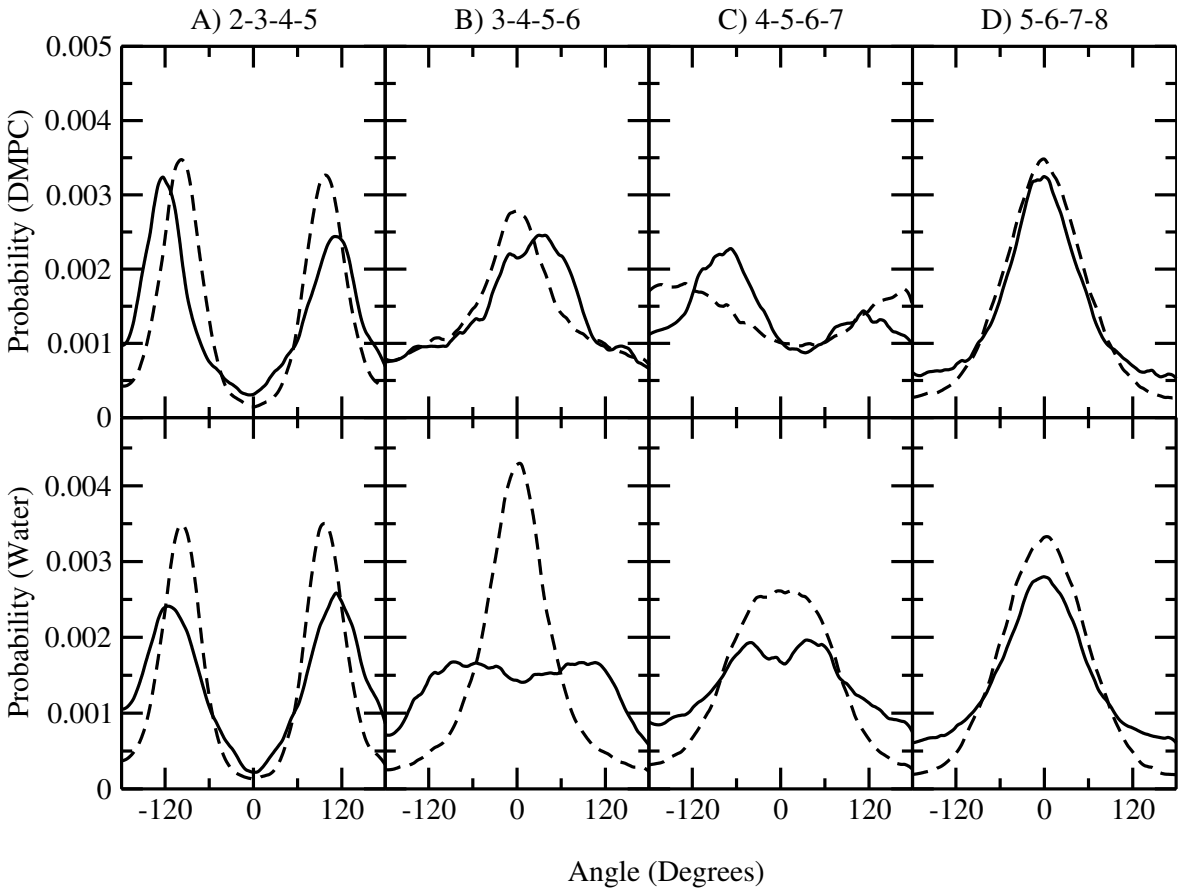

Figure 5.5: Dihedral distributions for AA (solid lines) and CG (dashed lines) CHX in DMPC (top row) and water (bottom row) between particles A) 2-3-4-5, B) 3-4-5-6, C) 4-5-6-7 and D) 5-6-7-8.

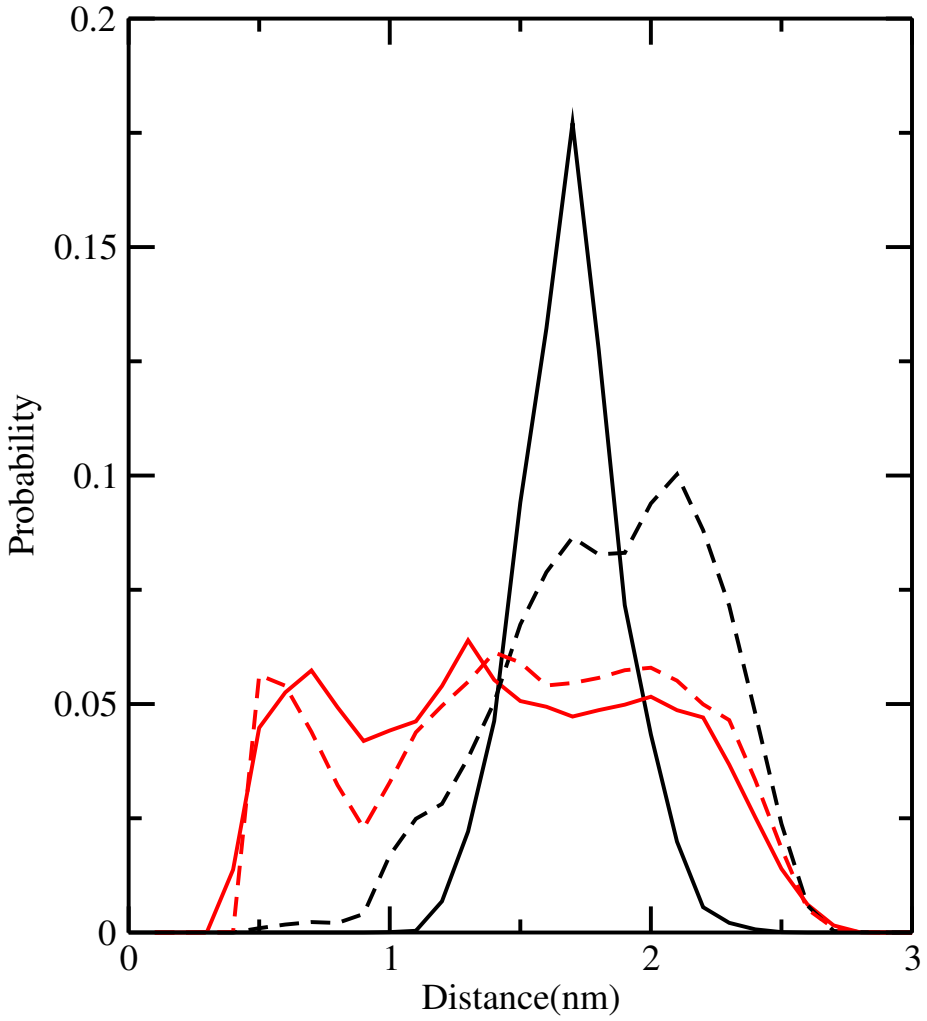

Figure 5.6: Virtual particle 1-12 distance to represent approximate Cl-Cl distance in DMPC (black) and in water (red) for the AA (solid lines) and CG (dashed lines) CHX^{1+} model.

Table 5.1: AA and CG system size and computational cost comparison. Both simulation types utilize 8 threads and 1 GPU.

	CHX:DMPC	# Lipids	# Waters	# Atoms	Length (ns)	Rate (ns/day)	GPU days
AA	1:100	128	3,840	26,690	200	35.3	5.66
	1:10	128	3,840	27,416	200	35.3	5.67
CG	1:100	900	17,991	63,090	250	191.9	1.30
	1:10	900	17,910	63,900	1,500	189.1	7.934

References

1. Gilbert, P & Moore, L. E. Cationic antiseptics : diversity of action under a common epithet. *Journal of Applied Microbiology* **99,** 703–715 (4 2005).

2. Munksgaard, C. B. Antiplaque biocides and bacterial resistance : a review. *J clin Periodonol* **29,** 965–974 (2002).

3. Chen, L., Bromberg, L., Hatton, T. A. & Rutledge, G. C. Electrospun cellulose acetate fibers containing chlorhexidine as a bactericide. **49,** 1266–1275 (2008).

4. Sinisterra, R. D. *et al.* A novel polymeric chlorhexidine delivery device for the treatment of periodontal disease. *Biomaterials* **25,** 3743–3750 (2004).

5. Adam P. Fraise, S. S. Jean-Yves Maillard. *Principles and Practices od Disinfection Preservation & Sterilization* 4th (Blackwell Publishing Ltd, 2004).

6. Moug, T. E., D.T., R., Furr, J., El-Falaha, B. & Russell, A. Antiseptic-induced changes in the cell surface of a chlorhexidine-sensitive and a chlorhexidine-resistant strain of Providencia stuartii. *Journal of Antimicrobial Chemotherapy* **16,** 685–689 (1984).

7. Hiom, S., Furr, J., Russell, A. & Dickenson, J. Effects of chlorhexidine diacetate and cetylpyridinium chloride on whole cells and protoplasts of Saccharomyces cerevisiae. *Microbios.* 111–20 (1993).

8. Barrett-Bee, K, Newboult, L & Edwards, S. The membrane destabilising action of the antibacterial agent chlorhexidine. *FEMS Microbiology Letters* **1-2,** 249–253 (1994).

9. Komljenović, I., Marquardt, D., Harroun, T. A. & Sternin, E. Location of chlorhexidine in DMPC model membranes: a neutron diffraction study. *Chemistry and Physics of Lipids* **163,** 480–487 (2010).

10. Van Oosten, B. *et al.* Small molecule interaction with lipid bilayers: A molecular dynamics study of chlorhexidine. *Journal of Molecular Graphics and Modelling* **48,** 96–104 (2014).

11. Marrink, S., de Vries, A. & Mark, A. Coarse Grained Model for Semiquantitative Lipid Simulations. *The Journal of Physical Chemistry B* **108,** 750–760 (2004).

12. Marrink, S. J., Risselada, H. J., Yefimov, S., Tieleman, D. P. & Vries, A. H. D. The MARTINI Force Field : Coarse Grained Model for Biomolecular Simulations. **111,** 7812–7824 (2007).

13. Van Oosten, B. & Harroun, T. A MARTINI extension for Pseudomonas aeruginosa PAO1 lipopolysaccharide. *Journal of Molecular Graphics and Modeling* **63,** 125–133 (2016).

14. Monticelli, L. *et al.* The MARTINI Coarse-Grained Force Field: Extension to Proteins. *Journal of Chemical Theory and Computation* **4,** 819–834 (5 2008).

15. Jambeck, J. & Lyubartsev, A. Another Piece of the Membrane Puzzle: Extending Slipids Further. *Journal of Chemical Theory and Computation* **9,** 774–784 (2013).

16. Kucerka, N. *et al.* Molecular Structures of Fluid Phosphatidylethanolamine Bilayers Obtained from Simulation-to-Experiment Comparisons and Exper-

imental Scattering Density Profiles. *Journal of Physical Chemistry B* **119,** 1947–1956 (2014).

Chapter 6

Testing high concentrations of membrane active antibiotic chlorhexidine

6.1 Introduction

Our first simulation study on CHX was fully atomistic and therefore limited in size to a small patch of membrane, as well as a small number of CHX molecules. Unsatisfied with this type of MD simulation, we identified several serious drawbacks. First, with 128 lipids in an 8x8x2 formation, the system was much too small to allow for any significant membrane undulations or defects to be observed with the addition of CHX. Secondly, we had decided on an unbiased simulation, whereby the CHX was introduced into the aqueous phase and allowed to make their own room among the lipids in their own time. Removing lipids prior to simulation, in order to accommodate such a small molecule, would be questionable and defeat the purpose of the simulation. Furthermore, adding a significant number of CHX resulted in a huge expansion of the computational

time, as the many CHX molecules spent a great deal of time interacting with each other in the aqueous environment before interacting with the lipids. CHX inserting into the membrane was shown to lower the system energy, however the energy difference was not great, and thus the system was slowly driven to equilibrium.

We concluded that titrating small numbers of CHX into the system should reduce the time of insertion. This would be true at least until the concentration of CHX in the bilayer was sufficiently high that the free energy gained by further insertion is reduced, slowing the time of insertion once again. We also reasoned that a much larger system should be used so that any disruption or instability in the membrane may be observed. Both of these ideas are realistically out of reach for an atomistic simulation in a reasonable computational time frame.

We perform a unique titration-like experiment where we introduce small numbers of the CHX molecule into a model DMPC membrane at set intervals. From this we are able to study the concentration effect of CHX, as well as create equilibrated systems of varying CHX concentration. We demonstrate that just as in a concentration-dependant experiments, the amount of energy gained by adding CHX into the membrane decreases as we saturate the membrane. We then performed a controlled cooling of these systems to recreate a computational calorimetry experiment, in which we were able to track the changes to the main phase transition as a function of CHX and cholesterol concentration.

The overarching goal of this study is to create and utilize CHX models to test a large number of molecules in a model DMPC membrane. We look specifically

for membrane conformational changes, changes in the membrane's main phase transition as well as CHX localized aggregation which could lead to membrane instability. We make observations on the lowered affinity between the molecule and the membrane, with increased saturation, leading to increased simulation time necessary to reach an equilibrium state and thus the importance of using a coarse grained model such as the MARTINI force field.

6.2 Methods

6.2.1 Simulated Titration

Our goal is to simulate a DMPC bilayer fully loaded with CHX at concentrations as high as 1:10 CHX:lipid. Rather than construct a bilayer with the CHX already in place, which would require guessing how to make room for the molecules and where to place them, we decided to "titrate" the CHX into a unperturbed bilayer. Based upon our previous experience, we knew that CHX has a high affinity for the bilayer, and CHX added into the water phase would rapidly incorporate into the lipid. Any change to the bilayer structure thus caused could then be monitored.

CHX contains a biguanidine linking a chlorphenol ring to its hexane hydrocarbon center (See Figure 6.1), making it member of the class of biguanides, an important group of compounds regularly utilized for their proven antibacterial applications [1–6]. Biguanides can appear in a variety of different forms due to a variety of tautomers and protonation states [7, 8]. A similar compound to CHX,

poly(hexamethylene-biguanide hydrochloride)(PHMB), is assumed to be in its singly protonated state in water, with calculated pKa values of approximately 13.5 and 3.03 for pKa_1 and pKa_2 respectively [7, 8]. In comparison, CHX was calculated to have three pKa values of 10.15, 9.55 and 3.10 [8]. The lower pKa values for CHX indicate that it is harder to protonate than deprotonate than PHMB due to the fact that the chlorophenyl is less electron donating than an alkyl group. It is comparatively electron withdrawing; withdrawing electron density will make the adjacent N atom more difficult to protonate [8]. However the pKa of CHX or any biguanide has only been studied in a polar environment and as such, there is uncertainty to its protonation state in an apolar environment such as a membrane. Therefore, for our experiments with concentration, we focused on the CHX^{1+} protonation state.

A single titration step then included adding 9 CHX^{1+} molecules (1% concentration) in a 3×3 configuration, arranged as far apart as geometrically possible to minimize their interactions with each other. The CHX were also equally distant from the bilayer and its periodic boundary image, meaning each CHX could freely enter the bilayer from either side. The system was then simulated in 500 ns intervals until all 9 CHX^{1+} molecules were fully inserted into the membrane. This titration step was then repeated a further 10 times so that it created 11 model membranes with equilibrated concentrations of CHX^{1+} increasing to 1:10 CHX:lipid.

6.2.2 Membrane Creation

A pure DMPC bilayer consisting of 900 CG lipids was constructed using the INSANE membrane building tool and equilibrated for 250 ns [9]. Membranes with DMPC and CHX were constructed using the simulated titration method as described above in order to give CHX concentrations ranging up to 10:1 lipid:drug. These membranes consisted of 900 DMPC lipids using the MARTINI DLPC topology with modified masses with the first carbonyl assigned to the CG backbone atom, while the remaining 13 carbons were split 5-5-3 among the three CG atoms of the tail. A second membrane consisting of 800 DMPC lipids and 80 cholesterol (CHOL) molecules was created using the insane membrane building tool [9], and equilibrated for 250 ns. Another titration of CHX into the DMPC:CHOL membrane was performed adding 8 CHX molecules 5 times to achieve a range of concentrations up to 1:20 CHX:DMPC. For subsequent lower cholesterol concentrations, an equal amount of cholesterol molecules were removed from each leaflet at random from each of the various equilibrated 10:1:X DMPC:CHOL:CHX membranes. The membranes were then equilibrated for 250 ns to allow for the membrane fill in the gaps of the missing cholesterol molecules.

6.2.3 Computational Calorimetry

Each membrane was first equilibrated at 36°C for 250 ns. The temperature was then reduced by steps of 2° C and simulated for 25 ns at each temperature, until the membrane exhibited signs of a transition from liquid to gel state. At this

point, the coldest temperature without the onset of a transition was simulated for 100 ns. If the membrane again went through the transition at this temperature, the next warmest simulation was repeated for 100 ns until no transition occurred. The temperature step was then reduced to cooling by steps of 0.5°C at each temperature and simulated for 100 ns (several other temperature steps and simulation times were tested see Results). The cooling was continued until the system reached 0°C or until the system was completely in the gel phase, whichever happened latest.

The specific heat at constant pressure was calculated as defined in terms of the fluctuations in energy (E) as:

$$c_p = \frac{< E^2 > - < E >^2}{k_B T^2}$$

where k_B is Boltzmann's constant and T is the average temperature of the simulation. Figure 6.9 shows the resultant specific heat vs temperature calculated for the pure DMPC membrane and the three simulations' potential energy plots which gave rise to the calculated specific heat values around the peak at the phase transition.

6.2.4 MD Simulation Details

All simulations were performed using GROMACS 5.0.4 [10]. CG simulations used a time step of 10 fs. The temperature was maintained for the lipids, cholesterol, CHX and the solvent independently with a coupling constant of 10 ps

using a Nose-Hoover thermostat. Semi-isotropic coupling was used to maintain a pressure of 1.0 bar using the Parrinello-Rahman barostat with a 1.0 ps coupling constant and compressibility of 4.5×10^{-5}. The Verlet group scheme was used for pair lists which were updates every 20 steps. Both Coulomb and LJ potentials are shifted to zero at an exact cut-off value of 1.2 nm. The polarized water of MARTINI 2.2P, was used with a screening dielectric of $\epsilon_r = 2.5$.

An atomistic simulation using the Slipids force field [11–13] was also performed on a pure DMPC membrane consisting of 200 lipids and 6000 TIP3p water molecules built by CHRAMM-GUI [14]. A timestep of 2 fs was used with the system in a periodic xyz orthorhombic box. The temperature was maintained for DMPC and the water independently with a coupling constant of 1.0 ps using a Nose-Hoover thermostat. Semi-isotropic coupling was used to maintain a pressure of 1.013 bar using the Parrinello-Rahman barostat with a 10 ps coupling constant and compressibility of 4.5×10^{-5}. The Verlet group scheme was used for pair lists which were updates every 20 steps. Both Coulomb and LJ potentials are shifted to zero at an exact cut-off value of 1.4 nm.

6.2.5 Weighted Histogram Analysis Method (WHAM)

Twelve sets of umbrella sampling simulations were conducted, six AA and six CG, to determine the potential of mean force (PMF) and free energy experienced by CHX or solvent as it is pulled through the lipid bilayer [15]. The six sets include pulling each of the 3 CHX charge models into a pure DMPC membrane, pulling one CHX^{1+} into a 1:10 CHX^{1+}:DMPC membrane, pulling water

into a pure DMPC membrane, and finally, pulling water into a 1:10 CHX^{1+}:DMPC membrane.

For the simulations with a CHX molecule as the pull group, the system was built with the membrane at the centre of the box, and a single CHX molecule in the water, equidistant to either side of the membrane, taking periodic boundary conditions into account. The CHX molecule was held in place with a harmonic constraint for a 1 ns equilibration period for the water and CHX to settle. The other set of simulations with a water molecule as the pull group used a pre-existing equilibrated membrane and a water molecule equidistant from either side of the membrane was chosen at random.

After equilibration, the pulled molecular group (either water or CHX) was brought into the membrane from its starting position in the water to the centre of the membrane, with a harmonic force constant of 1000 kJ mol^{-1} nm^{-1} and at a rate of 0.001 nm ps^{-1}. From this pulling simulation, 40 configurations were isolated, each with the z distance separating the centre of mass of the pulled molecule with the centre of the membrane, spaced 0.1 nm apart, ranging from 0 to 4.0 nm. Each of these configurations formed the starting point for a 100 ns simulation at 309 K, with a timestep of 10 fs and 2 fs for CG and AA simulations respectively. Each simulation held the test molecule in place with a harmonic restraining force on the centre of mass equal to 3000 kJ mol^{-1} nm^{-1} in the direction normal to the bilayer. PMFs were then calculated using the weighted histogram analysis method [15, 16] utilizing gromacs g_wham tool [17]. The first 25 ns of each trajectory were not included in the PMF calculation but rather used as further

equilibration time for each window. Therefore each PMF was calculated using a total of 3000 ns of simulation time (75 ns $\times$ 40 windows).

6.3 Results

6.3.1 CHX Insertion Energetics

To compare the free energy of CHX insertion into the bilayer between the CG and AA simulations, we used the WHAM method to calculate the PMF along the reaction coordinate of distance from the bilayer centre. These PMF plots were used to observe changes in the energy of insertion (ΔG_i), the energy of passing through the centre of the membrane, or flip-flop, (ΔG_{ff}), and the equilibrium distance from the bilayer centre corresponding to the location of lowest energy (Z_0). PMF plots generated using different force fields will generally result in different values for ΔG_i and ΔG_{ff} which can substantially disagree with each other [18–20]. This is an inherent problem arising from the different non-bonded parameters used by different force fields. Therefore, the reproduction of the absolute value of these energies was not held at as high of an importance as reproducing qualitative energy changes caused by altering the system. Furthermore, to our knowledge there is currently no experimentally value known for either ΔG_i or ΔG_{ff} of CHX in DMPC.

The first set of comparisons were made to assess differences between the 3 charged models of the CHX molecule in a pure DMPC membrane. Figure 6.2 shows the resulting PMF plots from each model, and Table 6.1 lists the corre-

sponding numerical values extracted. The lowest energy equilibrium location, Z_0, of the CHX molecule moves further from the membrane centre with increasing charge. For the AA simulations, the lowest energy position of CHX increased from 0.94 nm, to 1.14 nm, to 1.15 nm for the CHX^{0+}, CHX^{1+} and CHX^{2+} models respectively. Similarly, the CG models also found a well-matched, and increasing equilibrium position with increased charge with distances from the membrane center of 0.95 nm, 1.14 nm and 1.19 nm.

Both the CG and AA simulations qualitatively agree that increasing the charge also increases the energy barrier for CHX to pass from one leaflet to the other (ΔG_{ff}). The neutral CHX^{0+} has lowest ΔG_{ff} of the 3 models, being much smaller than ΔG_i , by a factor of 4. The neutral CHX^{0+} molecule is therefore much more likely to flip-flop from one side of the bilayer to the other rather than to leave the membrane entirely. Adding the +1 charge to the model raises ΔG_{ff} to be comparable, but slightly smaller, size to ΔG_i. The CHX^{2+} model has the highest ΔG_{ff}, notably larger than ΔG_i. Although the energy minimum location is still located inside the bilayer for the CHX^{2+} model, the driving force from the aqueous phase into the bilayer is greatly reduced.

Quantitatively, the CG simulations overestimate ΔG_i compared to AA simulations. The value of ΔG_i decreases with each increase in charge in the AA simulations with values of 43.34, 32.94 and 17.06 kJ/mol for the CHX^{0+}, CHX^{1+} and CHX^{2+} models respectively. The CG simulations however, did not change much at all, having values of 52.96, 58.24 and 45.25 kJ/mol for the CHX^{0+}, CHX^{1+} and CHX^{2+} models respectively. The higher ΔG_i values of the CG models could

consequently make the affinity of DMPC for CHX molecules artificially high.

The addition of CHX into DMPC has a structural effect on the membrane as discussed in greater detail in the following section. Therefore, a set of PMF plots were generated to observe the change in the energy of inserting a single CHX^{1+} molecule into a pure DMPC membrane as compared to one with 1:10 CHX^{1+}:DMPC concentration. Figure 6.2 shows that in both the AA and CG simulations, there is decrease in both ΔG_i and ΔG_{ff}. The 1:10 CHX^{1+}:DMPC membrane therefore has a reduced affinity to absorb more CHX molecules. The addition of CHX^{1+} molecules to the membrane also has the effect of lowering the barrier of another CHX^{1+} molecule crossing through DMPC. ΔG_i decreases by 9.62 kJ/mol, a 29% decrease in energy in the AA simulation, and by 11.19 kJ/mol, a 19% decrease in the CG simulation. The barrier ΔG_{ff} decreases by 5.15 kJ/mol, a 14% decrease in energy in the AA simulation, and by 22.89 kJ/mol, a 61% decrease in the CG simulation. Although, there is a clear effect on the energy of insertion and barrier at the centre of the membrane, the equilibrium position of CHX remains unchanged at 1.15 nm in the CG simulation and slightly closer to the membrane centre at 1.07 nm in the AA simulation.

Since CHX is putatively a membrane disrupting molecule, the permittivity of water was also investigated. A single water molecule was pulled through a pure DMPC membrane as well as the 1:10 CHX^{1+}:DMPC membrane. Figure 6.3 demonstrates very little alteration in the PMF plots for the insertion of water due to an increase in concentration of CHX for both of our AA and CG models. Therefore there is no substantial evidence from our simulations that a

CHX:DMPC ratio of 1:10 or lower will increase the permittivity of water.

6.3.2 Membrane Structural Changes

Figure 6.4 shows the change in key structural features of the DMPC membrane as a function of the CHX^{1+} concentration. The data is compared to AA simulations done in a previous study of CHX in DMPC at ratios of 0, 0.01, 0.03 and 0.1 CHX:DMPC (see Van Oosten et al. for simulation details [21]). A steady linear increase in the area per lipid is seen as the CHX^{1+} concentration is increased. Conversely, there is little change in the lipid thickness, showing no obvious trend. This suggests that the lipids are moving aside and the membrane expands as the CHX^{1+} molecule wedges itself in. The AA simulations used as a comparison also show a linear increase in the area per lipid and a constant thickness.

Two different types of the membrane thickness values were calculated to investigate the changes to the membrane thickness; the overall bilayer thickness, D_B, also known as Luzzati thickness in neutron scattering [22], and distance between lipid headgroups, D_{HH} commonly used in X-ray scattering [23, 24]. The CG membrane has a constant D_B thickness value of approximately 2.95 nm until 0.06 CHX:DMPC, where there is a sudden drop in the thickness to 2.82 nm. The D_{HH} thickness of the membrane is less steady than the D_B thickness, with values of approximately 1.13 nm with no upward or downward trend visible. The smaller thickness values of the CG simulation than that of the AA simulation arise from the particular atom-groupings of the DMPC model of the MARTINI force field, which groups four acyl-chain carbons into each virtual particle.

DMPC having 14 carbons can not evenly be divided by 4, and is therefore modelled using tails of 3 virtual particles, representing the same thickness as a lipid with length of 12 carbons (DLPC). The alternate choice to represent DMPC with 4 particles, which represents a 16 carbon length (DPPC), is no more accurate.

Since the MARTINI DMPC lipids consist of lipid tails represented by three particles, the order parameter along the acyl chain is ill defined by usual means. However, a second rank order parameter can be calculated using:

$$S_n = \frac{3}{2}\left\langle \cos^2(\theta) - \frac{1}{2} \right\rangle$$

where θ is the angle made between the bond between two particles and the bilayer normal. The second rank order parameter values are overall higher due to re-defining the torsion angles to be between groups of atoms and not between carbon atoms themselves, however, the similar characteristic of higher ordering at the headgroups and lower ordering in the tails, is still present. The upper panel in Figure 6.5 shows the CG second order parameter alongside the deuterium order parameter from AA simulations. With or without CHX^{1+}, both the CG and AA simulations show a similar ordering in the headgroups, and a decrease in order in the tails. Although the change in S_n with increasing CHX concentration is small, the lower panel of Figure 6.5 shows the maximum, minimum, and average values of S_n as a function of CHX concentration. A small and steady decrease in order with increasing CHX^{1+} concentration can be observed.

CHX molecules are mainly hydrophobic and as a result are seen to cluster in aqueous solutions and enter the membrane together. After entering the bi-

layer, they dissociate almost immediately. Figure 6.6A shows the distance in the bilayer-normal direction between the centre of the membrane and two clustered groups of CHX^{1+} molecules numbered 5 (aqua), 6 (blue), 7 (purple), 8 (red), and 9 (orange) from the first titration step. CHX^{1+} 5, 6, and 7 are seen to form a cluster of three, and CHX^{1+} 8 and 9 form a cluster of two, moving in tandem. The first cluster forms during the first 20 ns, and around 75 ns they all insert into the membrane simultaneously, while the second cluster are in the water from 20 ns to 340 ns before insertion. Figure 6.6B follows the minimum inter-CHX^{1+} distance to see how tightly they are clustered. For the first group, they are less than 0.5 nm of one another while in the water, but soon after they enter the membrane at 75 ns, they completely separate from each other. The same effect is seen with the second cluster, which separate immediately after insertion at 340 ns.

After the insertion of all 90 CHX molecules, there was an asymmetric distribution of 41 in the lower leaflet and 49 CHX molecules in the upper leaflet. Following an equilibrating period, the two-dimensional CHX^{1+}-CHX^{1+} radial distribution function in the plane of the bilayer was calculated and is shown in Figure 6.7A. Their radial distribution function rises gradually to 1 and does not show any nearest neighbour correlation. The CHX are spread evenly through the membrane, at the depth noted before. Figure 6.7B shows the two-dimensional radial distribution function for the DMPC phosphate groups. There is a nearest-neighbour and next-nearest-neighbour correlation distances of $\sim$0.9 nm and $\sim$1.45 nm, respectively, that remains unchanged with the addition of all the CHX^{1+}. This suggests that there is no differential lateral ordering of the lipids in the mem-

brane due to the addition CHX. Since the area per lipid has increased, the extra area is being taken up by the DMPC acyl tails, while the CHX prevents a thinning of the membrane.

The step-reduction seen in D_B at a CHX:DMPC ratio of 0.06 is also seen in a step-change in the distance from the centre of the membrane of the distribution of CHX^{1+}, shown in Figure 6.8 (top frame). The average CHX distance gradually increases from CHX:DMPC ratios of 0.01-0.06 from 1.00 nm to 1.03 nm, where there is again a sudden drop to 0.98 nm, followed by a nearly constant distance. It's difficult to isolate the nature of this structural change from CG data.

The diffusion rate of CHX as well as DMPC are compared as a function of CHX concentration in Figure 6.8 (middle and lower frames). The values for both CHX and DMPC are comparable to each other. The diffusion rates are fairly steady, with a small reduction in the diffusion rate of DMPC molecules. Clearly CHX is extraordinarily miscible with DMPC, structurally and dynamically.

The amount of time taken for each of the CHX molecules to insert itself into the membrane from the beginning of each titration is provided in Table 6.2. The CHX are numbered by the order in which they insert into the membrane. There is general lengthening in the amount of time taken for each molecule, or group of molecules, to insert. This was expected as the ΔG_i was seen to decrease while a slight $\sim$ 2 kJ/mol barrier emerged in the PMF of CHX in a 1:10 CHX:DMPC as compared to the pure DMPC membrane. Directly analyzing the insertion times of each molecule is problematic due to the aggregation of the molecules in the water. Table 6.2 shows that during each of the titration steps, there are groups of

CHX molecules which aggregate in the water before inserting into the membrane at the same time. It is also noticeable that the larger the group of CHX, the longer it took for that group to be inserted. Therefore it is possible that the insertion time is a function of both the CHX concentration in the membrane and the cluster size of CHX trying to insert into the membrane. To deconvolve these two variables, the aggregation would have to be controlled to observe the increase in insertion time for an aggregate of a set size. Our experiment does not have the proper statistical confidence due to the simulations having aggregates of differing size from 1 to 7 CHX molecules, which therefore does not give enough evidence for any one aggregate size.

6.3.3 Calorimetry Method Tests

The computational calorimetry technique proposed in this study is not a robust method for calculating the correct temperature or enthalpies of the main transition due to limitations of current force fields as well as the molecular dynamics approach. One of the limitations in the creation of the MARTINI force field was in that it was parameterized to reproduce the same internal energy values with a model consisting of a reduced number of degrees of freedom. This has lead to the incorrect reproduction of temperature with the use of this force field [25]. Calculating the enthalpy of the transition has proven to be equally challenging. The exact enthalpy of the phase transition was not calculated due to difficulties in determining the exact time for the transition to occur. Also, only large and fast transition created enough perturbations in the system energy to be measur-

able. We therefore investigate the effects of simulation time at each temperature as well as comparing energy fluctuations calculated from "quick" transitions of the CG membrane and "slow" transitions of an AA membrane.

We first investigate the effects that altering the length of the simulations at each temperature have on the phase transition. Figure 6.10 A) shows the energy vs time profile of the cooling using simulation times of 25, 50 and 100 ns per temperature. Firstly, we note that the transition does not always happen at the same temperature, suggesting a degree of error in the temperature of the transition of $\pm$ 1 temperature window. This is likely due to the statistical nature of the small system, where a nucleation site is needed, with the probability of nucleation increasing with decreased temperature. Secondly we note that the drop in energy at the transition takes approximately 30 ns. The 25 ns temperature windows are not long enough to capture the transition and thus, the transition is spread over a large range of windows as the energy decreases as a decaying exponential. The 50 and 100 ns per temperature windows are long enough and create a sigmoidal decrease in the system energy, contained in a single window. Figure 6.10 B) shows the area per lipid as a function of temperature for each of these three time lengths. For the 25 ns windows, we see the transition from high to low area per lipid takes approximately 5 simulation windows before leveling off at 48 nm^2. Similarly we see it takes 2 windows at 50 ns windows and one point is not quite sufficient enough for 100 ns windows. This tells us that although the main transition takes approximately 30 ns, all 3 time steps took 100-125 ns of equilibration for the system to settle into steady area per lipid values corresponding to the gel

phase.

Secondly we test the ability for the AA Slipids force field [11–13] to reproduce the sudden phase change exhibited by the CG MARTINI force field. In the CG simulations we observe that at the phase transition, all of the lipids act as one cooperative group transitioning from liquid to gel phase very quickly. This can be observed as a sharp increase in the average second rank order parameter. Figure 6.11 B) shows a distinct increase in the second rank order parameter as the system changes from liquid to gel phase at 10°C. The AA simulations using the Slipids force field however does not show an abrupt change from liquid to gel. Instead, we observe a low and steady change in the order parameter as the lipid tails become more ordered at lower temperatures, with the change occurring through the temperature range between 16°C and -10°C. This effect can also be observed in the calculated specific heat of the system in Figure 6.11 A). Since the CG simulation changes phase rapidly, the large change in the system energy is easily measures and created a sharp peak in the specific heat curve. However, since the AA simulation produces a much more gradual transition, there is no abrupt change in the system energy and thus, no peak in the specific heat.

6.3.4 Computational Calorimetry

The main transition temperature (T_m) of the DMPC reference simulation occurs at 10 °C. In Figure 6.12, the transition temperature shifts to lower values with increasing CHX concentrations. The trend at which the transition temperature lowers seems to have two distinct regions. Between CHX concentrations of 0 %

to 5 %, we see a linear decrease in T_m of approximately 1°C per step increase in CHX concentration. This trend is amplified at concentrations beyond 5 % where we see a lowering of T_m of approximately 4 °C. The height of each peak also decreases with increasing CHX concentrations from 0 % to 5 %. At concentrations larger than 5 % the peak begins to span more an one temperature simulation and shrinks in size, comparable to background noise.

The effects of adding cholesterol to the DMPC membrane are opposite to that of CHX with T_m increasing with an increase in cholesterol concentration. Figure 6.13 demonstrates that an addition of 1 % cholesterol causes T_m to shift up 2.5°C to 12.5°C. T_m then remains at 12.5°C until 10 % cholesterol concentrations where the temperature increases to 13°C. The peak height is at its largest at 1 % cholesterol concentration, however, increasing the amount of cholesterol above 1 % only decreases the peak height.

The addition of CHX into the cholesterol membranes has resulted in non-trivial results as seen in Figure 6.14. With 1 % CHX concentration the effects of cholesterol concentrations are dampened with the exception of 5 % cholesterol in which T_m is higher than the same membrane without CHX. With 5 % CHX concentrations, the addition of cholesterol has the opposing effect on the membrane, where increasing the cholesterol concentration decreases T_m.

6.4 Discussion

CHX is an effective antibacterial agent, shown to attack, disrupt and cause cell lysis [5, 6, 26, 27]. We therefore decided to observe CHX in a model DMPC membrane in which we have prior experimental data [28] where the presence of smectic-multilayers at concentrations as high as 1:3 CHX:DMPC indicate the structural integrity of the bilayer remains intact. Our hypothesis was such that we should observe some sign of membrane instability at concentrations approaching that of the minimum inhibitory concentration.

Assuming a typical rod-shaped *P. aeruginosa* cell to be a cylinder of length 2.5 μm and radius 0.5 μm, with its surface completely composed of lipopolysaccharide (LPS) molecules of area per lipid 1.37 nm^2 [29], there are roughly 1.4×10^6 LPS covering the surface. This becomes 3×10^6 if such bacteria were covered in DMPC at 0.6 nm^2 area per lipid. The actual number lies between theses values since the outer membrane is only composed of approximately 75% LPS molecules with additional, smaller phospholipids [30].

Studies to establish MIC values start with a biofilm of as much as 10^{12} colony forming units (cfu)/L, and if we assume each cfu is established by one cell, then LPS has a concentration in the biofilm of $\sim 2.3 \times 10^{-6}$ mol/L ($\sim 5 \times 10^{-6}$ mol/L for DMPC only) [31]. This will form a lower limit of lipid concentration, as colonies are more often established by groups of cells. We also take the MIC of of CHX to be 0.5 mg/L, which of course is species dependant, and the molecular mass to be 505 g/mol [5, 6, 27]. Thus the concentration of CHX at MIC to be 1×10^{-6} mol/L, and thus the lipid:CHX ratio at the MIC is roughly in the range

of $2 \sim 8 : 1$, assuming all the CHX is taken up by the biofilm.

Even at concentrations approaching that of the MIC, we see no noticeable disruption of the DMPC model membrane, in agreement with our earlier experimental results. The small changes in membrane thickness, and little change in membrane fluidity and order, all point to a cell membrane that remains functionally intact. Unless there is some unidentified target of CHX that is cell membrane bound, there is no sign that even charged CHX would pass through the cell membrane to an interior compartment. We find it unlikely the interaction of CHX with LPS would change these results, and should CHX pass through the outer membrane of gram negative bacteria such as *P. aeruginosa*, it would certainly be easily incorporated in the inner membrane as shown here. One further possibility is that the observed lytic properties of CHX simply cannot be reproduced easily with a simplistic model membrane such as DMPC.

Lin et al. [32] have studied the fusion of micelles of differing sizes with the umbrella sampling technique in order to better study the fusion of micelles of different size. Since we also note a large effect of aggregation of CHX molecules, a combination of these two techniques would be a useful extension to this study. This would include finding the most energetically favourable aggregate size and inserting it into a model membrane to observe the energy barrier for the aggregate to insert. In our study we see an increase in the amount of time needed for insertion of a large aggregate size, but we lack the statistical accuracy to make any valuable conclusions on the matter. Another extension for this study would be to test the energy barrier of these aggregates in membranes of different lipid

compositions, that better mimic both a mammalian and bacterial cell membrane, which may lead to insight to why CHX is effective at killing bacteria, however is not as effective in killing mammalian cells.

6.5 Conclusion

In this paper, we presented a novel use for our extension to the MARTINI force field for the small molecule chlorhexidine (CHX). The computational savings of a CG model was vital to this study, which contains a total 47.5 us of production simulation time (36 us of umbrella sampling and 11.5 us of simulated titration), on a system of 900 lipids and up to 90 additional CHX molecules.

We used the CHX^{1+} model to simulate a titration adding 1% concentration of CHX into a DMPC membrane ten times so that we had 11 equilibrated systems with CHX concentrations ranging from 0 to 1:10. With these systems, we were able to observe the concentration effects of CHX on the DMPC membrane. The DMPC membrane was easily able to absorb all the CHX molecules, linearly increasing the area per lipid while the thickness remained constant, with the exception of a sudden drop at 6% concentration. Although 1:10 concentration of CHX was not enough to saturate the membrane, a decrease in the affinity between the drug and lipid was observed, as well as a lowered energy barrier for additional molecules to penetrate through the membrane. No internal ordering was found for either the CHX or DMPC molecules. The CHX molecules would aggregate in the aqueous solution, and separate from each other once inserted

into the membrane.

We then performed a controlled cooling of these DMPC:CHX membranes created by this simulated titration to recreate a computational calorimetry experiment. From this we observed that T_m of DMPC decreased with the addition of CHX and increased with the addition of cholesterol. The resulting effect of the combination of both CHX and cholesterol were however, nontrivial. Low concentration of CHX seemed to dampen the ability of cholesterol to raise T_m, whereas high concentrations of CHX completely reversed the effects of cholesterol causing a lowering of T_m.

6.6 Acknowledgements

This work was supported by the Natural Sciences and Engineering Research Council of Canada, the Shared Hierarchical Academic Research Computing Network (SHARCNET: www.sharcnet.ca), and Compute/Calcul Canada.

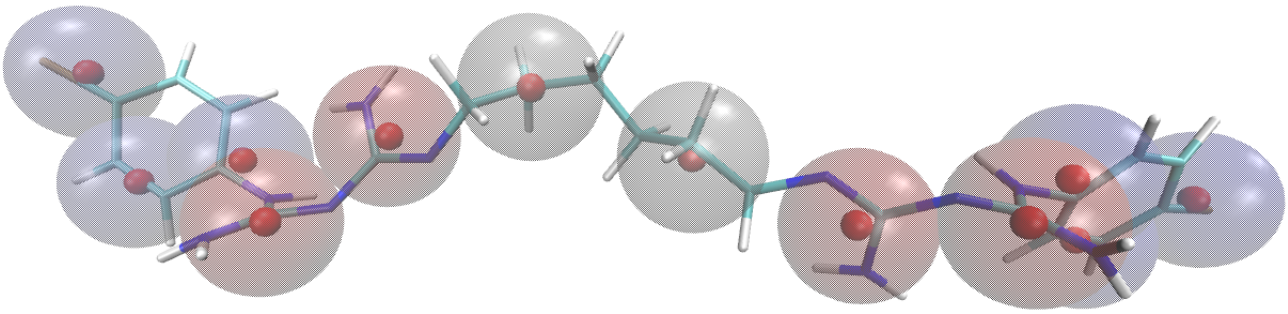

Figure 6.1: Simulation snapshot of AA CHX molecule with virtual particles based on the center of mass (red dot) of the atoms they represent. The molecule sections are coloured with CPL in blue tint, BGU in red tint and HEX in grey tint.

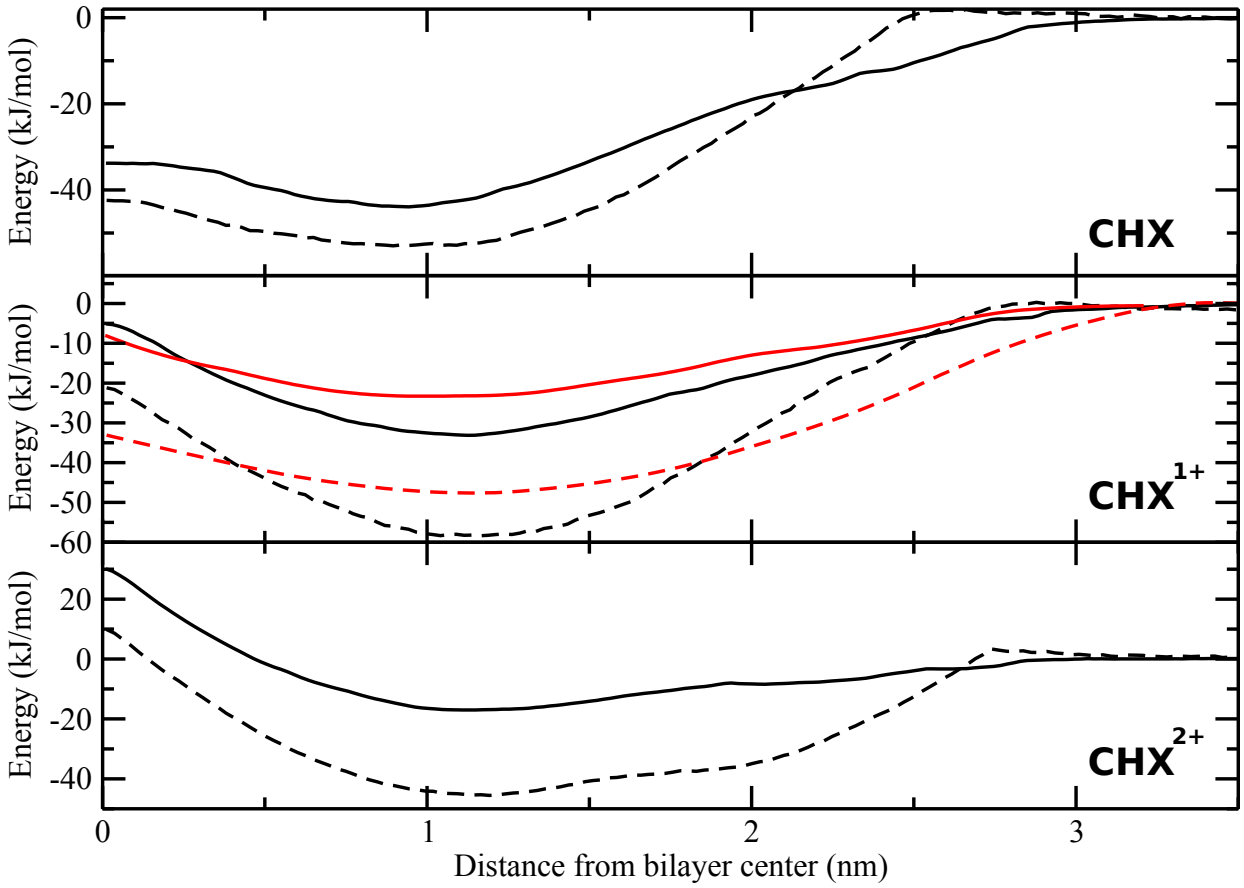

Figure 6.2: PMF of AA (solid lines) and CG (dashed lines) for each of the 3 CHX models: neutral CHX^{0+} (top), CHX^{1+} (middle), CHX^{2+} (bottom) in a pure DMPC membrane (black) as well as in a 1:10 CHX^{1+}:DMPC membrane (red) exclusively for CHX^{1+} in the central frame.

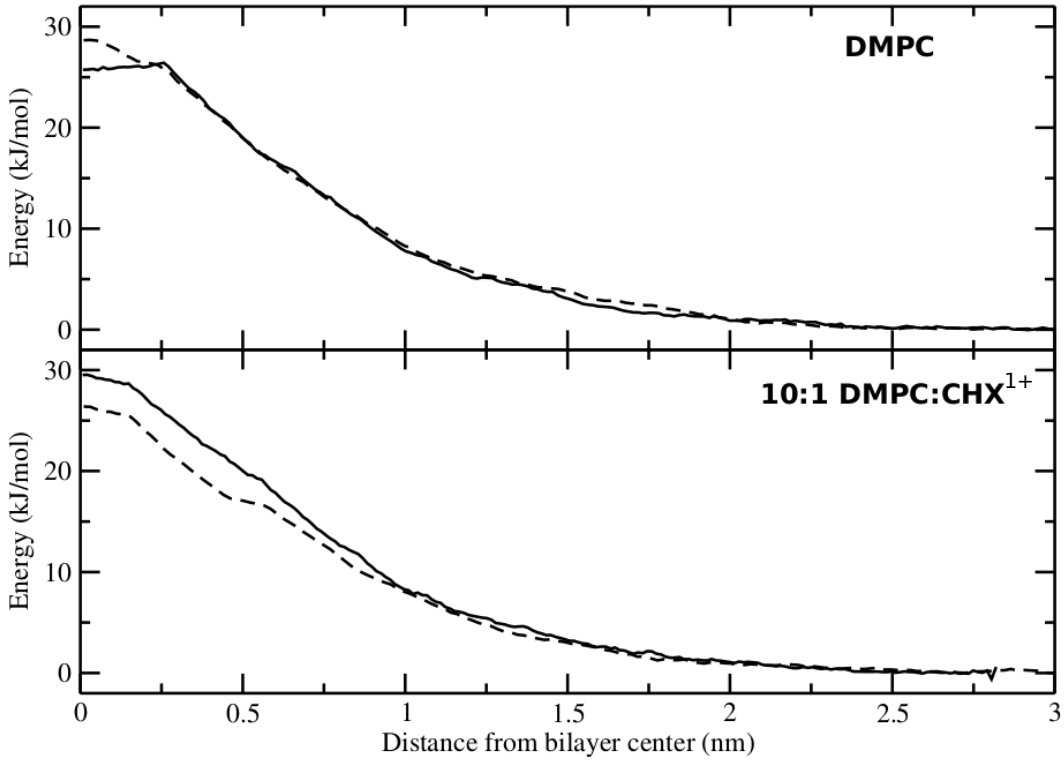

Figure 6.3: PMF of one water molecule (solid line AA and dashed line CG) into a pure DMPC membrane (top frame) and 1:10 CHX^{1+}:DMPC membrane (bottom frame).

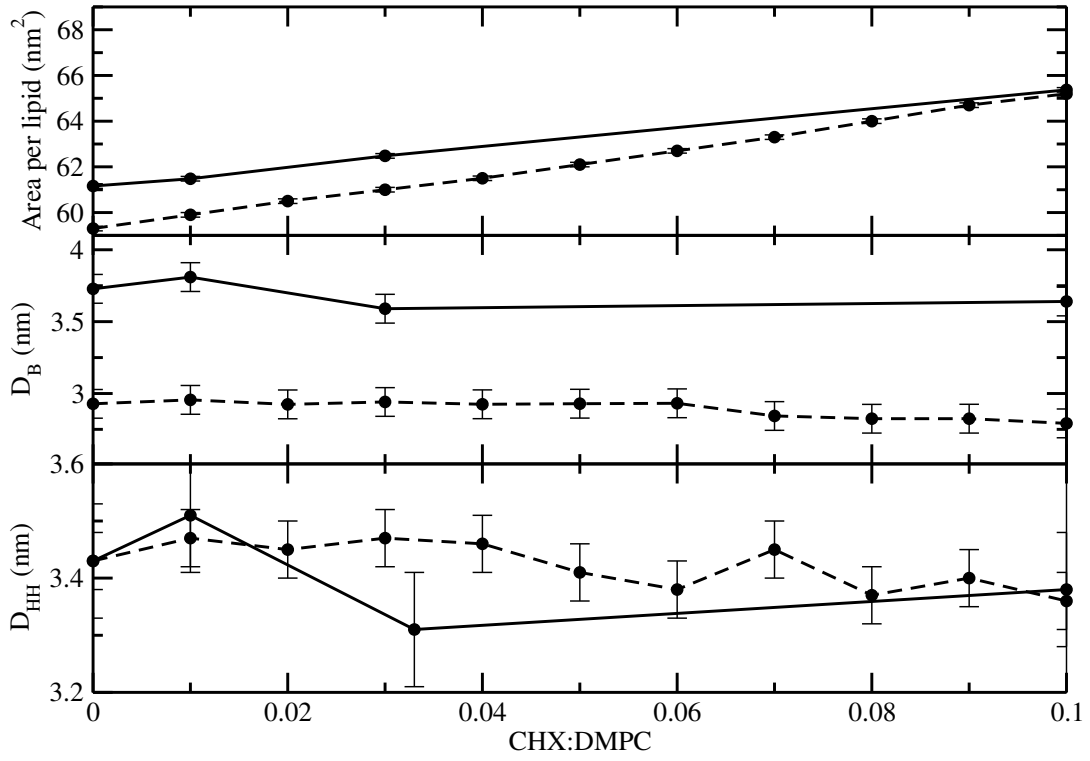

Figure 6.4: Spatial properties for AA (solid lines) and CG (dashed lines) per CHX concentration. Area per lipid (top), total membrane thickness D_B (middle) and membrane backbone to backbone thickness D_{HH} (bottom)

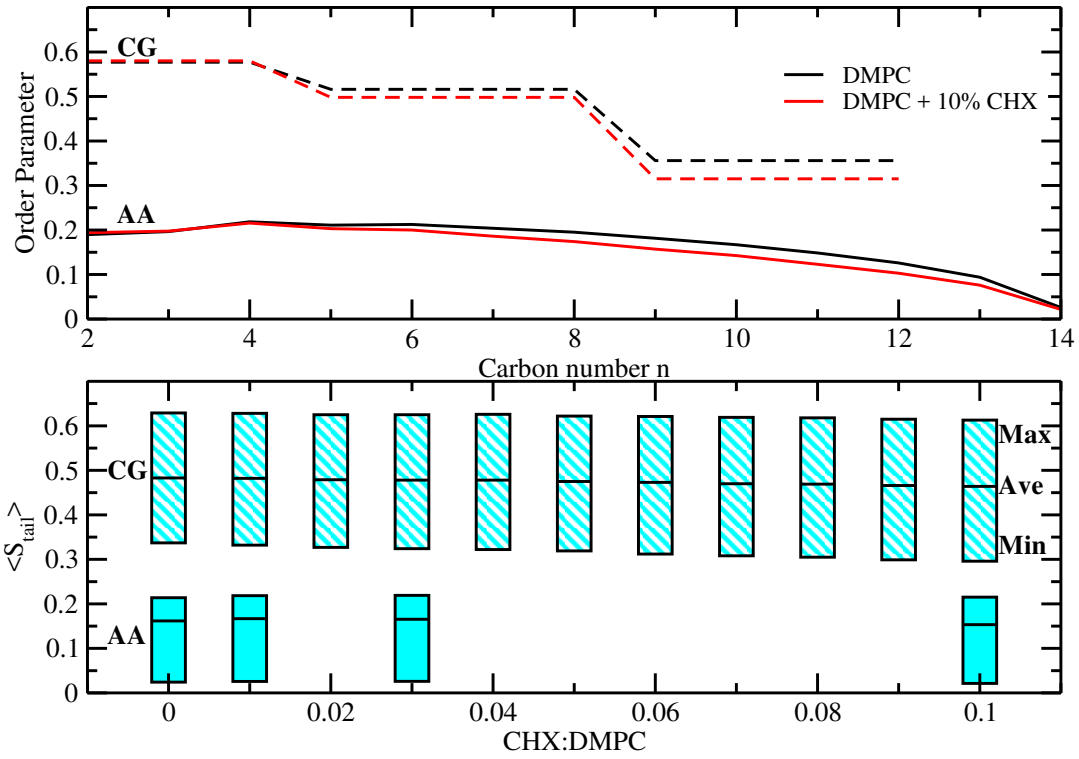

Figure 6.5: Top: deuterium order parameter averaged over both lipid tails for the AA simulation of the pure DMPC membrane (solid black) and the 1:10 CHX^{1+}:DMPC membrane(solid red) as well as the second rank order parameter calculated from the angles of the bond between particles in the CG simulations of the pure DMPC membrane (dashed black) and the 1:10 CHX^{1+}:DMPC membrane (dashed red). Bottom: Boxplot representing the maximum, minimum and average order parameter value at each of the CHX concentrations for the AA simulations (solid colour) and CG simulations (hatched colour).

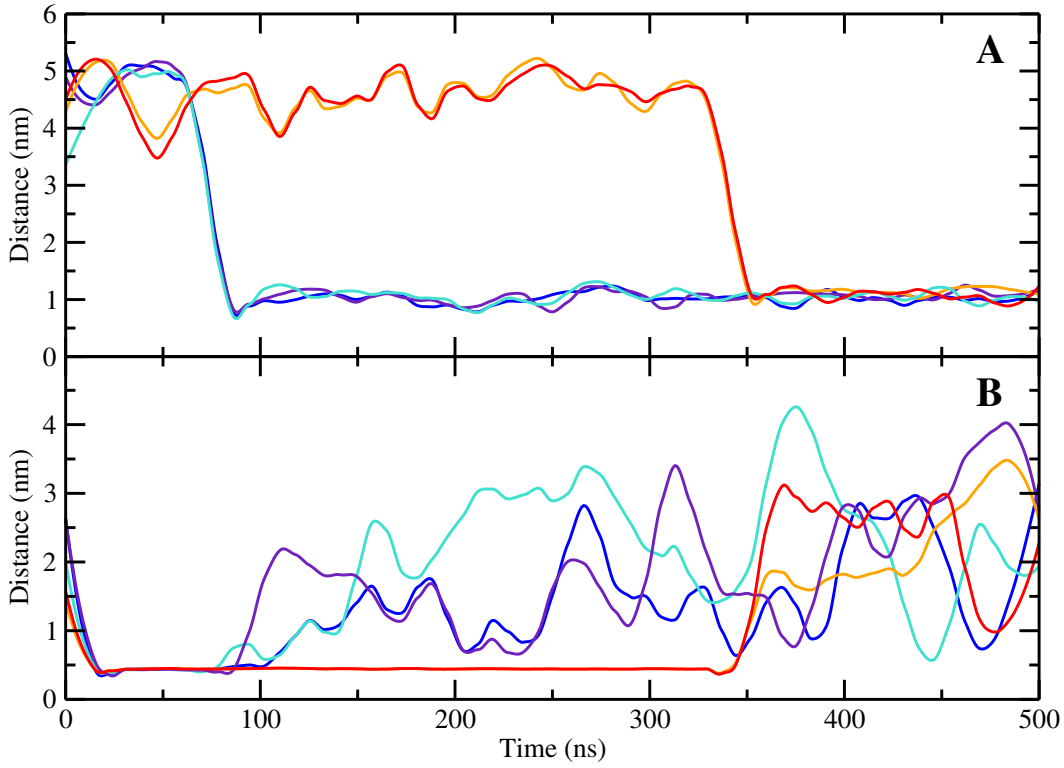

Figure 6.6: Time evolution of the position of five CHX^{1+} from the initial titration. The distance from the CHX^{1+} centre of mass to the bilayer center (top), and minimum distance between that CHX^{1+} and another (bottom).

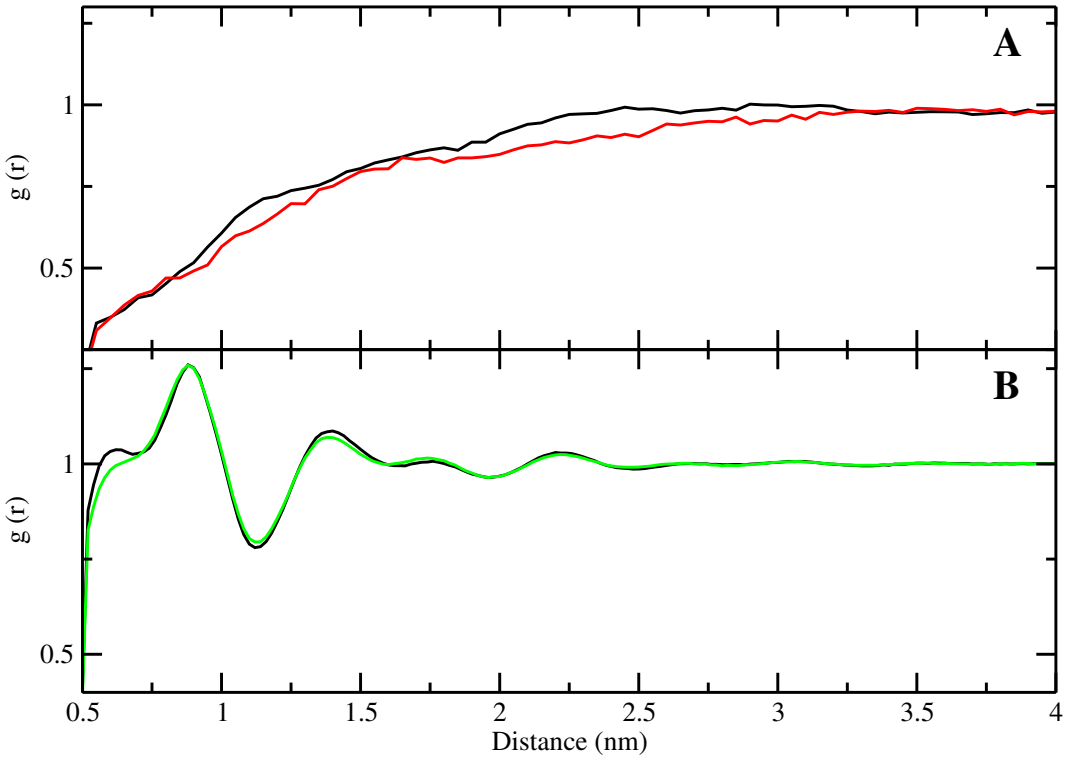

Figure 6.7: (A) 2D CHX^{1+}-CHX^{1+} radial distribution function for the 11:10 CHX^{1+}:DMPC simulation in the top leaflet (black) and bottom leaflet (red). (B) 2D DMPC P-P radial distribution of pure DMPC membrane (black) and 1:10 CHX^{1+}:DMPC membrane (green).

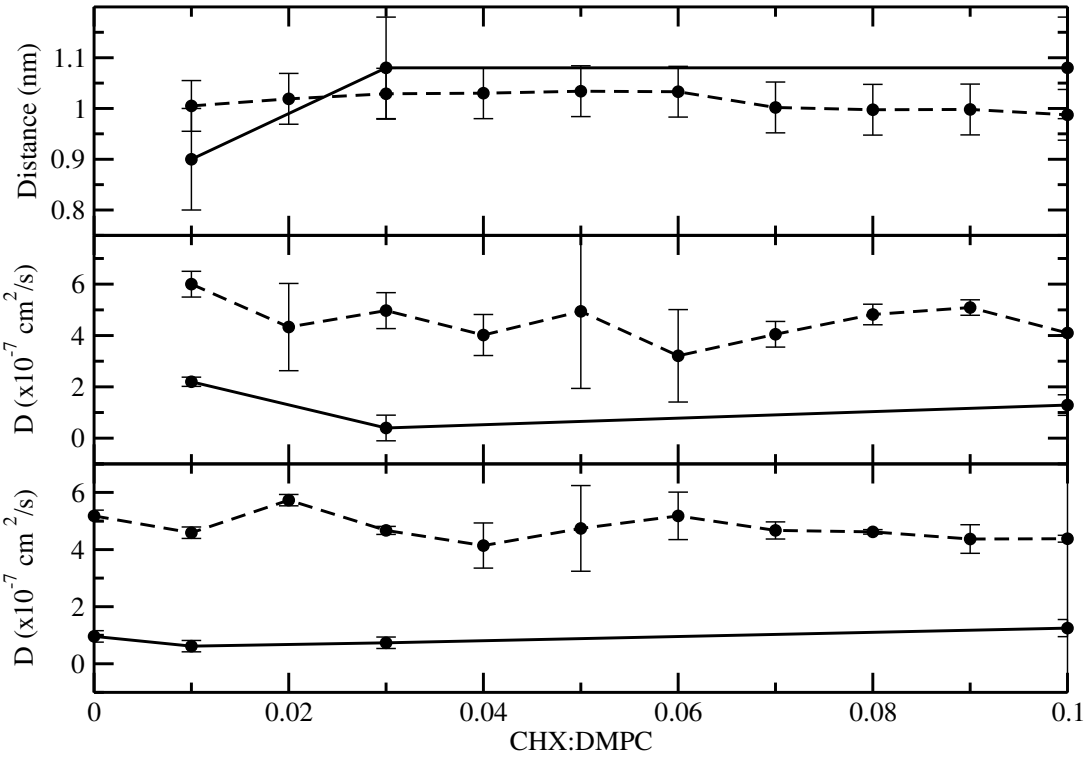

Figure 6.8: System properties for AA (solid lines) and CG (dashed lines) per CHX concentration. CHX distribution distance from bilayer center (top), CHX lateral diffusion rate (middle) and DMPC lateral diffusion rate (bottom)

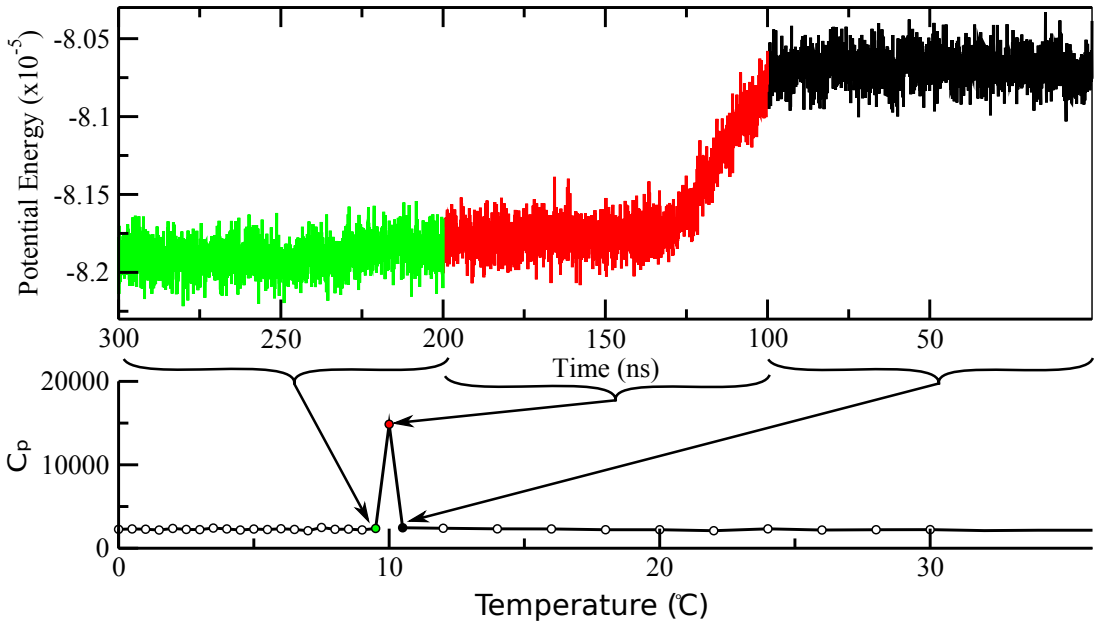

Figure 6.9: Top - energy vs time for pure DMPC at temperatures of 10.5°C (black), 10°C (red) and 9.5°C (green), as it is cooled through the main transition from liquid to gel. Bottom - specific heat vs temperature. Arrows indicate the three points of the graph which are calculated from the three energy sections shown above.

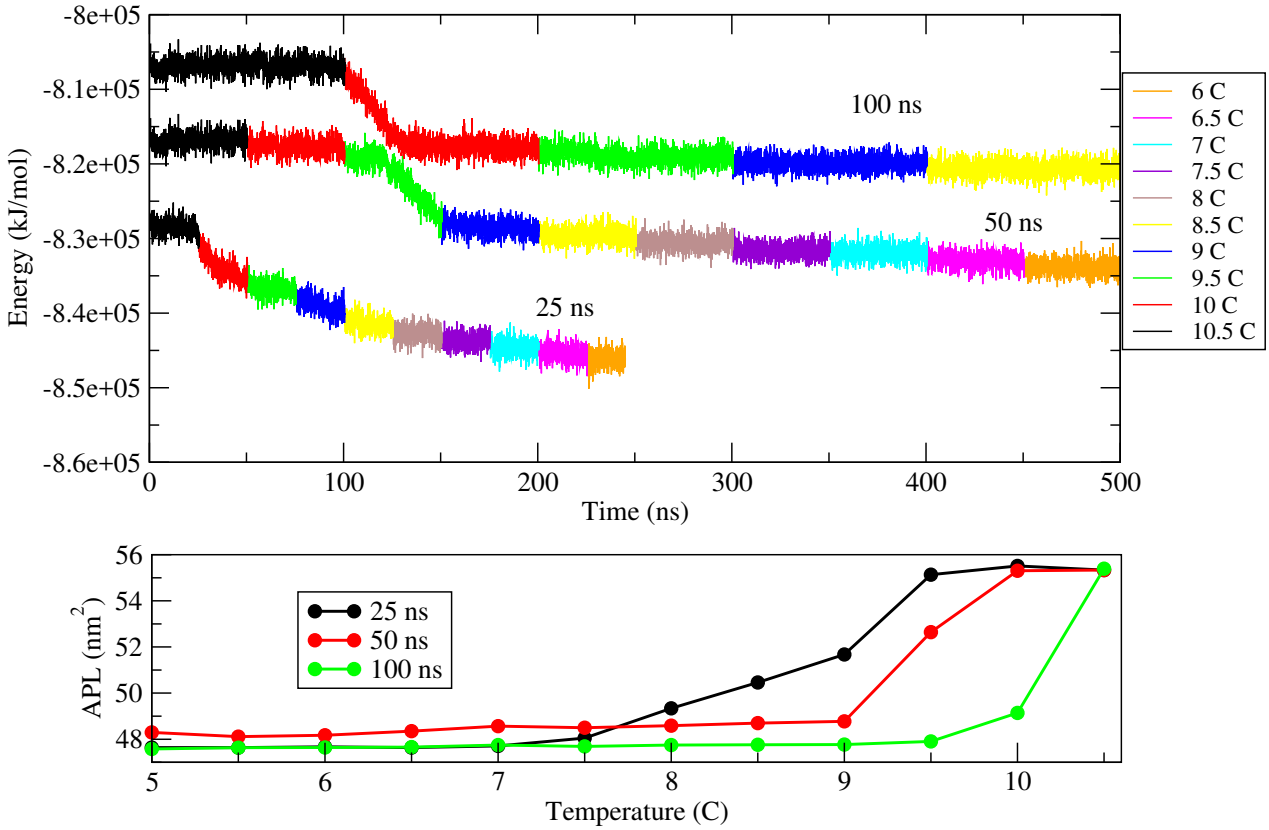

Figure 6.10: Top - Energy vs time for different simulation time lengths for a constant temperature window of 25, 50 and 100 ns (shifted vertically for clarity). Each Temperature is coloured differently to enhance the clarity of the location of the changes in temperature. Bottom - The area per lipid for the 25 (black), 50 (red) and 100 ns (green) temperature windows.

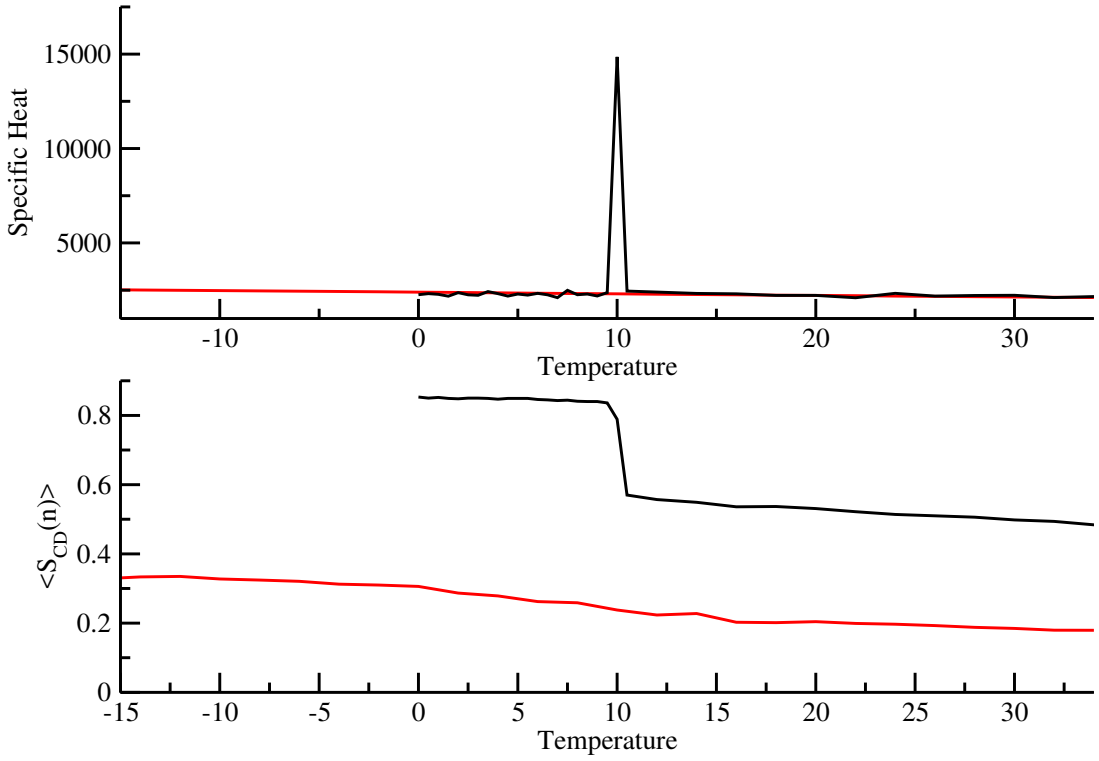

Figure 6.11: Top - Specific heat of CG(black) and AA(red) simulations. Bottom - average deuterium order parameter for AA (red) and average order parameter between CG particle bonds(black).

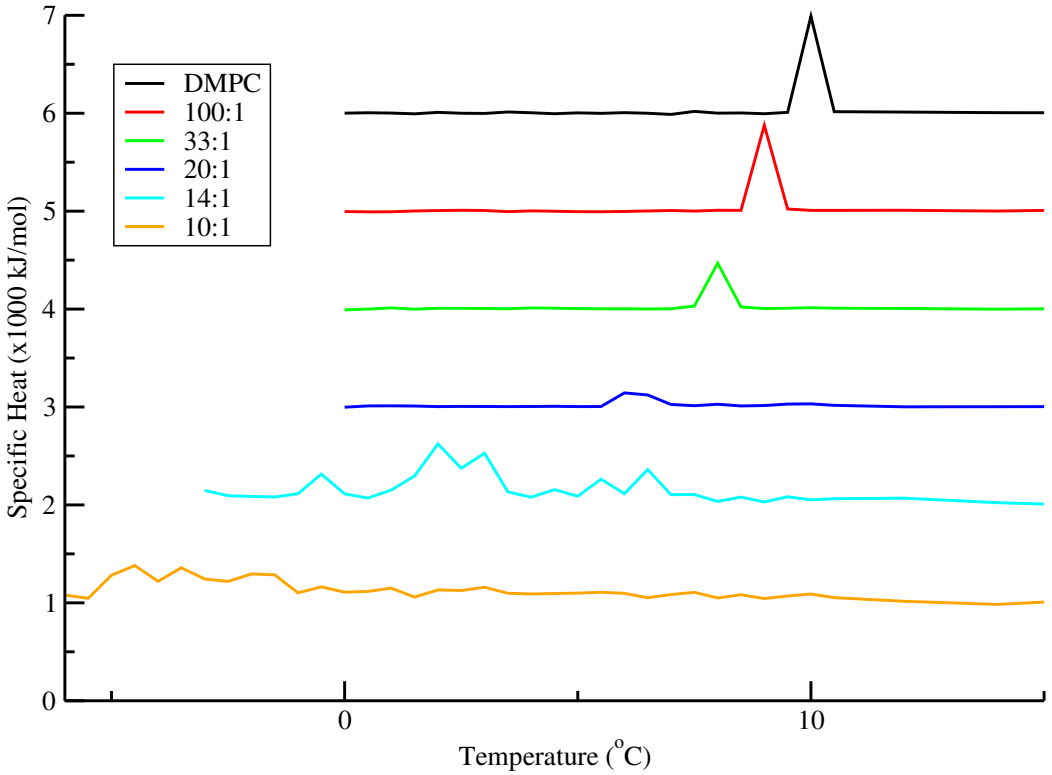

Figure 6.12: Specific heat traces for DMPC and 0 to 10 % CHX concentration. 7% and 10% are scales by a factor of 5 for clarity, all traces are shifted vertically for visual clarity.

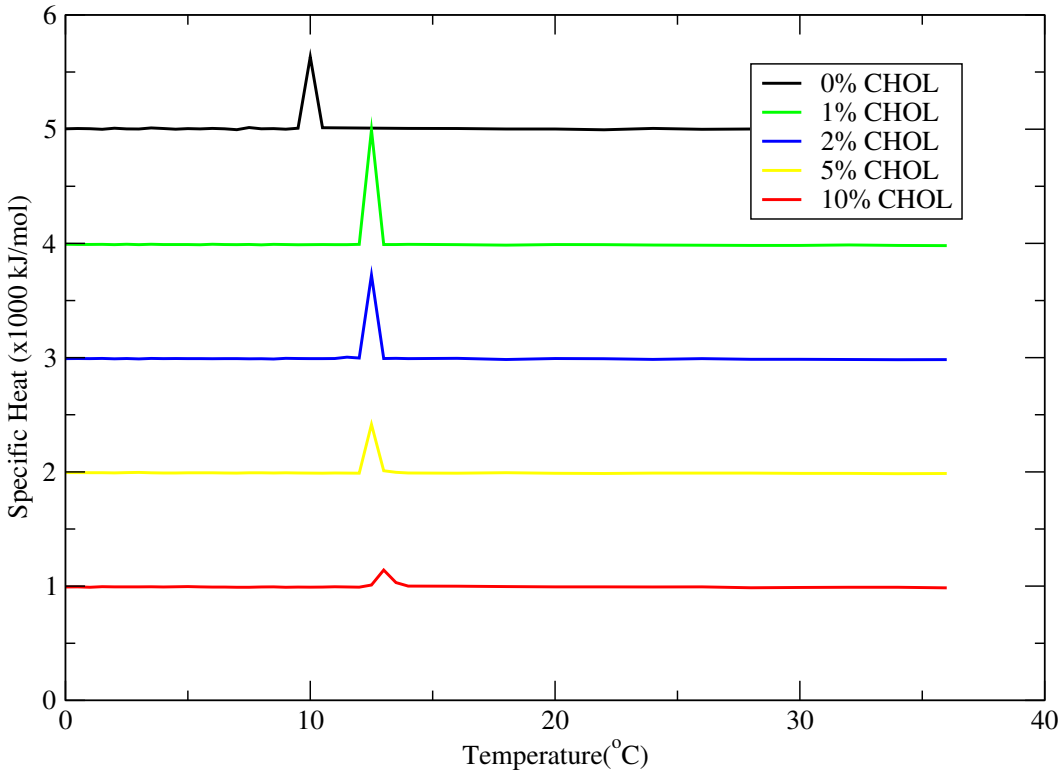

Figure 6.13: Specific heat traces for DMPC and 0 to 10 % cholesterol concentration. All traces are shifted vertically for visual clarity.

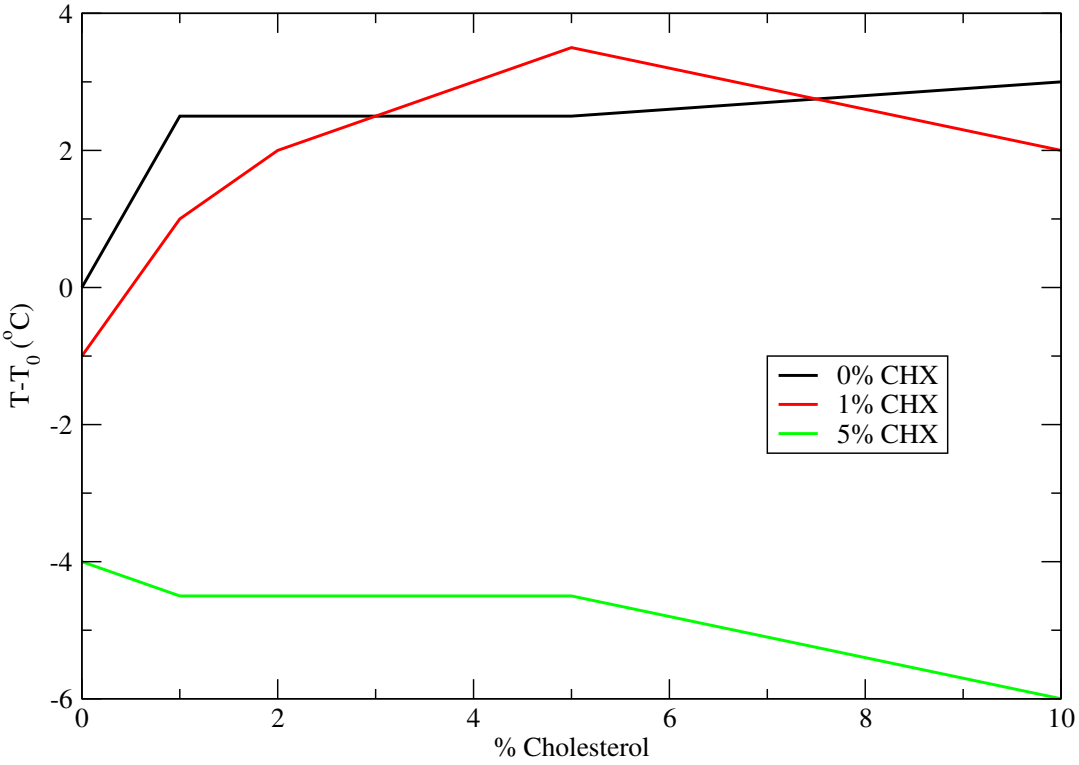

Figure 6.14: Main transition temperature changes in respect to a pure DMPC membrane (T-T_m) for membranes of various CHX and cholesterol concentrations

Table 6.1: PMF calculated values for the energy of insertion (ΔG_i), energy barrier to cross the membrane centre (ΔG_{ff}), and the equilibrium distance from the membrane centre (Z_0)

Pulled Molecule	Membrane	ΔG_i (kJ/mol)	ΔG_{ff} (kJ/mol)	Z_0 (nm)
AA CHX	DMPC	43.34	10.43	0.94
AA CHX^{1+}	DMPC	32.94	36.84	1.14
AA CHX^{2+}	DMPC	17.06	48.28	1.15
CG CHX	DMPC	52.96	11.54	0.95
CG CHX^{1+}	DMPC	58.24	37.42	1.14
CG CHX^{2+}	DMPC	45.25	55.72	1.19
AA CHX^{1+}	1:10 CHX^{1+}:DMPC	23.32	31.69	1.07
CG CHX^{1+}	1:10 CHX^{1+}:DMPC	47.05	14.53	1.15
AA Water	DMPC	-	25.72	∞
AA Water	1:10 CHX^{1+}:DMPC	-	29.48	∞
CG Water	DMPC	-	28.6	∞
CG Water	1:10 CHX^{1+}:DMPC	-	24.61	∞

Table 6.2: Time (in ns) for each CHX molecule to insert into the membrane, listed by titration number(T-1 to T-10). CHX are numbered according to the order in which they inserted.

	T-1	T-2	T-3	T-4	T-5	T-6	T-7	T-8	T-9	T-10
CHX 1	2	6	5	5	11	3	9	86	10	12
CHX 2	26	13	35	10	41	9	13	86	997	16
CHX 3	26	588	35	190	41	18	16	86	1010	16
CHX 4	67	588	35	387	41	30	22	3100	1010	42
CHX 5	75	588	35	387	41	50	597	3110	1010	640
CHX 6	75	588	394	387	43	840	597	3120	1010	1020
CHX 7	75	588	394	387	46	840	597	3120	1010	1020
CHX 8	342	588	394	387	364	840	597	3120	1010	1020
CHX 9	342	588	394	387	364	840	597	3120	1010	1020

References

1. Denys, A, Machlanski, T, Bialek, J & Mrozicki, S. Relationships between chemical structure and antiviral activity of some biguanide derivatives. *Zentralbl Bakteriol Orig B* **164,** 85–89 (2004).

2. Tanzer, J. M., Slee, A. M. & Kamay, B. A. Structural requirements of guanide, biguanide, and bisbiguanide agents for antiplaque activity. *Antimicrobial Agents And Chemotherapy* **12,** 721–729 (1977).

3. Campbell, R. K., White, J. & Saulie, B. A. Metformin: a new oral biguanide. *Clinical Therapeutics* **18,** 360–371 (1996).

4. Uchiyama, H. *et al.* Quinine-resistant Severe Falciparum Malaria Effectively Treated with Atovaquone and Proguanil Hydrochloride Combination Therapy. *Internal Medicine* **43,** 624–627 (2004).

5. Thomas, L, Russell, A. D. & Maillard, J. Antimicrobial activity of chlorhexidine diacetate and benzalkonium chloride against Pseudomonas aeruginosa and its response to biocide residues, 533–543 (2005).

6. Solmaz, G. & Korachi, M. nhibition and Disruption Properties of Chlorhexidine Gluconate on Single and Multispecies Oral Biofilms. *Jundishapur Journal of Microbiology* **6,** 61–66 (2012).

7. Blackburn, R. S., Harvey, A., Kettle, L. L., Payne, J. D. & Russell, S. J. Sorption of Poly(hexamethylenebiguanide) on Cellulose: Mechanism of Binding and Molecular Recognition. *Langmuir* **22,** 5636–5644 (2006).

8. Blackburn, R. S. *et al.* Sorption of Chlorhexidine on Cellulose: Mechanism of Binding and Molecular Recognition. *Journal of Physical Chemistry B* **111,** 8775–8784 (2007).

9. Wassenaar, T., Ingolfsson, H., Bockmann, R., Tieleman, P. & Marrink, S. Computational Lipidomics with insane: A Versatile Tool for Generating Custom Membranes for Molecular Simulations. *Journal of Chemical Theory and Computation* **11,** 2144–2155 (2015).

10. Bekker, H *et al.* in *Physics Computing '92* (eds DeGroot, R. & Nadrchal, J) 252–256 (World Scientific Publishing, 1993). ISBN: 981-02-1245-3.

11. Jambeck, J. & Lyubartsev, A. Derivation and Systematic Validation of a Refined All-Atom Force Field for Phosphatidylcholine Lipids. *The Journal of Physical Chemistry B* **116,** 3164–3179 (10 2012).

12. Jambeck, J. & Lyubartsev, A. An Extension and Further Validation of an All-Atomistic Force Field for Biological Membranes. *Journal of Chemical Theory and Computation* **8,** 2938–2948 (2012).

13. Jambeck, J. & Lyubartsev, A. Another Piece of the Membrane Puzzle: Extending Slipids Further. *Journal of Chemical Theory and Computation* **9,** 774–784 (2013).

14. Jo, S., Kim, T., Iyer, V. & Im, W. CHARMM-GUI: A web-based graphical user interface for CHARMM. *Journal of Computational Chemistry* **29,** 1859–1865 (2008).

15. Kumar, S., Rosenberg, J. M., Bouzida, D., Swendsen, R. H. & Kollman, P. A. The weighted histogram analysis method for free-energy calculations on biomolecules. I. The method. *Journal of Computational Chemistry* **13,** 1011–1021 (1992).

16. Roux, B & Physics, C. The calculation of the potential of mean force using computer simulations. *Computer Physics Communications* **91,** 275–282 (1995).

17. Hub, J., de Groot, B. & van der Spoel, D. g_wham-A Free Weighted Histogram Analysis Implementation Including Robust Error and Autocorrelation Estimates. *Journal of Chemical Theory and Computation* **6,** 3713–3720 (2010).

18. Marrink, S. J., Risselada, H. J., Yefimov, S., Tieleman, D. P. & Vries, A. H. D. The MARTINI Force Field : Coarse Grained Model for Biomolecular Simulations. **111,** 7812–7824 (2007).

19. Monticelli, L. *et al.* The MARTINI Coarse-Grained Force Field: Extension to Proteins. *Journal of Chemical Theory and Computation* **4,** 819–834 (5 2008).

20. Paloncyova, M. *et al.* Benchmarking of Force Fields for Molecule-Membrane Interactions. *Journal of Chemical Theory and Computation* **10,** 4143–4151 (2014).

21. Van Oosten, B. *et al.* Small molecule interaction with lipid bilayers: A molecular dynamics study of chlorhexidine. *Journal of Molecular Graphics and Modelling* **48,** 96–104 (2014).

22. Luzzati, V & Husson, F. THE STRUCTURE OF THE LIQUID-CRYSTALLINE PHASES OF LIPID-WATER SYSTEMS. *The Journal of Cell Biology* **12,** 207–219 (1962).

23. Kučerka, N., Nieh, M & Katsaras, J. Fluid phase lipid areas and bilayer thicknesses of commonly used phosphatidylcholines as a function of temperature. *Biochimica et Biophysica Acta* **1808,** 2761–2771 (2011).

24. Kucerka, N. *et al.* Molecular Structures of Fluid Phosphatidylethanolamine Bilayers Obtained from Simulation-to-Experiment Comparisons and Experimental Scattering Density Profiles. *Journal of Physical Chemistry B* **119,** 1947–1956 (2014).

25. Marrink, S., Risselada, J., Yefimov, S., Tieleman, P. & de Vries, A. The MARTINI Force Field: Coarse Grained Model for Biomolecular Simulations. *The Journal of Physical Chemistry B* **111,** 7812–7824 (27 2007).

26. Athanassiadis, B, Abbott, P. & Walsh, L. *The use of calcium hydroxide, antibiotics and biocides as antimicrobial medicaments in endodontics* 2007.

27. Adam P. Fraise, S. S. Jean-Yves Maillard. *Principles and Practices od Disinfection Preservation & Sterilization* 4th (Blackwell Publishing Ltd, 2004).

28. Komljenović, I., Marquardt, D., Harroun, T. A. & Sternin, E. Location of chlorhexidine in DMPC model membranes: a neutron diffraction study. *Chemistry and Physics of Lipids* **163,** 480–487 (2010).

29. Kirschner, K. N., Lins, R. D., Maass, A. & Soares, T. A. A glycam-based force field for simulations of lipopolysaccharide membranes: Parametrization and validation. *Journal of Chemical Theory and Computation* **8,** 4719–4731 (2012).

30. Caroff, M. & Karibian, D. Structure of bacterial lipopolysaccharides. *Carbohydrate Research* **338,** 2431–2447 (2003).

31. Fraise, A, Maillard, J & Sattar, S. *Russell, Hugo and Ayliffe's Principles and Practice of Disinfection, Preservation and Sterilization [electronic resource].* (Hoboken : Wiley, 2012., 2012).

32. Lin, D. & Grossfield, A. Thermodynamics of Micelle Formation and Membrane Fusion Modulate Antimicrobial Lipopeptide Activity. *Biophysical Journal* **109,** 750–759 (2015).

Chapter 7

Conclusion

I have expanded the library of available molecular dynamic force fields to include both all-atom (AA) and coarse grained (CG) models for both chlorhexidine (CHX) and lipopolysaccharide (LPS) from *Pseudomonas Aeruginosa* PAO1.

Starting with the experimental knowledge of CHX in a model DMPC membrane from previous studies in our lab [1], an AA model was constructed to reproduce what was known experimentally. Specifically, langmuir-blodgett compression of DMPC monolayers showed that CHX has a high affinity for DMPC, and through neutron diffraction the location of CHX being at the water/lipid interface. The AA CHX model was constructed using the bonded terms taken from the amino acids of similar structure to CHX and determining the electrostatics through DFT calculations. A neutral, +1 and +2 charged version of the model were created due to the uncertainty in the exact charge of the molecule inside of a membrane.

The three AA models were then used to make CG version of each model, using the bottom up approach to be compatible with the MARTINI force field. This reduced the computational complexity and allows for a speed increase of two orders of magnitude allowing for much larger systems to be simulated on

a longer timescale. Each of the models were tested and iteratively altered until they could accurately reproduce the AA models.

With the ability to simulate large systems, we simulated a titration experiment introducing CHX into large model DMPC membrane of 900 lipids. From this, it was observed that the CHX molecules would aggregate in solution in small groups before entering the membrane. Once the group of CHX molecules entered the membrane they would stay at the lipid/water interface. The CHX molecules would then separate from each other, forming no discernible correlation to their intermolecular spacing. The effects of CHX on the DMPC are minimal up to 10% concentration, with a linear increase to the area per lipid and a near constant thickness, with a minor thinning of the membrane around 6% CHX concentration.

At concentration up to 10% CHX the DMPC membrane is still intact. Therefore our study was unable to observe the method in which CHX disrupt the membrane. An extension to this study would be to continually add CHX to the membrane until the membrane fell apart, or reached saturation. Experimental evidence of DMPC membranes withholding up to 30% CHX, from the previous neutron scattering experiments [1] demonstrates the ability of a DMPC to hold a large amount of CHX molecules. Therefore the continuation of the study of CHX in DMPC was halted in lieu of switching focus to a more biologically relevant membrane.

The outer membrane of *Pseudomonas Aeruginosa* consists of an asymmetric membrane with major components being LPS on the outer leaflet and PE phos-

pholipids on the inside. The library for the MARTINI force field consists of a large number of different PE and other phospholipids but not LPS. For this reason we created a CG model for LPS using the same bottom up approach as for the CHX model. AA models of LPS already exist and therefore the Glycam based LPS model from Soares et al. [2] was used to build the CG model.

Chapter 8

Future Work

This thesis provides the tools necessary for a wide range of future study. With the three AA and three CG models of CHX there is great potential to enhance the study of CHX through the use of molecular dynamics, on either scale. With the CG model, the partitioning of CHX into membranes of different lipid concentration could be studied. This type of study would show, which lipids CHX prefers to be in or if CHX changes the density of a certain lipid type, creating domains of a certain lipid type within a membrane. The CG model also allows for very large and long simulations, which could lead to studies on membrane fluctuations caused by the addition of CHX as well as the possible destruction of a membrane at high concentrations. High concentrations is possibly the greatest advantage of the CG model, which can approach the MIC concentrations of bacteria to aid in the determination of how CHX acts as an effective antiseptic.

The AA models allow for a more atomic resolution viewpoint of the mechanism of CHX. With this, the positioning and intermolecular positioning and connections can be viewed in which the CG model can not. This for instance was mentioned in Chapter 3, in which we observed a tendency for CHX to create hydrogen bonding with the DMPC headgroups. This aided in the understanding

to its location at the headgroup region of the membrane and lead us to study the change in the lateral diffusion caused by this.

The water models used in this study should be closely examined to ensure it is appropriate for the study of CHX. CHX is thought to destabilize the membrane of the cell, interfering with the process of osmosis, allowing for water to leak out of the cell [3]. It is therefore vital to have a correct water model that can reproduce the diffusion of water through the membrane. During the several microseconds of simulation time of our CHX/DMPC membranes, there was no water observed penetrating the membrane. Whether this is expected or a flaw in the water model, has yet to be determined and should be investigated.

With the creation of a CG model of LPS from *Pseudomonas aeruginosa*, a vast variety of different lipids in combination with our model can make for a wide diversity of different bacterial membranes to study. This model has the potential to broaden the field of study in both bacteria as well as antibacterial drug research. Although the focus of this thesis was to study the antiseptic activity of CHX, the expansion of this work is not limited to this single molecule. A coarse grained model of any drug can be made using the methods in Chapter 4 to create a CG model. In combination with our bacterial membrane with the given LPS model, the mechanism of membrane disruption can better be studied.

References

1. Komljenović, I., Marquardt, D., Harroun, T. A. & Sternin, E. Location of chlorhexidine in DMPC model membranes: a neutron diffraction study. *Chemistry and Physics of Lipids* **163,** 480–487 (2010).

2. Kirschner, K. N., Lins, R. D., Maass, A. & Soares, T. A. A glycam-based force field for simulations of lipopolysaccharide membranes: Parametrization and validation. *Journal of Chemical Theory and Computation* **8,** 4719–4731 (2012).

3. Greenstein, G., Berman, C. & Jaffin, R. Chlorhexidine. An adjunct to periodontal therapy. *J. Periodontol.* **57,** 370–377 (1986).

Chapter 9

Appendicies

9.1 MD Setup and Run Tutorial

1. Create or find a molecular structure file for your system (.pdb or .gro type files).

    - Proteins
        - Most protein structure files can be found at the RCSB protein data bank (`http://www.rcsb.org/pdb/home/home.do`).
        - Peptides of a single secondary structure can be built using a molecular editor such as the Avogadro software.
    - AA membrane
        - Many large simulation groups provide pre equilibrated systems on their websites available to download. This is advantageous because it can save hours/days of equilibration time needed on the system(you can skip to step 7). Examples: `http://wcm.ucalgary.ca/tieleman/downloads`, `http://mmkluster.fos.su.se/slipids/Downloads.html`.

  - Elsewise a membrane may be generated from the CHARMM-GUI membrane builder, which allows for any for a combination of a multitude of different lipids currently in their library, to either the top or bottom leaflet as defined by the user(`http://www.charmm-gui.org/`).

- CG membrane
  - Again many common membranes have been simulated by other research groups and can be downloaded from their main website. The main MARTINI webpage (`http://md.chem.rug.nl/index.php/downloads`) has many files, but a quick web search can find other more obscure structures.
  - CHARMM-GUI has a CG version as well (`http://www.charmm-gui.org/?doc=input/mbilayer`). Similar to the AA version, it can create different membranes with a combination of any lipid currently in their library.
  - MARTINI has a membrane builder insane, which unequilibrated membranes with any ratio of lipids chosen.

2. Create a topology file.
   - A topology file contains the information on which force field you are using, as well as a list of which molecules are in your system, and how many of them there are. A sample topology file can be found at `http://www.physics.brocku.ca/MARTINI/`.

3. Add water or ions.

   - Water

     – CHARMM-GUI often misplaces water molecules so it is often best to remove all waters from their file and add your own. Otherwise water can be added if more is needed in your system. This is done with the g_solvate tool.

     ```
     g_solvate -cp system.gro -cs spc216.gro -maxsol 5000
     -o system_solvated.gro
     ```

     This example uses spc216 water and adds at maximum 5000 of them to your system.gro file and creates an output system_solvated.gro. **If you plan to add ions to the system, add additional waters that will be replaced by ions in the next step.

   - Ions

     – Create a ions.tpr file using the grompp tool and the ions.mdp file located later in this appendix.

     ```
     grompp -f ions.mdp -c system_solv.gro -p topol.top
     -o ions.tpr
     ```

     – The genion tool can then be used on this created ions.tpr file to add as many ions of your choice.

```
genion -s ions.tpr -o system_solv_ions.gro -p topol.top
-pname NA -nname CL -nn 4 -np 6
```

This example adds 4 CL ions and 6 NA ions to your system. It will ask which molecules you want to replace from your system. For this you should choose water, so that it swaps out one water molecule for one ion.

4. Energy Minimization

- Your system is now built but the previous creation usually leaves the system very unstable and a few equilibration steps must be taken. First a steepest descent simulation should be used to remove unfavourable conformations using the sample minim.mdp.
  - Create a run input .tpr file using grompp.

    ```
    grompp -f minim.mdp -c system.gro -p system.top -o em.tpr
    ```

  - Run the simulation using as many threads as you want(2^n for best performance).

    ```
    mdrun -nt 8 -v -deffnm em
    ```

5. NVT

- The system is now ready for a md simulation with constant volume so the system does not explode if unfavourable conformations still exist.

You may want to hold a molecule using a position restraint at this step if it is still unstable.

- Create a run input .tpr file using grompp.

```
grompp -f nvt.mdp -c em.gro -p system.top -o nvt.tpr
```

- Run the simulation using as many threads as you want(2^n for best performance).

```
mdrun -nt 8 -v -deffnm nvt
```

6. NPT

- The system is now ready for a md simulation without constraint on its volume. You may want to hold a molecule using a position restraint at this step if it is still unstable.

  - Create a run input .tpr file using grompp.

```
grompp -f npt.mdp -c nvt.gro -p system.top -o npt.tpr
```

  - Run the simulation using as many threads as you want(2^n for best performance).

```
mdrun -nt 8 -v -deffnm npt
```

7. Production MD

- The system is now ready for a production md simulation with no constraints.

– Create a run input .tpr file using grompp.

```
grompp -f md.mdp -c npt.gro -p system.top -o md.tpr
```

– Run the simulation using as many threads as you want(2^n for best performance).

```
mdrun -nt 8 -v -deffnm md
```

9.2 Coarse Graining Method Tutorial

1. Choose a proper mapping from the AA version to the CG version of the molecule. The easiest way is to not try and reinvent the wheel, but rather look to literature to find molecules with similar structure and use their mapping for those similar sections. Otherwise, choose a mapping of approximately 4 heavy atoms to 1 virtual particle that avoids any internal rotation, so that the 4 atoms have a tendency to have one predominant conformation.

2. Use an AA simulation to replicate a CG simulation using the engine of your AA force field. The simulation must be long enough to make smooth distributions for all bonded parameters for step 3. This can be done in two ways

   - If you do not yet have a simulation of the AA structure - create virtual particles that track the center of mass of each of your mapped virtual

particles. This can be done using gromacs particle definitions in the [atoms] and [virtual_sitesn] sections:

```
[ atoms ]
65 COM 1 CHX V1 65 0 0
[virtual_sitesn]
65 2 1 2 3 4
```

This creates a particle number 65 which has no mass, charge or any effect on the system, but rather simply exists at the center of mass of particles 1,2,3 and 4

- If you have a pre-existing AA simulation - You yourself must calculate and track the center of mass of each of your mapped groups. This is terribly computationally inefficient.

3. Make a list of every bonded interaction between 2 adjacent virtual particle, angle between 3 particles and dihedral between 4. Create a histogram for each of these virtual bond, angle and dihedral for each set of the CG virtual particles from your AA simulation. These histograms can be created using the gromacs tools g_dist and g_angle:

```
g_dist -f md_v1 -s md_v1 -n bonds.ndx -o v1-v2.xvg
g_angle -f md_v1 -n angles.ndx -od v1-v2-v3.xvg -type angle
g_angle -f md_v1 -n dihedrals.ndx -od v1-v2-v3-v4.xvg -type dihedral
```

Make sure that the histograms are smooth enough to have sampled all of its conformations. If the resultant bond histograms can not be fit by a single

Gaussian curve, you might want to reconsider if a different mapping can be made so that it does.

4. Make a first approximation CG force field itp file. Here you should list each virtual particle, each bond, angle, and dihedral.

    - Particle definitions - Each virtual particle should have a charge of 0 or 1. The mass should be the sum of the masses of the constituent particles that it represents. The particle type should be chosen by either comparing to other similar molecules or a by a best guess of how polar/apolar that particle is.
    - Bond definitions - initial guesses for the length of the bond should be given as the center of the AA histogram. The strength should be given values of 50,000 kJ mol^{-1} nm^{-2} for extremely sharp peaks such as those in a ring structure, 10,000 kJ mol^{-1} nm^{-2} for determinate but wide peaks or 1,000 kJ mol^{-1} nm^{-2} for very wide or multiple peaked histograms. For first approximation, avoid the use of constraint bonds for they can be unstable.
    - Angle and dihedral definitions - initially set these to zero, for they might be unstable.

5. Use the last frame from your AA simulation to construct a CG system with only virtual particles. This is easily done if you have the virtual particle definitions, simply remove all atoms which are not virtual. If you did not

use the particle definitions, calculate the position of the virtual particles using the center of mass of the atoms they represent.

6. Run the CG simulation. Initially use a small time step of 2 fs. If the system is still unstable, you may try to either reduce spring constants or lower the time step to 1 fs.

7. Create a histogram for each bond as done in previously for the AA simulation in step 3.

8. Match the AA and CG histograms. If the peak is too sharp, reduce the strength. If it is off centred, shift the length by the amount that is is off by. Do not exceed a bond strength of 50,000 kJ mol^{-1} nm^{-2}.

9. Repeat steps 6-8 until there is a good agreement between all bonds. The time step may be increased slowly if the system is stable up to 20 fs.

10. Add angle and bond terms. Weak terms should be used at first with an angle strength of about 100 and dihedrals strength of 1.

11. Run the CG simulation. You may need to use a small time step of 2 fs. If the system is still unstable, you may try to either reduce spring constants or lower the time step to 1 fs.

12. Match the AA and CG histograms. If the peak is too sharp, reduce the strength. If it is off centred, shift the length by the amount that is is off by. Do not exceed a bond strength of 50,000 kJ mol^{-1} nm^{-2}, angle strength of

1,000 and should not be below 0 ° or exceed an angle of 180 ° and dihedrals should not exceed a strength of 50.

13. Repeat steps 11-12 until there is a good agreement between all bonds. The time step may be increased slowly if the system is stable up to 20 fs.

14. Iterate as many times as you want, until it matches either AA results, or experimental results.

Chapter 10

Permissions

ELSEVIER LICENSE
TERMS AND CONDITIONS

Mar 24, 2016

This is a License Agreement between Brad J Van Oosten ("You") and Elsevier ("Elsevier") provided by Copyright Clearance Center ("CCC"). The license consists of your order details, the terms and conditions provided by Elsevier, and the payment terms and conditions.

All payments must be made in full to CCC. For payment instructions, please see information listed at the bottom of this form.

Supplier	Elsevier Limited The Boulevard,Langford Lane Kidlington,Oxford,OX5 1GB,UK
Registered Company Number	1982084
Customer name	Brad J Van Oosten
Customer address	17 Hemlock St. St Catharines, ON l2t 4b7
License number	3835530186001
License date	Mar 24, 2016
Licensed content publisher	Elsevier
Licensed content publication	Journal of Molecular Graphics and Modelling
Licensed content title	Small molecule interaction with lipid bilayers: A molecular dynamics study of chlorhexidine
Licensed content author	Brad Van Oosten,Drew Marquardt,Ivana Komljenović,Jeremy P. Bradshaw,Edward Sternin,Thad A. Harroun
Licensed content date	March 2014
Licensed content volume number	48
Licensed content issue number	n/a
Number of pages	9
Start Page	96
End Page	104
Type of Use	reuse in a thesis/dissertation
Portion	full article
Format	both print and electronic
Are you the author of this Elsevier article?	Yes
Will you be translating?	No
Title of your thesis/dissertation	A multi-scale molecular dynamic approach to the study of the outer membrane of the bacteria {\it Psudomonas Aeruginosa} PA01 and

	the biocide chlorhexidine
Expected completion date	Jul 2016
Estimated size (number of pages)	300
Elsevier VAT number	GB 494 6272 12
Permissions price	0.00 CAD
VAT/Local Sales Tax	0.00 CAD / 0.00 GBP
Total	0.00 CAD
Terms and Conditions	

INTRODUCTION

1. The publisher for this copyrighted material is Elsevier. By clicking "accept" in connection with completing this licensing transaction, you agree that the following terms and conditions apply to this transaction (along with the Billing and Payment terms and conditions established by Copyright Clearance Center, Inc. ("CCC"), at the time that you opened your Rightslink account and that are available at any time at http://myaccount.copyright.com).

GENERAL TERMS

2. Elsevier hereby grants you permission to reproduce the aforementioned material subject to the terms and conditions indicated.
3. Acknowledgement: If any part of the material to be used (for example, figures) has appeared in our publication with credit or acknowledgement to another source, permission must also be sought from that source. If such permission is not obtained then that material may not be included in your publication/copies. Suitable acknowledgement to the source must be made, either as a footnote or in a reference list at the end of your publication, as follows:
"Reprinted from Publication title, Vol /edition number, Author(s), Title of article / title of chapter, Pages No., Copyright (Year), with permission from Elsevier [OR APPLICABLE SOCIETY COPYRIGHT OWNER]." Also Lancet special credit - "Reprinted from The Lancet, Vol. number, Author(s), Title of article, Pages No., Copyright (Year), with permission from Elsevier."
4. Reproduction of this material is confined to the purpose and/or media for which permission is hereby given.
5. Altering/Modifying Material: Not Permitted. However figures and illustrations may be altered/adapted minimally to serve your work. Any other abbreviations, additions, deletions and/or any other alterations shall be made only with prior written authorization of Elsevier Ltd. (Please contact Elsevier at permissions@elsevier.com)
6. If the permission fee for the requested use of our material is waived in this instance, please be advised that your future requests for Elsevier materials may attract a fee.
7. Reservation of Rights: Publisher reserves all rights not specifically granted in the combination of (i) the license details provided by you and accepted in the course of this licensing transaction, (ii) these terms and conditions and (iii) CCC's Billing and Payment terms and conditions.
8. License Contingent Upon Payment: While you may exercise the rights licensed immediately upon issuance of the license at the end of the licensing process for the transaction, provided that you have disclosed complete and accurate details of your proposed use, no license is finally effective unless and until full payment is received from you (either by publisher or by CCC) as provided in CCC's Billing and Payment terms and conditions. If full payment is not received on a timely basis, then any license preliminarily granted shall be

deemed automatically revoked and shall be void as if never granted. Further, in the event that you breach any of these terms and conditions or any of CCC's Billing and Payment terms and conditions, the license is automatically revoked and shall be void as if never granted. Use of materials as described in a revoked license, as well as any use of the materials beyond the scope of an unrevoked license, may constitute copyright infringement and publisher reserves the right to take any and all action to protect its copyright in the materials.

9. Warranties: Publisher makes no representations or warranties with respect to the licensed material.

10. Indemnity: You hereby indemnify and agree to hold harmless publisher and CCC, and their respective officers, directors, employees and agents, from and against any and all claims arising out of your use of the licensed material other than as specifically authorized pursuant to this license.

11. No Transfer of License: This license is personal to you and may not be sublicensed, assigned, or transferred by you to any other person without publisher's written permission.

12. No Amendment Except in Writing: This license may not be amended except in a writing signed by both parties (or, in the case of publisher, by CCC on publisher's behalf).

13. Objection to Contrary Terms: Publisher hereby objects to any terms contained in any purchase order, acknowledgment, check endorsement or other writing prepared by you, which terms are inconsistent with these terms and conditions or CCC's Billing and Payment terms and conditions. These terms and conditions, together with CCC's Billing and Payment terms and conditions (which are incorporated herein), comprise the entire agreement between you and publisher (and CCC) concerning this licensing transaction. In the event of any conflict between your obligations established by these terms and conditions and those established by CCC's Billing and Payment terms and conditions, these terms and conditions shall control.

14. Revocation: Elsevier or Copyright Clearance Center may deny the permissions described in this License at their sole discretion, for any reason or no reason, with a full refund payable to you. Notice of such denial will be made using the contact information provided by you. Failure to receive such notice will not alter or invalidate the denial. In no event will Elsevier or Copyright Clearance Center be responsible or liable for any costs, expenses or damage incurred by you as a result of a denial of your permission request, other than a refund of the amount(s) paid by you to Elsevier and/or Copyright Clearance Center for denied permissions.

LIMITED LICENSE

The following terms and conditions apply only to specific license types:

15. **Translation**: This permission is granted for non-exclusive world **English** rights only unless your license was granted for translation rights. If you licensed translation rights you may only translate this content into the languages you requested. A professional translator must perform all translations and reproduce the content word for word preserving the integrity of the article.

16. **Posting licensed content on any Website**: The following terms and conditions apply as follows: Licensing material from an Elsevier journal: All content posted to the web site must maintain the copyright information line on the bottom of each image; A hyper-text must be included to the Homepage of the journal from which you are licensing at http://www.sciencedirect.com/science/journal/xxxxx or the Elsevier homepage for books at http://www.elsevier.com; Central Storage: This license does not include permission for a scanned version of the material to be stored in a central repository such as that provided by Heron/XanEdu.

Licensing material from an Elsevier book: A hyper-text link must be included to the Elsevier

homepage at http://www.elsevier.com . All content posted to the web site must maintain the copyright information line on the bottom of each image.

Posting licensed content on Electronic reserve: In addition to the above the following clauses are applicable: The web site must be password-protected and made available only to bona fide students registered on a relevant course. This permission is granted for 1 year only. You may obtain a new license for future website posting.

17. **For journal authors:** the following clauses are applicable in addition to the above:

Preprints:

A preprint is an author's own write-up of research results and analysis, it has not been peer-reviewed, nor has it had any other value added to it by a publisher (such as formatting, copyright, technical enhancement etc.).

Authors can share their preprints anywhere at any time. Preprints should not be added to or enhanced in any way in order to appear more like, or to substitute for, the final versions of articles however authors can update their preprints on arXiv or RePEc with their Accepted Author Manuscript (see below).

If accepted for publication, we encourage authors to link from the preprint to their formal publication via its DOI. Millions of researchers have access to the formal publications on ScienceDirect, and so links will help users to find, access, cite and use the best available version. Please note that Cell Press, The Lancet and some society-owned have different preprint policies. Information on these policies is available on the journal homepage.

Accepted Author Manuscripts: An accepted author manuscript is the manuscript of an article that has been accepted for publication and which typically includes author-incorporated changes suggested during submission, peer review and editor-author communications.

Authors can share their accepted author manuscript:

- immediately
    - via their non-commercial person homepage or blog
    - by updating a preprint in arXiv or RePEc with the accepted manuscript
    - via their research institute or institutional repository for internal institutional uses or as part of an invitation-only research collaboration work-group
    - directly by providing copies to their students or to research collaborators for their personal use
    - for private scholarly sharing as part of an invitation-only work group on commercial sites with which Elsevier has an agreement
- after the embargo period
    - via non-commercial hosting platforms such as their institutional repository
    - via commercial sites with which Elsevier has an agreement

In all cases accepted manuscripts should:

- link to the formal publication via its DOI
- bear a CC-BY-NC-ND license - this is easy to do
- if aggregated with other manuscripts, for example in a repository or other site, be shared in alignment with our hosting policy not be added to or enhanced in any way to appear more like, or to substitute for, the published journal article.

Published journal article (JPA): A published journal article (PJA) is the definitive final record of published research that appears or will appear in the journal and embodies all

value-adding publishing activities including peer review co-ordination, copy-editing, formatting, (if relevant) pagination and online enrichment.
Policies for sharing publishing journal articles differ for subscription and gold open access articles:
Subscription Articles: If you are an author, please share a link to your article rather than the full-text. Millions of researchers have access to the formal publications on ScienceDirect, and so links will help your users to find, access, cite, and use the best available version.
Theses and dissertations which contain embedded PJAs as part of the formal submission can be posted publicly by the awarding institution with DOI links back to the formal publications on ScienceDirect.
If you are affiliated with a library that subscribes to ScienceDirect you have additional private sharing rights for others' research accessed under that agreement. This includes use for classroom teaching and internal training at the institution (including use in course packs and courseware programs), and inclusion of the article for grant funding purposes.
Gold Open Access Articles: May be shared according to the author-selected end-user license and should contain a CrossMark logo, the end user license, and a DOI link to the formal publication on ScienceDirect.
Please refer to Elsevier's posting policy for further information.
18. **For book authors** the following clauses are applicable in addition to the above:
Authors are permitted to place a brief summary of their work online only. You are not allowed to download and post the published electronic version of your chapter, nor may you scan the printed edition to create an electronic version. **Posting to a repository:** Authors are permitted to post a summary of their chapter only in their institution's repository.
19. **Thesis/Dissertation**: If your license is for use in a thesis/dissertation your thesis may be submitted to your institution in either print or electronic form. Should your thesis be published commercially, please reapply for permission. These requirements include permission for the Library and Archives of Canada to supply single copies, on demand, of the complete thesis and include permission for Proquest/UMI to supply single copies, on demand, of the complete thesis. Should your thesis be published commercially, please reapply for permission. Theses and dissertations which contain embedded PJAs as part of the formal submission can be posted publicly by the awarding institution with DOI links back to the formal publications on ScienceDirect.

Elsevier Open Access Terms and Conditions
You can publish open access with Elsevier in hundreds of open access journals or in nearly 2000 established subscription journals that support open access publishing. Permitted third party re-use of these open access articles is defined by the author's choice of Creative Commons user license. See our open access license policy for more information.
Terms & Conditions applicable to all Open Access articles published with Elsevier:
Any reuse of the article must not represent the author as endorsing the adaptation of the article nor should the article be modified in such a way as to damage the author's honour or reputation. If any changes have been made, such changes must be clearly indicated.
The author(s) must be appropriately credited and we ask that you include the end user license and a DOI link to the formal publication on ScienceDirect.
If any part of the material to be used (for example, figures) has appeared in our publication with credit or acknowledgement to another source it is the responsibility of the user to ensure their reuse complies with the terms and conditions determined by the rights holder.
Additional Terms & Conditions applicable to each Creative Commons user license:
CC BY: The CC-BY license allows users to copy, to create extracts, abstracts and new works from the Article, to alter and revise the Article and to make commercial use of the

Article (including reuse and/or resale of the Article by commercial entities), provided the user gives appropriate credit (with a link to the formal publication through the relevant DOI), provides a link to the license, indicates if changes were made and the licensor is not represented as endorsing the use made of the work. The full details of the license are available at http://creativecommons.org/licenses/by/4.0.

CC BY NC SA: The CC BY-NC-SA license allows users to copy, to create extracts, abstracts and new works from the Article, to alter and revise the Article, provided this is not done for commercial purposes, and that the user gives appropriate credit (with a link to the formal publication through the relevant DOI), provides a link to the license, indicates if changes were made and the licensor is not represented as endorsing the use made of the work. Further, any new works must be made available on the same conditions. The full details of the license are available at http://creativecommons.org/licenses/by-nc-sa/4.0.

CC BY NC ND: The CC BY-NC-ND license allows users to copy and distribute the Article, provided this is not done for commercial purposes and further does not permit distribution of the Article if it is changed or edited in any way, and provided the user gives appropriate credit (with a link to the formal publication through the relevant DOI), provides a link to the license, and that the licensor is not represented as endorsing the use made of the work. The full details of the license are available at http://creativecommons.org/licenses/by-nc-nd/4.0.

Any commercial reuse of Open Access articles published with a CC BY NC SA or CC BY NC ND license requires permission from Elsevier and will be subject to a fee.

Commercial reuse includes:

- Associating advertising with the full text of the Article
- Charging fees for document delivery or access
- Article aggregation
- Systematic distribution via e-mail lists or share buttons

Posting or linking by commercial companies for use by customers of those companies.

20. **Other Conditions**:

v1.8

ELSEVIER LICENSE
TERMS AND CONDITIONS

Mar 24, 2016

This is a License Agreement between Brad J Van Oosten ("You") and Elsevier ("Elsevier") provided by Copyright Clearance Center ("CCC"). The license consists of your order details, the terms and conditions provided by Elsevier, and the payment terms and conditions.

All payments must be made in full to CCC. For payment instructions, please see information listed at the bottom of this form.

Supplier	Elsevier Limited The Boulevard,Langford Lane Kidlington,Oxford,OX5 1GB,UK
Registered Company Number	1982084
Customer name	Brad J Van Oosten
Customer address	17 Hemlock St. St Catharines, ON l2t 4b7
License number	3835530564172
License date	Mar 24, 2016
Licensed content publisher	Elsevier
Licensed content publication	Journal of Molecular Graphics and Modelling
Licensed content title	A MARTINI extension for Pseudomonas aeruginosa PAO1 lipopolysaccharide
Licensed content author	Brad Van Oosten,Thad A. Harroun
Licensed content date	January 2016
Licensed content volume number	63
Licensed content issue number	n/a
Number of pages	9
Start Page	125
End Page	133
Type of Use	reuse in a thesis/dissertation
Intended publisher of new work	other
Portion	full article
Format	both print and electronic
Are you the author of this Elsevier article?	Yes
Will you be translating?	No
Title of your	A multi-scale molecular dynamic approach to the study of the outer

thesis/dissertation	membrane of the bacteria {\it Psudomonas Aeruginosa} PA01 and the biocide chlorhexidine
Expected completion date	Jul 2016
Estimated size (number of pages)	300
Elsevier VAT number	GB 494 6272 12
Permissions price	0.00 USD
VAT/Local Sales Tax	0.00 USD / 0.00 GBP
Total	0.00 USD
Terms and Conditions	

INTRODUCTION

1. The publisher for this copyrighted material is Elsevier. By clicking "accept" in connection with completing this licensing transaction, you agree that the following terms and conditions apply to this transaction (along with the Billing and Payment terms and conditions established by Copyright Clearance Center, Inc. ("CCC"), at the time that you opened your Rightslink account and that are available at any time at http://myaccount.copyright.com).

GENERAL TERMS

2. Elsevier hereby grants you permission to reproduce the aforementioned material subject to the terms and conditions indicated.
3. Acknowledgement: If any part of the material to be used (for example, figures) has appeared in our publication with credit or acknowledgement to another source, permission must also be sought from that source. If such permission is not obtained then that material may not be included in your publication/copies. Suitable acknowledgement to the source must be made, either as a footnote or in a reference list at the end of your publication, as follows:
"Reprinted from Publication title, Vol /edition number, Author(s), Title of article / title of chapter, Pages No., Copyright (Year), with permission from Elsevier [OR APPLICABLE SOCIETY COPYRIGHT OWNER]." Also Lancet special credit - "Reprinted from The Lancet, Vol. number, Author(s), Title of article, Pages No., Copyright (Year), with permission from Elsevier."
4. Reproduction of this material is confined to the purpose and/or media for which permission is hereby given.
5. Altering/Modifying Material: Not Permitted. However figures and illustrations may be altered/adapted minimally to serve your work. Any other abbreviations, additions, deletions and/or any other alterations shall be made only with prior written authorization of Elsevier Ltd. (Please contact Elsevier at permissions@elsevier.com)
6. If the permission fee for the requested use of our material is waived in this instance, please be advised that your future requests for Elsevier materials may attract a fee.
7. Reservation of Rights: Publisher reserves all rights not specifically granted in the combination of (i) the license details provided by you and accepted in the course of this licensing transaction, (ii) these terms and conditions and (iii) CCC's Billing and Payment terms and conditions.
8. License Contingent Upon Payment: While you may exercise the rights licensed immediately upon issuance of the license at the end of the licensing process for the transaction, provided that you have disclosed complete and accurate details of your proposed use, no license is finally effective unless and until full payment is received from you (either by publisher or by CCC) as provided in CCC's Billing and Payment terms and conditions. If

full payment is not received on a timely basis, then any license preliminarily granted shall be deemed automatically revoked and shall be void as if never granted. Further, in the event that you breach any of these terms and conditions or any of CCC's Billing and Payment terms and conditions, the license is automatically revoked and shall be void as if never granted. Use of materials as described in a revoked license, as well as any use of the materials beyond the scope of an unrevoked license, may constitute copyright infringement and publisher reserves the right to take any and all action to protect its copyright in the materials.

9. Warranties: Publisher makes no representations or warranties with respect to the licensed material.

10. Indemnity: You hereby indemnify and agree to hold harmless publisher and CCC, and their respective officers, directors, employees and agents, from and against any and all claims arising out of your use of the licensed material other than as specifically authorized pursuant to this license.

11. No Transfer of License: This license is personal to you and may not be sublicensed, assigned, or transferred by you to any other person without publisher's written permission.

12. No Amendment Except in Writing: This license may not be amended except in a writing signed by both parties (or, in the case of publisher, by CCC on publisher's behalf).

13. Objection to Contrary Terms: Publisher hereby objects to any terms contained in any purchase order, acknowledgment, check endorsement or other writing prepared by you, which terms are inconsistent with these terms and conditions or CCC's Billing and Payment terms and conditions. These terms and conditions, together with CCC's Billing and Payment terms and conditions (which are incorporated herein), comprise the entire agreement between you and publisher (and CCC) concerning this licensing transaction. In the event of any conflict between your obligations established by these terms and conditions and those established by CCC's Billing and Payment terms and conditions, these terms and conditions shall control.

14. Revocation: Elsevier or Copyright Clearance Center may deny the permissions described in this License at their sole discretion, for any reason or no reason, with a full refund payable to you. Notice of such denial will be made using the contact information provided by you. Failure to receive such notice will not alter or invalidate the denial. In no event will Elsevier or Copyright Clearance Center be responsible or liable for any costs, expenses or damage incurred by you as a result of a denial of your permission request, other than a refund of the amount(s) paid by you to Elsevier and/or Copyright Clearance Center for denied permissions.

LIMITED LICENSE

The following terms and conditions apply only to specific license types:

15. **Translation**: This permission is granted for non-exclusive world **English** rights only unless your license was granted for translation rights. If you licensed translation rights you may only translate this content into the languages you requested. A professional translator must perform all translations and reproduce the content word for word preserving the integrity of the article.

16. **Posting licensed content on any Website**: The following terms and conditions apply as follows: Licensing material from an Elsevier journal: All content posted to the web site must maintain the copyright information line on the bottom of each image; A hyper-text must be included to the Homepage of the journal from which you are licensing at http://www.sciencedirect.com/science/journal/xxxxx or the Elsevier homepage for books at http://www.elsevier.com; Central Storage: This license does not include permission for a scanned version of the material to be stored in a central repository such as that provided by Heron/XanEdu.

Licensing material from an Elsevier book: A hyper-text link must be included to the Elsevier homepage at http://www.elsevier.com . All content posted to the web site must maintain the copyright information line on the bottom of each image.

Posting licensed content on Electronic reserve: In addition to the above the following clauses are applicable: The web site must be password-protected and made available only to bona fide students registered on a relevant course. This permission is granted for 1 year only. You may obtain a new license for future website posting.

17. **For journal authors:** the following clauses are applicable in addition to the above:

Preprints:

A preprint is an author's own write-up of research results and analysis, it has not been peer-reviewed, nor has it had any other value added to it by a publisher (such as formatting, copyright, technical enhancement etc.).

Authors can share their preprints anywhere at any time. Preprints should not be added to or enhanced in any way in order to appear more like, or to substitute for, the final versions of articles however authors can update their preprints on arXiv or RePEc with their Accepted Author Manuscript (see below).

If accepted for publication, we encourage authors to link from the preprint to their formal publication via its DOI. Millions of researchers have access to the formal publications on ScienceDirect, and so links will help users to find, access, cite and use the best available version. Please note that Cell Press, The Lancet and some society-owned have different preprint policies. Information on these policies is available on the journal homepage.

Accepted Author Manuscripts: An accepted author manuscript is the manuscript of an article that has been accepted for publication and which typically includes author-incorporated changes suggested during submission, peer review and editor-author communications.

Authors can share their accepted author manuscript:

- immediately
    - via their non-commercial person homepage or blog
    - by updating a preprint in arXiv or RePEc with the accepted manuscript
    - via their research institute or institutional repository for internal institutional uses or as part of an invitation-only research collaboration work-group
    - directly by providing copies to their students or to research collaborators for their personal use
    - for private scholarly sharing as part of an invitation-only work group on commercial sites with which Elsevier has an agreement
- after the embargo period
    - via non-commercial hosting platforms such as their institutional repository
    - via commercial sites with which Elsevier has an agreement

In all cases accepted manuscripts should:

- link to the formal publication via its DOI
- bear a CC-BY-NC-ND license - this is easy to do
- if aggregated with other manuscripts, for example in a repository or other site, be shared in alignment with our hosting policy not be added to or enhanced in any way to appear more like, or to substitute for, the published journal article.

Published journal article (JPA): A published journal article (PJA) is the definitive final

record of published research that appears or will appear in the journal and embodies all value-adding publishing activities including peer review co-ordination, copy-editing, formatting, (if relevant) pagination and online enrichment.
Policies for sharing publishing journal articles differ for subscription and gold open access articles:
Subscription Articles: If you are an author, please share a link to your article rather than the full-text. Millions of researchers have access to the formal publications on ScienceDirect, and so links will help your users to find, access, cite, and use the best available version.
Theses and dissertations which contain embedded PJAs as part of the formal submission can be posted publicly by the awarding institution with DOI links back to the formal publications on ScienceDirect.
If you are affiliated with a library that subscribes to ScienceDirect you have additional private sharing rights for others' research accessed under that agreement. This includes use for classroom teaching and internal training at the institution (including use in course packs and courseware programs), and inclusion of the article for grant funding purposes.
Gold Open Access Articles: May be shared according to the author-selected end-user license and should contain a CrossMark logo, the end user license, and a DOI link to the formal publication on ScienceDirect.
Please refer to Elsevier's posting policy for further information.
18. **For book authors** the following clauses are applicable in addition to the above:
Authors are permitted to place a brief summary of their work online only. You are not allowed to download and post the published electronic version of your chapter, nor may you scan the printed edition to create an electronic version. **Posting to a repository:** Authors are permitted to post a summary of their chapter only in their institution's repository.
19. **Thesis/Dissertation**: If your license is for use in a thesis/dissertation your thesis may be submitted to your institution in either print or electronic form. Should your thesis be published commercially, please reapply for permission. These requirements include permission for the Library and Archives of Canada to supply single copies, on demand, of the complete thesis and include permission for Proquest/UMI to supply single copies, on demand, of the complete thesis. Should your thesis be published commercially, please reapply for permission. Theses and dissertations which contain embedded PJAs as part of the formal submission can be posted publicly by the awarding institution with DOI links back to the formal publications on ScienceDirect.

Elsevier Open Access Terms and Conditions
You can publish open access with Elsevier in hundreds of open access journals or in nearly 2000 established subscription journals that support open access publishing. Permitted third party re-use of these open access articles is defined by the author's choice of Creative Commons user license. See our open access license policy for more information.
Terms & Conditions applicable to all Open Access articles published with Elsevier:
Any reuse of the article must not represent the author as endorsing the adaptation of the article nor should the article be modified in such a way as to damage the author's honour or reputation. If any changes have been made, such changes must be clearly indicated.
The author(s) must be appropriately credited and we ask that you include the end user license and a DOI link to the formal publication on ScienceDirect.
If any part of the material to be used (for example, figures) has appeared in our publication with credit or acknowledgement to another source it is the responsibility of the user to ensure their reuse complies with the terms and conditions determined by the rights holder.
Additional Terms & Conditions applicable to each Creative Commons user license:
CC BY: The CC-BY license allows users to copy, to create extracts, abstracts and new

works from the Article, to alter and revise the Article and to make commercial use of the Article (including reuse and/or resale of the Article by commercial entities), provided the user gives appropriate credit (with a link to the formal publication through the relevant DOI), provides a link to the license, indicates if changes were made and the licensor is not represented as endorsing the use made of the work. The full details of the license are available at http://creativecommons.org/licenses/by/4.0.

CC BY NC SA: The CC BY-NC-SA license allows users to copy, to create extracts, abstracts and new works from the Article, to alter and revise the Article, provided this is not done for commercial purposes, and that the user gives appropriate credit (with a link to the formal publication through the relevant DOI), provides a link to the license, indicates if changes were made and the licensor is not represented as endorsing the use made of the work. Further, any new works must be made available on the same conditions. The full details of the license are available at http://creativecommons.org/licenses/by-nc-sa/4.0.

CC BY NC ND: The CC BY-NC-ND license allows users to copy and distribute the Article, provided this is not done for commercial purposes and further does not permit distribution of the Article if it is changed or edited in any way, and provided the user gives appropriate credit (with a link to the formal publication through the relevant DOI), provides a link to the license, and that the licensor is not represented as endorsing the use made of the work. The full details of the license are available at http://creativecommons.org/licenses/by-nc-nd/4.0.

Any commercial reuse of Open Access articles published with a CC BY NC SA or CC BY NC ND license requires permission from Elsevier and will be subject to a fee.

Commercial reuse includes:

- Associating advertising with the full text of the Article
- Charging fees for document delivery or access
- Article aggregation
- Systematic distribution via e-mail lists or share buttons

Posting or linking by commercial companies for use by customers of those companies.

20. **Other Conditions**:

v1.8

Questions? customercare@copyright.com or +1-855-239-3415 (toll free in the US) or +1-978-646-2777.